TRANSPORT AND AGGLOMERATION OF DUST CONTAMINANT PARTICLES IN REACTIVE ION ETCH REACTORS

BY

FREDERICK YI-KAI HUANG

B.S., University of Illinois at Urbana-Champaign, 1991
M.S., University of Illinois at Urbana-Champaign, 1994

THESIS

Submitted in partial fulfillment of the requirements
for the degree of Doctor of Philosophy in Electrical Engineering
in the Graduate College of the
University of Illinois at Urbana-Champaign, 1997

Urbana, Illinois

TRANSPORT AND AGGLOMERATION OF DUST CONTAMINANT PARTICLES IN REACTIVE ION ETCH REACTORS

Frederick Y. Huang, Ph.D.
Department of Electrical and Computer Engineering
University of Illinois at Urbana-Champaign, 1997
M. J. Kushner, Advisor

Dust particle contamination in plasma etching reactors continues to be a major concern to microelectronic device manufacturers. Dust particulates as small as tens of nanometers in dimension can produce killer defects on the substrate surface. These contaminants are produced either through gas-phase nucleation processes in the discharge, or through interaction with surfaces in the reactor. Their transport is governed by the forces exerted upon them in the reactor, primarily electrostatic, ion drag, neutral drag, thermophoresis, and gravitational forces.

Dust particulates collected from reactive ion etching (RIE) reactors are commonly found to be agglomerate structures consisting of smaller, spherical "primary particles." These primary particles grow to a terminal size in the reactor and then combine to form the larger agglomerates. This agglomeration phenomenon requires a certain amount of kinetic energy from the primary particles, which typically charge negatively in such discharges. With sufficient kinetic energy, primary particles can overcome their mutual electrostatic repulsion and join together to form an agglomerate particle.

The transport and agglomeration of dust particles in RIE reactors has been studied using a series of numerical simulations. These computational models have demonstrated that both dust transport and agglomeration are highly dependent on reactor geometry and discharge operating conditions, as well as the size of the primary particle. In general, higher radio-frequency (RF)

powers and larger primary particles lead to more agglomeration. This in turn typically results in a larger amount of substrate contamination.

The morphology of the agglomerates formed was also found to be dependent on plasma conditions. Agglomerates generally grow either in a diffusive or ballistic manner. Neutral gas flow in the reactor has been found to be a useful means of controlling contamination. Higher flow rates can sweep dust particles away from sensitive areas of the reactor before they reach the surfaces.

TABLE OF CONTENTS

Page

1. INTRODUCTION 1

1.1 Figures 8
1.2 References 12

2. MODEL DESCRIPTION 14

2.1 Introduction 14
2.2 The Hybrid Plasma Equipment Model (HPEM) 15
2.3 The Dust Transport Simulation (DTS) 18
2.4 The Particle Agglomeration Model (PAM) 21
2.5 The Molecular Dynamics Simulation (MD-PAM) 25
2.6 Figures 29
2.7 References 37

3. SIMULATION RESULTS AND ANALYSIS 38

3.1 Results for the Dust Transport Simulation 38
3.2 Results for the Particle Agglomeration Model 40
3.3 Results for the Molecular Dynamics PAM Model 44
3.4 Figures 55
3.5 References 93

4. CONCLUSIONS 94

VITA 97

ACKNOWLEDGEMENTS

I would like to thank the Semiconductor Research Corporation for its generous support of my research work through an SRC Graduate Fellowship. In particular, I would like to acknowledge Ginny Poe, coordinator of the SRC's Graduate Fellowship Program, for her endless efforts to help me survive graduate school. In addition, I would also like to thank the following agencies for their support: the National Science Foundation, SEMATECH, Sandia National Laboratories, and the University of Wisconsin ERC for Plasma Aided Manufacturing.

My deepest thanks go to my thesis advisor, Mark J. Kushner, for directing my graduate research. Over the course of six years, he has never failed to make time for my seemingly endless stream of questions, and has always exhibited the utmost patience and wisdom. I am grateful for all the guidance he has provided to me of not only science, but of life as well.

Thanks also to my fellow members of the ODP lab: Mike Grapperhaus, Rob Hoekstra, Ron Kinder, Peter Xu, Da Zhang, Dr. Eric Keiter, Dr. Shahid Rauf, and Kelly Voyles. I would also like to thank the past members of ODP: Drs. Helen Hwang, Irène Pérès, Jong Won Shon, Seung Choi, Phillip Stout, Ann Gentile, Mike Hartig, Peter Ventzek, Hoyoung Pak, Tim Sommerer, Mike McCaughey, and Jean Sexton.

I would not have made it this far without the help of many people during my college career. In particular, I would like to thank the following people for their support and friendship all these years: Mary Piotrowski, Craig Payne, Charlotte Bobek, Julian Hsiang, Cecilia Friberg, Virginia Huang, Dawn Janich, and Jami Tucker. Special thanks go to my extended family in Champaign, the members of Sung Lee Tae Kwon Do, for always reminding me of what's really important in life: the people around you. The list of people from Sung Lee I'd especially like to

thank is long, but well-deserved: Bill Ehrhardt, Mike Zeller, Adrian “Dough Boy” Rodriguez, Alice Lambert, Derek Whiting, Lola Kwan, Laura Harmon, Katherine Czismadia, Paul Zinnes, Andy Weinstein, Jennie Harris, Chili Shears, Drew Castelein, Kendall Pierson, Sunny Kim, Matt Cooper, Ray and Christy Wagner, Jennifer Keller, Steve Moritz, Becky Wilkins, Vince Clark, Rob and Joy Whitbred, Marc Talbot, Alex Brown, Taliah Charlton, Kasia Jarzebska, Tomoko Koyama, Ron Foley, Philip Hwang, Axita Patel, Betty King, Dori Thomas, Kristi Moss, Tara Zaharoff, Isao Fujita, Vince Duffy, Brett and Kristin Feddersen, Eva Dougherty, Eric Hiller, Carla Samuels, Melissa Zilic, Sandra Franco, Mike McDonald, Dennis Abry, John Genge, Darrell Stam, Marya Ryan, Angel Gomez, Kevin Phillips, Michele Miller, Hart Fisher, David Riecks, Dave Wheeler, Jim Chou, Rick Kacprowicz, Jeff Rose, Dwayne Williams, Ralph and Carolyn Trimble, Suja Maringanti, and Satyam Subrahmanyam. Thanks for a lot more fun than a grad student could ever realistically hope of having.

Finally, my love and gratitude to my parents and sister. What they’ve done for me could never be expressed adequately in words. Everything I’ve ever accomplished in life is a result of their undying love, faith, and understanding, and so I dedicate this thesis to them.

© Copyright by Frederick Yi-Kai Huang, 1997

1. INTRODUCTION

Dust-particle contamination of wafers in plasma etching reactors is a continuing concern in the microelectronics industry. While state-of-the-art cleanrooms and manufacturing processes have reduced environmental particle levels to almost negligible concentrations, microcontamination due to particles generated in the processes is a leading cause of degradation of device yields.[1] With the advent of minimum feature-size design rules in the submicron range, even very small (less than hundreds of nanometers) particulates can result in “killer defects” on the silicon die, and they can affect the quality of films deposited by plasma-enhanced chemical vapor deposition. In addition, these particles typically charge negatively in the discharge since the collection rate of electrons on their surface is initially higher than that of positive ions. As a result of this electrical charging, dust contamination can also perturb the local plasma properties.[2] Therefore, understanding and controlling the generation and transport of these contaminants is of great interest to the semiconductor community. According to the Semiconductor Industry Association (SIA) National Technology Roadmap, the current requirement for wafer defect density is 0.024 defects/cm^2. This value will drop to 0.016 by 1998.[3] The current metrology requirements is detection of particles as small as 50 nm in size on a bare silicon wafer.[4] As the minimum feature size continues to decrease into the sub-0.1 μm range, these requirements become even more demanding.

Dusty plasmas have been studied for many years in the field of astrophysics.[5-7] Recently, though, because of their relevance to integrated circuit manufacturing, dusty plasmas have received much attention from other researchers.[1-4,8-24] Spears et al. were the first to observe the formation of microparticles in silane plasmas during deposition of amorphous silicon.[8] Dust

particles are generally first generated either through erosion of materials in the reactor, or through gas-phase chemistry nucleation processes.[4] The discharges used in semiconductor device fabrication are typically at low gas pressures (tens to hundreds of mTorr) with electron densities of 10^9-10^{11} cm^{-3}. Boufendi et al. have demonstrated that particles grow in three distinct phases during gas-phase nucleation: initial crystallization, coalescence, and molecular sticking. A plot of some of their experimental results is shown in Figure 1.1. (All figures and tables appear at end of chapter.) The first stage of growth is attributed to nanometer-size crystallites.[9] As the concentration of these crystallites increases, they begin to coalesce into particles. Once they grow larger than 5 nm, they begin to charge negatively, continuing to increase in size to about 20 nm. At this stage, the particulates' negative charge prevents them from further coagulation, and the final stage of growth is due to molecular sticking of neutral atoms and radicals on the surface of the particles. The generation rate of particulates can be very high. Concentrations as high as 10^8 particles/cm^3 on the order of 100 nm in size have been observed after only 1 s of plasma operation in a helium-diluted silane discharge.[10]

Dust particles collected from surfaces in these reactors are often clusters or agglomerates of smaller, mono-disperse "primary" spherical particles.[11-13] These observations imply that particles first grow to a terminal size in the nucleation phase and then agglomerate to form larger structures. During nucleation, the coulombic repulsion prevents the small particles from agglomerating. Once they reach sizes of several tens to hundreds of nanometers, however, it is possible for the particles to have sufficient kinetic energy to overcome the electrostatic potential between them and agglomerate into the larger structures.

Dust particles are often observed to reside in ring- or dome-like layers near the surfaces of the reactors. Various forces in the reactor affect the transport of the contaminants. At some

locations, the sum of these forces may be zero, suspending the particles in trapping sites. The dominant forces exerted upon dust particulates under typical processing operating conditions are electrostatic and ion-drag forces.[14-15] These forces and others will be discussed in more detail in Chapter 2.

Several investigators have developed experimental techniques for detecting particles and measuring their properties.[8-13,16-17,19-22] Spears et al. and Selwyn have used laser light scattering (LLS) techniques to detect the presence of dust particles in reactors.[8,16] These techniques are useful for viewing particles larger than about 200 nm.[17] The minimum detection size is limited by the r^6/λ^4 variation of the Rayleigh scattering cross section, where r is the size of the detection target and λ is the wavelength of the light source. The lasers typically used in such experiments produce light in the visible range. Wavelengths are generally on the order of a few to several hundred nanometers. Recently, there have been many efforts to develop *in situ* particle monitors (ISPMs) based on this detection method to measure particle contamination in plasma reactors. Currently, such measurement devices are difficult to integrate into a manufacturing process. External light sources require access ports such as windows built into the reactor. Oftentimes, such access is not practical in the design of these reactors. The laser sources used in such experiments are not generally able to withstand the harsh temperatures and corrosive species in typical commercial etching and deposition vacuum reactors, and therefore cannot be placed inside the etching/deposition chamber itself.[1] Instead, these types of sensors are often placed in the exhaust lines of vacuum tools in an attempt to gather particles that are carried out by the processing gases.[18]

A typical LLS experiment is depicted in Figure 1.2.[16] The laser light is rastered across the substrate surface in the reactor and the scattered light is then collected by a CCD video camera or

photomultiplier. A photograph of a scattered light image from one of Selwyn's experiments is shown in Figure 1.3, looking toward the laser light source from across the reactor. The illuminated portions of the photo show the light scattered off the dust particles. The trapped particles can clearly be seen in ring-shaped clouds over the surfaces of the silicon wafers. Again, the particles are transported to these regions and are subsequently suspended there because of the balancing of forces in these regions. Selwyn et al. have also demonstrated that topographical features on the surface of the substrate can affect the locations of these trapping sites.[16]

Other measurement techniques have been developed recently to detect smaller particles and examine the morphology of these contaminants more closely. Haaland et al. and Garscadden et al. have used scanning electron microscope (SEM) and transmission electron microscope (TEM) techniques to view the dust contaminants, on a high-resolution scale on the order of tens to hundreds of nanometers, collected from various radio-frequency (RF) discharges. They found narrow size distributions in the dust population, and that the morphology resembled microscopic "cauliflowers" (Figure 1.4).[12-13] Stoffels et al. detected particles by heating them with a laser and measuring the resulting black body radiation.[19] They determined that in an Ar/CCl_2F_2 RF discharge, the primary source of particle contamination was the silicon substrate surface. They also concluded that small vertical structures formed on the silicon surface during the etch process broke away from the substrate surface and were introduced into the plasma as macroscopic particulates.[20] Boufendi et al. have developed a complementary technique which uses laser induced particle explosive evaporation to detect particles in the first crystalline phase (2 nm size).[9] Using this method, they found that the formation of these crystalline structures is highly dependent on gas temperature. In their experiment, Boufendi and his colleagues were able to demonstrate that higher ambient gas temperatures around 120 ºC and above delayed the formation of

crystallites, although it was not enough to prevent their generation. Boufendi's results are highly dependent on the fact that the experiment was performed in a silane discharge. Other gas chemistries may use very different chemical mechanisms in particulate growth. Howling et al. used ion mass spectrometry in a pure silane plasma to determine that negative ions are the precursors to particulate formation in such discharges.[21]

Several authors have developed numerical models to study the transport and plasma-particle interactions in plasma reactors.[22-25] Boeuf et al. developed a particle-in-cell Monte Carlo (PIC-MC) model which predicted the charge and floating potential on dust particles, given an *a priori* set of discharge conditions and particle concentration and size, as well as a 2-D fluid model to simulate the transport of particulates in the reactor.[22] These studies confirmed the existence of electrostatic trapping sites and showed that the location of these traps was highly sensitive to the electrode configuration. Goree has performed simulations examining the electrostatic charging of particles of various sizes in a variety of plasma conditions based on orbital-limited theory. He also included the reduction of charge on particles due to a high particle density, as well as electron emission off the surface of the dust particles. Based on these studies, Goree has proposed that inducing a positive charge on dust particulates through enhanced electron emission can be a useful means of controlling contamination. The amount of electron emission can be increased by heating the electrons in the discharge, perhaps by operating at low pressures or by using an external heat source.[23] Graves et al. have introduced another model, which calculates the various forces acting upon the dust particles as well as the sheath structure around each particle, assuming that the dust concentration is low enough to ignore particle-particle and particle-plasma interactions.[24] They found that under most conditions, particles were heated to the neutral gas temperature in plasma reactors. However, in some high-density tools such as electron cyclotron resonance (ECR) sources, particles could be heated to two to three times the gas temperature. Particles in such discharges were also not trapped as effectively, due to the large ion-drag forces acting upon them. The 2-D model of Choi and Kushner also calculates the forces exerted on the particles, and further

integrates their equations of motion to predict the resulting trajectories.[25] Using this model, they generated electron-dust and ion-dust momentum transfer and collection cross sections. They found that these cross sections increase with particle size and electron temperature, and approach the geometrical cross section of the particle asymptotically.

To this point, there have been no computational models that investigate particle-particle interactions during the agglomeration phase of growth. Very little is understood about the growth mechanisms associated with particle agglomeration and the reasons behind the morphologies commonly observed in etching reactors. This topic is the focus of the present thesis. The motivation for this computational study is to accomplish two goals: to develop models of the physical mechanisms in particle agglomeration, and to use these models to identify operating conditions favorable to controlling the growth and amount of dust contaminants in plasma manufacturing tools. A numerical simulation based upon the original model of Choi and Kushner has been further developed to examine the agglomeration phenomenon and determine the discharge conditions favorable to this stage of growth. A new molecular dynamics (MD) simulation has additionally been developed to examine the evolution and morphologies of dust particulates growing in a discharge. A description of the models is given in Chapter 2, and results and analysis of the simulation are presented in Chapter 3. Finally, some conclusions are drawn in Chapter 4.

It seems that, in general, higher operating powers lead to larger ion-drag forces which overwhelm the electrostatic forces to some degree. As the RF power deposition in the discharge increases, contaminants are driven further through the sheath regions and eventually reach the surfaces of the reactor. This is true for particles of all sizes, although larger dust particles are more sensitive to these ion-drag forces.

The agglomeration phenomenon and the resulting dust morphology are highly dependent on the collision velocity of the agglomeration partners, as well as their respective sizes. Both higher velocities and larger masses result in greater kinetic energies. This is favorable for agglomeration. Higher kinetic energies relative to the electrostatic potential between two

approaching particles results in more compactly shaped agglomerates. Lower kinetic energies, if still sufficient for agglomeration, produce morphologies with low fractal dimension.

Typically, neutral gas flow, if fed laterally across the substrate surface, can be very useful for controlling contamination in the reactor. This does not decrease the amount of contamination in the reactor (in fact it can increase the agglomerate density), but at sufficient flow rates, the feed gas flow can sweep particles away from sensitive regions of the reactor toward the exhaust port.

1.1 Figures

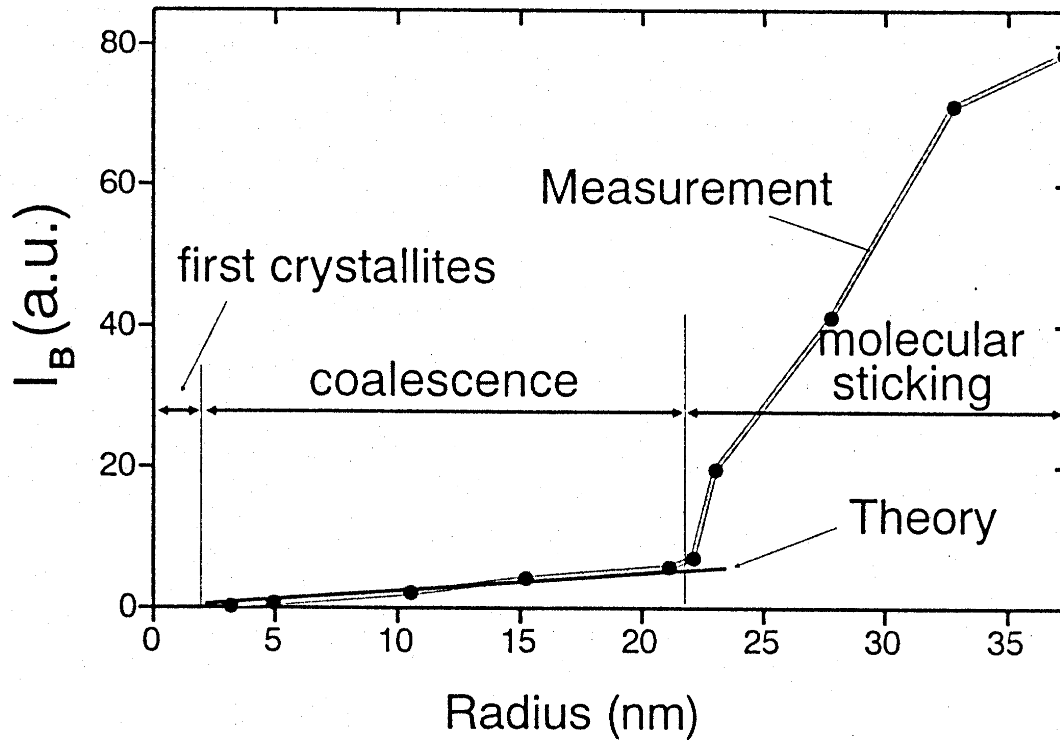

Figure 1.1. Emission intensity from a laser-induced particle explosive evaporation (LIPEE) experiment as a function of RF plasma discharge duration for a 1.2 sccm silane flow. The intensity indicates the relative size of the particles.[9]

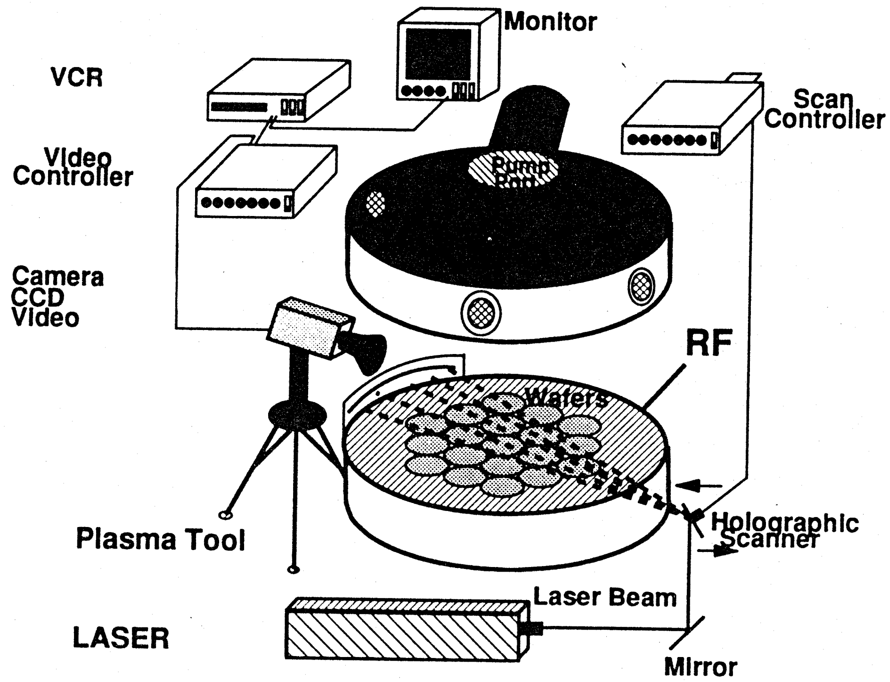

Figure 1.2. Schematic diagram of a typical laser light-scattering (LLS) particle detection experiment.[16]

Figure 1.3. Photograph of scattered laser light from an LLS experiment.[16] The laser light is rastered across the surface of three silicon wafers in a plasma reactor.

Figure 1.4. Scanning electron micrograph (SEM) of a dust particle collected in a 1 Torr 15 kHz helium plasma with graphite electrodes. The particle is 650 nm in diameter.[13]

1.2 References

[1]J. R. Mitchell and B. A. Knollenberg, Semicond. Int. **19**, 145 (1996).

[2]S. J. Choi and M. J Kushner, Appl. Phys. Lett. **62**, 2197 (1993).

[3]P. Singer, Semicond. Int. **18,** 46 (1995).

[4]T. Francis, Semicond. Int. **16**, 62 (1993).

[5]C. K. Goertz, Rev. Geophys. **27**, 271 (1989).

[6]R. J. Gould and E. E. Salpeter, Astrophys. J. **138**, 393 (1963).

[7]F. Hoyle and N. C. Wicksramasinghe, *The Theory of Cosmic Grains* (Kluwer, Dordrecht, Holland, 1991).

[8]K. G. Spears, T. M. Robinson, and R. M. Roth, IEEE Trans. Plasma Sci. **PS-14**, 179 (1986).

[9]L. Boufendi, J. Hermann, A. Bouchoule, B. Dubrueil, E. Stoffels, W. W. Stoffels, and M. L. de Giorgi, J. Appl. Phys. **76**, 148 (1994).

[10]Y. Watanabe, M. Shiratani, and M. Yamashita, Appl. Phys. Lett. **61**, 1510 (1992).

[11]J. F. O'Hanlon, R. N. Carlile, M. P. Garrity, and S. M. Collins (private communication, 1996).

[12]P. D. Haaland, A. Garscadden, B. N. Ganguly, S. Ibrani, and J. Williams, Plasma Sources Sci. Technol. **3**, 381 (1994).

[13]A. Garscadden, B. N. Ganguly, P. D. Haaland, and J. Williams, Plasma Sources Sci. Technol. **3**, 239 (1994).

[14]T. J. Sommerer, M. S. Barnes, J. H. Keller, M. J. McCaughey, and M. J. Kushner, Appl. Phys. Lett. **59**, 638 (1991).

[15]M. S. Barnes, J. H. Keller, J. C. Forster, J. A. O'Neill, and D. K. Coultas, Phys. Rev. Lett. **68**, 313 (1992).

[16]G. S. Selwyn, Plasma Sources Sci. Technol. **3**, 340 (1994).

[17]D. S. Lemons, R. K. Keinigs, D. Winske, and M. E. Jones, Appl. Phys. Lett. **68**, 613 (1996).

[18]K. Takahashi and J. Daugherty, J. Vac. Sci. Tech. **14**, 2936 (1996).

[19]E. Stoffels, W. W. Stoffels, G. M. W. Kroesen, and F. J. de Hoog, *Proceedings of the IXth Symposium E.P.C.R.L.T.P.*, Pila, Czecho-Slovakia, 1992 (unpublished), p. 132.

[20]W. W. Stoffels, E. Stoffels, G. M. W. Kroesen, M. Haverlag, J. H. W. G. den Boer, and F. J. de Hoog, Plasma Sources Sci. Technol. **3**, 320 (1994).

[21]A. A. Howling, L. Sansonnens, J-L Dorier, and Ch. Hollenstein, J. Phys. D: Appl. Phys **26**, 1003 (1993).

[22]J. P. Boeuf, Ph. Belenguer, and T. Hbid, Plasma Sources Sci. Technol. **3**, 407 (1994).

[23]J. Goree, Plasma Sources Sci. Technol. **3**, 400 (1994).

[24]D. B. Graves, J. E. Daugherty, M. D. Kilgore, and R. K. Porteous, Plasma Sources Sci. Technol. **3**, 433 (1994).

[25]S. J. Choi, and M. J. Kushner, IEEE Trans. Plasma Sci. **22**, 138 (1994).

2. MODEL DESCRIPTION

2.1 Introduction

A series of models has been developed to investigate the problem of dust contamination in etching reactors. Specifically, the first of these models, the Hybrid Plasma Equipment Model, computes relevant plasma parameters by solving Maxwell's equations as well as the continuity, momentum, and energy equations in the reactor under a given set of discharge conditions. These parameters are then used by the next model, the Dust Transport Model (DTS), to compute the forces exerted upon dust particles throughout the reactor. The DTS then integrates the classical equations of motion to calculate the resulting trajectories of the dust particulates. Finally, the velocities and trajectories of the dust particles are used by the Particle Agglomeration Model (PAM) and its Molecular Dynamics extensions (MD-PAM) to simulate the Coulombic interaction between particles and the resulting agglomeration. The objective in using these models is to self-consistently simulate the growth and transport phenomena associated with these dust particles after their generation in the reactor. By doing so, I hope to gain some insight into the physical mechanisms involved in these phenomena, as well as discover some general scaling laws which couple the size and amount of particle contamination to discharge parameters.

In this section, a detailed description of the three models is presented. This begins with a description of the Hybrid Plasma Equipment Model,[1] followed by a description of the Dust Transport Model. The latter is based on a transport model originally developed by Choi and Kushner.[2] A description of the new Particle Agglomeration Model (PAM) and its complementary Molecular Dynamics simulation (MD-PAM) is then given. A block diagram of the hierarchy of models discussed in this thesis is given in Figure 2.1.

2.2 The Hybrid Plasma Equipment Model (HPEM)

The Hybrid Plasma Equipment Model is a modular, two-dimensional numeric simulation of plasma etching and deposition tools. It is a hybrid model consisting of three primary modules: an electromagnetics module, an electron Monte Carlo simulation, and a fluid-chemical kinetics model. In addition, there is an additional plasma chemistry Monte Carlo simulation, a plasma sheath model, and an etching profile model.[1] A schematic of the various modules in the HPEM is given in Figure 2.2. Before running the HPEM codes, a rectilinear geometry is defined using a separate mesh generator program. Materials and their properties (e.g., conductivity, dielectric permittivity) in the reactor are also declared at this stage. The HPEM is then used to compute the coil-generated electric and magnetic fields in the electromagnetics module (EMM) throughout this defined mesh. The electron temperature, transport coefficients, and source functions are determined in the electron Monte Carlo simulation (EMCS), where the electron trajectories and resulting collisions are followed for many tens of RF cycles. This information is then passed on to the fluid-chemical kinetics simulation (FKS), which generates electrostatic fields, conductivities, and species densities. These modules are coupled together in an iterative fashion to arrive at a steady-state solution. Once these models are converged, the source functions and electrostatic fields are passed to the plasma chemistry Monte Carlo simulaton (PCMCS) to produce ion fluxes and energy distributions.

A typical reactor configuration is depicted in Figure 2.3, although the HPEM allows the user to generally specify the reactor's topography and material properties. Industrial etching reactors are typically cylindrical in shape, with a parallel plate electrode geometry. Additional reactor-specific features may be present, such as a showerhead-type gas inlet, or magnetic multipoles used for confining the plasma. For the purpose of our experiments, I have chosen a

reactor geometry which includes a showerhead-type grounded electrode at the top of the chamber, with a powered electrode at the bottom of the reactor. A wafer used for processing in such a reactor would reside on top of this powered electrode. Feed gases are introduced to the chamber through the showerhead. The exit pump port is an annular region surrounding the bottom electrode. Additional substrate topographies were also used, including grooves in the electrode surface, and a metallic dark space shield surrounding the bottom electrode. The purpose of these additional geometries is to investigate their effect on the transport of dust particulates. A detailed discussion of the HPEM model is given in Ventzek et al.[1] but will be briefly described in the following sections.

2.2.1. The electromagnetic module (EMM)

The electromagnetics module calculates the electric and magnetic fields in the plasma that are generated in the reactor. The azimuthal electric field E_θ is computed by solving the complex wave equation

$$\nabla^2 E_\theta(r,z) = i\omega\mu_0\sigma(r,z)E_\theta(r,z) \tag{2.1}$$

where the field is assumed to be purely sinusoidal, and ω is the driving frequency. The magnetic permeability of the medium is represented by μ_0, and σ(r,z) is the spatially dependent electrical conductivity. The equation is solved for in cylindrical coordinates over the volume of the discharge using a successive-over-relaxation (SOR) method. The boundary conditions imposed upon the equation are that $E_\theta=0$ on metal surfaces in the reactor and on the axis ($r=0$). This implies that the field is purely azimuthal, and that the walls of the chamber and wafer holder are metallic conductors. Once the electric field is obtained, the magnetic field is computed from Maxwell's equations:

$$B(r,z) = (i\,/\,\boldsymbol{w})\nabla \times E \qquad (2.2)$$

2.2.2 The electron Monte Carlo simulation (EMCS)

The EMCS uses the electric and magnetic fields computed in the EMM and FKS to track the trajectories of electrons in the discharge. Electrons are initially distributed uniformly throughout the reactor, and their initial velocities are selected from a Maxwellian distribution. Their trajectories are then calculated using a second order integration. Acceleration of the particles is interpolated as a function of position and phase from the electric and magnetic fields. The electron energy distribution function (EEDF) and collision probabilities for all relevant electron impact processes (ionization, excitation, momentum transfer collisions, etc.) are used in simulating the production and loss of various excited and charged species. The time step used in the calculation of these trajectories for a pseudoparticle *j* is defined as

$$\Delta t_j = \min(0.01\boldsymbol{t}_{\mathrm{rf}}, 0.01\boldsymbol{t}_{\mathrm{ECR}}, t_{cl} - t_j, \Delta t_{rz}/4) \qquad (2.3)$$

where t_j is the time for particle *j* before it is advanced, $\boldsymbol{t}_{rf}$ is the radio frequency period, $\boldsymbol{t}_{ECR}$ is the local electron cyclotron period, t_{cl} is the time of the next collision event, and $\boldsymbol{D}t_{rz}$ is the time taken to cross the local spatial mesh cell.

Null collisions and particle scattering are included in this module and are described in Sommerer et al.[3] and Weng et al.[4] The trajectories of electrons are computed for several (≈ 20-50) RF cycles. At the end of this simulation, source functions for all electron impact processes are computed from the time averaged EEDF, and passed on to the fluid-chemical kinetics simulation.

2.2.3 The Fluid-Chemical Kinetics Simulation (FKS)

The FKS module uses the electron impact source functions and transport coefficients calculated in the EMCS and solves the continuity equations for all charged and neutral species, as well as Poisson's equation:

$$\frac{\partial N_j}{\partial t} = \nabla\left(\mu_j q_j N_j E_s - D_j \nabla N_j\right) + \left(\frac{\partial N_j}{\partial t}\right)_c \qquad (2.4)$$

$$\nabla \cdot E_s = -\nabla^2 \Phi = \frac{\rho}{\varepsilon_0} \qquad (2.5)$$

where μ_j is the mobility, D_j is the diffusion coefficient, N_j is the density, q_j is the charge for a species j, E_s is the electrostatic field, Φ is the electrostatic potential, and ρ is the charge density. The last term on the right-hand side in Equation (2.4) includes production and depletion of species due to heavy particle collisions and electron impact processes alike.

The FKS is given some initial estimates of the species densities and then iterated with the other modules in the HPEM until convergence is achieved. Generally, depending on the accuracy of the initial guesses, the HPEM may require tens to hundreds of microseconds of simulation time to achieve convergence. Because of the computational intensity of such a simulation, an acceleration technique, described in Ventzek et al.,[1] is employed to improve the accuracy of the initial species densities used in the FKS.

2.3 The Dust Transport Simulation (DTS)

As mentioned in Chapter 1, there are various mechanical and electrical forces in plasma tool reactors that act upon dust contaminants. These forces, including electrostatic, ion-drag, neutral drag, thermophoretic, self diffusion and gravitational, govern the transport of particulates. Under typical operating conditions in etching reactors, the predominant forces are electrostatic and ion-drag. Electrostatic forces are exerted upon the negatively charged particles by the electric fields in the discharge. This force, then, typically drives particles toward the peak of the plasma potential in the discharge, near the center. Ion-drag forces result from momentum-transfer collisions between positive ions and the heavier dust particles, and accelerate the dust particulates in the direction of net ion flux, usually towards the surfaces of the reactor. Fluid drag results from

the entrainment of the dust particles in the bulk gas flow of the reactor, which carries them towards the exhaust port. This force can play a large role in the transport of dust particles since often the feed gases flow in a direction normal to the electrostatic and ion-drag forces. Thermophoretic forces push particles down temperature gradients in the discharge, while self-diffusion acts along density gradients. The trapping sites discussed in Chapter 1 appear at locations where the sum of these forces is equal to zero. A general diagram of these forces in a typical parallel plate reactor is shown in Figure 2.4.

The DTS is a two-dimensional Monte Carlo model which uses the temperatures, fluxes, and electrostatic fields generated by the HPEM to compute the forces discussed above and their resulting trajectories and velocities. The DTS begins with a collection of pseudoparticles scattered throughout the reactor with a predetermined spatial and size distribution. The particles are given an initial velocity of zero. The reactor forces are then calculated, and the particles' equations of motion are integrated to second order. Relevant plasma parameters are interpolated between mesh points. The force on a dust particle i with radius r_i and mass M_i is given by Choi et al.:[6]

$$F_i(r) = M_i g + q_i E + \int \sigma_m \phi_I(r, v_I) \left| v_I \right| dv_I - \frac{6\pi\mu r}{C(Kn)}(v_i - u) \cdot C_D(Re_p)\frac{Re_p}{24} - 6\pi\mu r_i v K_T \cdot \frac{\nabla T}{T} \quad (2.6)$$

The terms on the right hand side of Equation (2.6) represent the gravitational, electrostatic, ion-drag, fluid drag, and thermophoretic forces, respectively. Here, g is the gravitational acceleration, q_i is the charge on the particle, E is the electric field, σ_m is the ion momentum transfer cross section, v_i, v_I and u are the dust, ion, and fluid velocities, respectively, and ϕ_I is the ion flux. The expression used for the ion momentum cross section is that derived by Kilgore et al:[5]

$$\sigma = c_1 \ln\left[1 + \left(c_2 \Big/ \left(b/\lambda_D{}^2\right)^2\right)\right] \quad (2.7)$$

where b is the collision length. This is the impact parameter corresponding to a 90° scattering angle, and is defined as

$$b = Ze^2 / 4\pi\varepsilon_0 E_+ \qquad (2.8)$$

where Z is the number of charges on the particle, e is the elementary electronic charge, and E_+ is the kinetic energy of the approaching ion. In Equation (2.7), λ_D is the linearized Debye length, defined as the effective shielding length for a dust particulate whose radius a is much smaller than the conventional Debye length λ. This linearized Debye length is derived by linearizing the Poisson-Vlasov Equation and is given in Kilgore et al.[5] In Equation (2.7), c_1 and c_2 are fitted constants of 0.9369 and 61.32, respectively. In the last two terms of Equation (2.6) describing the viscous fluid drag and thermophoresis, the constants C, C_D, Re_p, and K_T are derived from classical thermodynamics using a hard sphere collision assumption and are given by Choi et al.:[6]

$$C(Kn) = 1 + Kn(\alpha + \beta) \cdot \exp(-\frac{\gamma}{Kn}) \qquad (2.9)$$

$$C_D(\mathrm{Re}_p)\frac{Re_p}{24} = 1 + 0.173 \cdot Re_p^{0.657} + \frac{0.01721 \cdot Re_p}{1 + 16300 \cdot Re_p^{-1.09}} \qquad (2.10)$$

$$Re_p = \frac{2\rho r_i \left| v_i - u \right|}{\mu} \qquad (2.11)$$

$$K_T = \frac{2C_s[(k_g / k_p) + C_t Kn]}{(1 + 3C_m Kn)[1 + 2 \cdot (k_g / k_p) + 2C_t Kn]} \qquad (2.12)$$

In Equations (2.9)-(2.12), Kn is the Knudsen number defined as the ratio of the gas mean free path to the characteristic length of the reactor, Re_p is the Reynolds number (the ratio of convective versus diffusive flow), μ is the fluid viscosity, and T is the gas temperature. The constants *a, b,* and γ are experimental constants which are dependent on the gas composition and the particle surface roughness. Here, k_g and k_p are the thermal conductivities of the gas and particle, respectively. In addition, C_t, C_s, and C_m are the thermal creep coefficient, temperature jump

coefficient, and velocity jump coefficient respectively. The values for these constants are given in Choi et al.[6]

The surface charge of the particle is calculated based on the electron and ion temperatures in the spatial cell of the dust particle. Orbital motion limited theory dictates that the electric potential on a particle should be independent of the plasma density in that region. The particle's potential ϕ is computed by balancing the electron current I_- and positive ion current I_+ to its surface:

$$I_+ = \pi a^2 N_+ \left(\frac{2E_0}{M}\right)^{1/2} \left(1 - \frac{q\phi}{E_0}\right) \tag{2.13}$$

$$I_- = \pi a^2 N_- \left(\frac{8kT_e}{\pi m}\right)^{1/2} \exp\left(\frac{q\phi}{E_0}\right) \tag{2.14}$$

where a is the radius of the particle, N is the bulk plasma density, E_0 is the ion energy, which is assumed to be monoenergetic, and M and m represent the ion and electron masses, respectively. From Equations (2.13) and (2.14), the particle potential can be calculated, assuming that the total negative charge density of dust particles in this region is much less than the plasma density.

The particles, once released in the simulation, are tracked continuously until a steady-state condition is reached. Particles may be lost throughout the simulation as they are collected on surfaces in the reactor. Therefore, the DTS allows for a constant refreshing of pseudoparticles to maintain the total particle inventory. The DTS simulation is continued until particles have reached a quasi-steady state. The condition of steady state is defined as being reached when there is a constant flux of particles to the trapping locations.

2.4 The Particle Agglomeration Model (PAM)

The Particle Agglomeration Model uses the Dust Transport Simulation as a point of departure. It uses the same algorithms and methodology to calculate the forces on the particles and advance their trajectories, but additionally includes particle-particle interactions using particle-

mesh Monte Carlo methods. During the simulation of the dust transport, the pseudoparticles are periodically “binned” onto the numerical mesh to provide an instantaneous dust particle density in each cell. These densities are then used to compute collision frequencies between all pseudoparticles in that cell, based on the overlap of the particles’ Debye-Hückel shielding volumes (see Figure 2.5). Monte Carlo techniques are then used to determine the occurrence of a particle-particle collision, based on the time interval between binnings and the calculated particle collision frequencies. A given pseudoparticle collides with one of the other pseudoparticles in the spatial cell if

$$\Delta t \geq -\frac{\ln(r)}{\boldsymbol{n}_D} \tag{2.15}$$

where $\boldsymbol{D}t$ is the time between binning, r is a random number between zero and one, and $\boldsymbol{n}_D$ is the calculated particle collision frequency. The collisional cross section between two dust particles is defined as

$$\boldsymbol{s} = \boldsymbol{p}\,(r_{tot1} + r_{tot2})^2 \tag{2.16}$$

where r_{tot1} and r_{tot2} are the total radii of the two Debye-Hückel bodies, *i.e.*, the sum of the physical radius of the particle and the linearized Debye length. The collision frequency, then, between these two particles is given by

$$\boldsymbol{u}_D = \frac{v_{rel}\boldsymbol{s}}{\mathrm{V}} \tag{2.17}$$

where v_{rel} is the relative velocity of the pair, and **V** is the volume of the mesh cell.

In the event of a “shielding volume collision,” i.e., two particles interacting coulombically, one of the other pseudoparticles in the cell is chosen as a collision partner. This collision partner

is chosen using a probability space generated on the basis of the collision frequencies, i.e., the collision partner is the pseudoparticle j which satisfies

$$\frac{\boldsymbol{n}'_{j-1}}{\boldsymbol{n}_D} \leq r \leq \frac{\boldsymbol{n}'_j}{\boldsymbol{n}_D}, \quad \boldsymbol{n}'_{\mathrm{j}} = \sum_{i=1,j} \boldsymbol{n}_j \tag{2.18}$$

Each possible collision partner represents a fractional range in the probability space, defined between zero and one. After choosing a random number r, the corresponding particle is chosen as the collision partner. With the collision pairing made, the velocities and masses of the two particles are used to calculate the center of mass kinetic energy of the collision pair $\boldsymbol{e}$. Given that the maximum repulsive electrostatic potential between the particles is

$$U = \frac{1}{4\boldsymbol{pe}_0} \frac{Q_1 Q_2}{d} \tag{2.19}$$

where Q_1 and Q_2 are the charges on the two particles, and d is their distance of closest approach, an agglomeration collision is only possible if $\boldsymbol{e} \geq U$. If this is the case, a random impact parameter is chosen to determine the occurrence of a physical collision. The impact parameter is defined as the distance of closest approach for two interacting particles. This parameter ranges between the sum of the physical radii of the two particles, to the sum of the Debye shielding lengths of the particles. Dust particles separated by a distance greater than this upper limit will not interact coulombically. The ratio of the lower and upper limits of the impact parameter is then given by

$$P = \frac{R_1 + R_2}{\left(R_1 + \boldsymbol{l}_1\right) + \left(R_2 + \boldsymbol{l}_2\right)} \tag{2.20}$$

Here, R_1 and R_2 represent the physical radius of the particles, while the sum $(R+\boldsymbol{l})$ represents the radius of the Debye sphere around the particle. This ratio describes the probability of a physical collision. A random number chosen above this value represents a physical collision between the collision pair. If a physical collision does occur, the particles agglomerate into a larger structure,

conserving total volume, mass, and momentum. Otherwise, they maintain their current velocity and trajectory, or are deflected by the electrostatic repulsive forces.

The shape of the agglomerates is an important factor in the growth process. The PAM allows for two particle shapes, spherical and cylindrical. The shape of the particle enters into the calculation of the charge on the particle given its electric potential V. The electrical potential is calculated with the same algorithm as described in Chapter 2. The effective charge Q on a particle is given by

$$Q = CV \tag{2.21}$$

where C is the particle's capacitance. For a spherically shaped particle of radius R, the capacitance is

$$C = 4\pi\varepsilon_0 R\left(1 + \frac{R}{\lambda_D}\right) \tag{2.22}$$

where λ_D is the linearized Debye length derived by Kilgore et al.[5] This capacitance is the value calculated for a spherical capacitor consisting of two concentric shells separated by a distance of λ_D, derived from first principles from Gauss's Law. For a cylindrical particle with length L and radius R, the capacitance is approximately

$$C = \frac{2\pi\varepsilon_0 L}{\ln(\lambda_D / R)} + \frac{2\pi R^2 \varepsilon_0}{\lambda_D} \tag{2.23}$$

The first term in this expression represents a capacitor consisting of two concentric cylinders separated by λ_D, while the second term approximates the capacitive contribution from the two ends of the particle.

The distance of closest approach for two colliding spherical particles is the sum of their radii. Cylindrical particles, however, can impinge at random orientations resulting in different distances of closest approach. To account for this effect, when using two cylindrical particles or one cylindrical and one spherical particle for agglomeration, a distance of closest approach is

randomly chosen based on the radius and length of the collision partners (see Figure 2.6). The shape of the resulting agglomerate depends on the orientation and shape of the colliding particles. For example, if strictly spherical particles are used, the newly formed agglomerate is simply a larger sphere whose dimensions are determined by conserving volume. If, as another example, two cylindrical particles collide in a “head to tail” orientation, the resultant agglomerate is another cylinder with an aspect ratio smaller than that of its two components (aspect ratio is defined as $\boldsymbol{G}=R/L$). The length and radius of the new cylinder is chosen in such a manner as to conserve mass based on the overlap length of the colliding particles. In doing so, either long thin cylindrical particles ($\boldsymbol{G}<<1$) or flat disks ($\boldsymbol{G}>>1$) can be formed. Like the DTS, the PAM simulation is continued until a steady-state distribution of the dust particle population is reached.

2.5 The Molecular Dynamics Simulation (MD-PAM)

The morphology of dust contaminants in plasma etching reactors can provide some insight to their growth mechanisms and provide useful information for developing means of controlling them. As mentioned in Chapter 1, dust particles collected from plasma reactors are often chain-like or “cauliflower-shaped” clusters. This structure provides some information on the history of the particle’s growth. To investigate the shapes of these dust particulates, a molecular dynamics (MD) simulation has been developed for use in conjunction with the PAM model. The MD-PAM simulates the interaction of individual charged primary particles with a growing agglomerate of arbitrary shape while considering electrostatic shielding. For the work presented, the MD-PAM is not executed in the framework of a reactor-scale particle transport mode, as is the previously described PAM. Particle velocity distributions from the reactor-scale simulation are used in the MD-PAM, however. Specific plasma conditions such as electron and ion densities and temperatures are read in as inputs to the model, as are the mass density and radius of the dust primary particle. A “primary particle” in this context is defined as a particle of a given dimension and material, which is the smallest dust particle allowed in the reactor. This represents a dust particle which, through the nucleation process, has already evolved to a certain size. Generally,

primary particles are tens to hundres of nanometers in size. Agglomerates are grown by joining together primary particles. Only spherically shaped primary particles are considered.

Given the size and shape of a primary particle, as well as its dielectric constant and the density and temperature of the charged species in the surrounding plasma, the equilibrium electrical charge on the particulates is calculated in the same manner as in the DTS. A velocity vector is specified for each of the two reactant particles (either two primary particles, a primary particle and an agglomerate, or two agglomerates), either predetermined or randomly selected from a given velocity distribution. To simulate a free-moving particle i approaching another particle j suspended at a trapping location, an option is provided in the MD-PAM to artificially increase the weight of particle j so that it remains relatively still in the simulation. A collision location is then chosen and the particles are "backed off" along the reverse trajectory of their initial velocity vectors to starting locations where the repulsive electric potential between the particles is less than one percent of its value when the particles are in physical contact with each other. This is illustrated in Figure 2.7. An impact parameter is then randomly chosen between zero and the sum of the "radii" of the two particles. (In the case of an agglomerate particle, the "radius" is the maximum distance between the center of mass and any of its constituent primary particles.)

The trajectories of the particles are then integrated forward in time, accounting for the plasma-shielded electrical force between them. A third-order Runge-Kutta technique, having an adaptive time step, is used for this purpose. The particles agglomerate if they come into physical contact with each other. In the event of an agglomeration, the particles are joined at their point of contact to form a larger particle. This process is then repeated in another trial, choosing different initial velocities and/or impact parameters. If an agglomeration does not occur after a specified number of trials (typically tens of thousands), it is declared that these particular plasma conditions do not support agglomerates larger than that already created. A maximum size the agglomerate can grow to, in units of primary particles, is also typically set; for the results shown in Chapter 3, this limit was set to 150. Generally, if a particle grows to this limit, it will continue to grow in the discharge. The mechanical forces which bind primary particles together in the agglomerate are not

resolved. As a result, once attached in the agglomerate, it is assumed that the spatial coordinates of each primary particle are fixed with respect to the agglomerate's center of mass. That is, the agglomerates are forced to be rigid bodies.

The simulation typically begins with two primary (monomer) particles and the agglomerate is built by adding additional monomer particles. The orientation of the agglomerate during this building process is important in determining the propensity for agglomeration since the incident primary particle experiences a different force depending on the local morphology. To account for this effect, Eulerian angles are randomly chosen for the agglomerate about its center of mass before integrating its trajectory forward in time.

As previously mentioned, the electrostatic force between two particles may be diminished somewhat due to the shielding of their respective electric charges, especially among larger agglomerates. If the size of the agglomerate is on the order with the shielding length (in this case the linearized Debye length[5]), a primary particle approaching the agglomerate from one end may not "see" the charge at the other end. A rigorous analysis of this phenomenon would require dynamically solving the 3-D Poisson's equation in the vicinity of the agglomerate, accounting for electron and ion motion in that region. Such a solution is beyond the scope of this work. The shielding effect is approximated by using an effective charge for each primary particle in the force equation of the colliding particles. For example, the force on a primary particle j approaching an agglomerate with i constituent primary particles is:

$$\boldsymbol{f}_j = \frac{1}{4\pi\varepsilon_0} \sum_i \frac{Q_j Q_i' (\mathbf{r_i} - \mathbf{r_j})}{r_{ij}^3}, r_{ij} = \left| \mathbf{r_i} - \mathbf{r_j} \right| \qquad (2.24)$$

where $\mathbf{r_i}$ and $\mathbf{r_j}$ are the spatial coordinates of particles i and j respectively. The effective charge Q_i is defined as

$$Q_i'(r_{ij}) = Q_i\left(1 - \frac{\int_R^{r_{ij}} 4\pi r^2 \exp(-r/\lambda_D)dr}{\int_R^{\infty} 4\pi r^2 \exp(-r/\lambda_D)dr}\right) \tag{2.25}$$

where R is the radius of the primary particle, λ_D is the shielding distance, and Q_i is the unshielded primary particle charge. This effective charge on the target dust particle being approached by a projectile particle accounts for charge shielding effects. A portion of the surface charge on the target is not "seen" by the projectile particle because it is shielded by the space charge region separating this collision pair. The effective charge on the target is derived by integrating the space charge region between the two particles and subtracting it from its unshielded charge. From Equation (2.25), we see that the effective charge is always less than the unshielded charge. An approaching particle would see a somewhat diminished amount of surface charge on a target particle from distances farther than a shielding length away. Therefore, the approaching particle would be able to carry more inertia into the collision, increasing the probability of agglomeration.

The MD-PAM retains a complete description of each particle during the simulation. This includes the spatial location of the center of mass, as well as the spatial coordinates of each primary particle in the agglomerate relative to its center of mass. In addition, the particle's center of mass velocity is recorded (see Figure 2.8). The unshielded charge of each primary particle is assumed to be fixed since the plasma density and temperatures are held constant in the collision region.

2.6 Figures

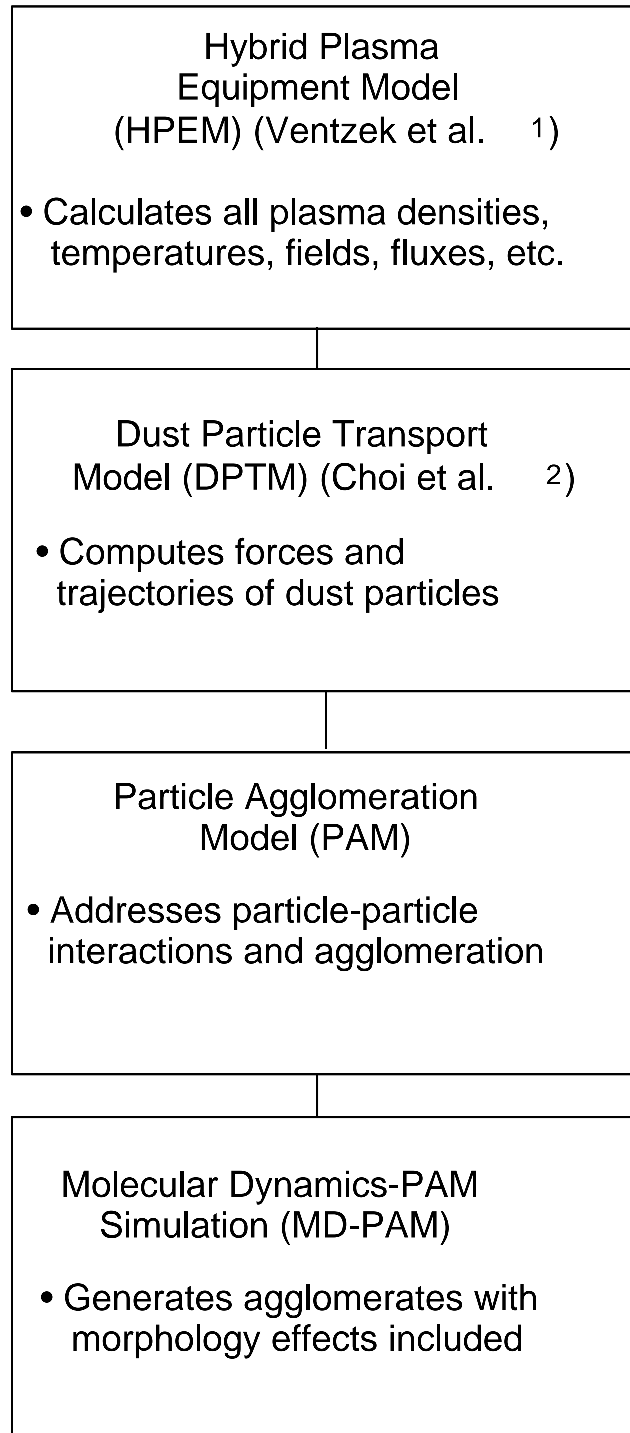

Figure 2.1. Block diagram of relevant models.

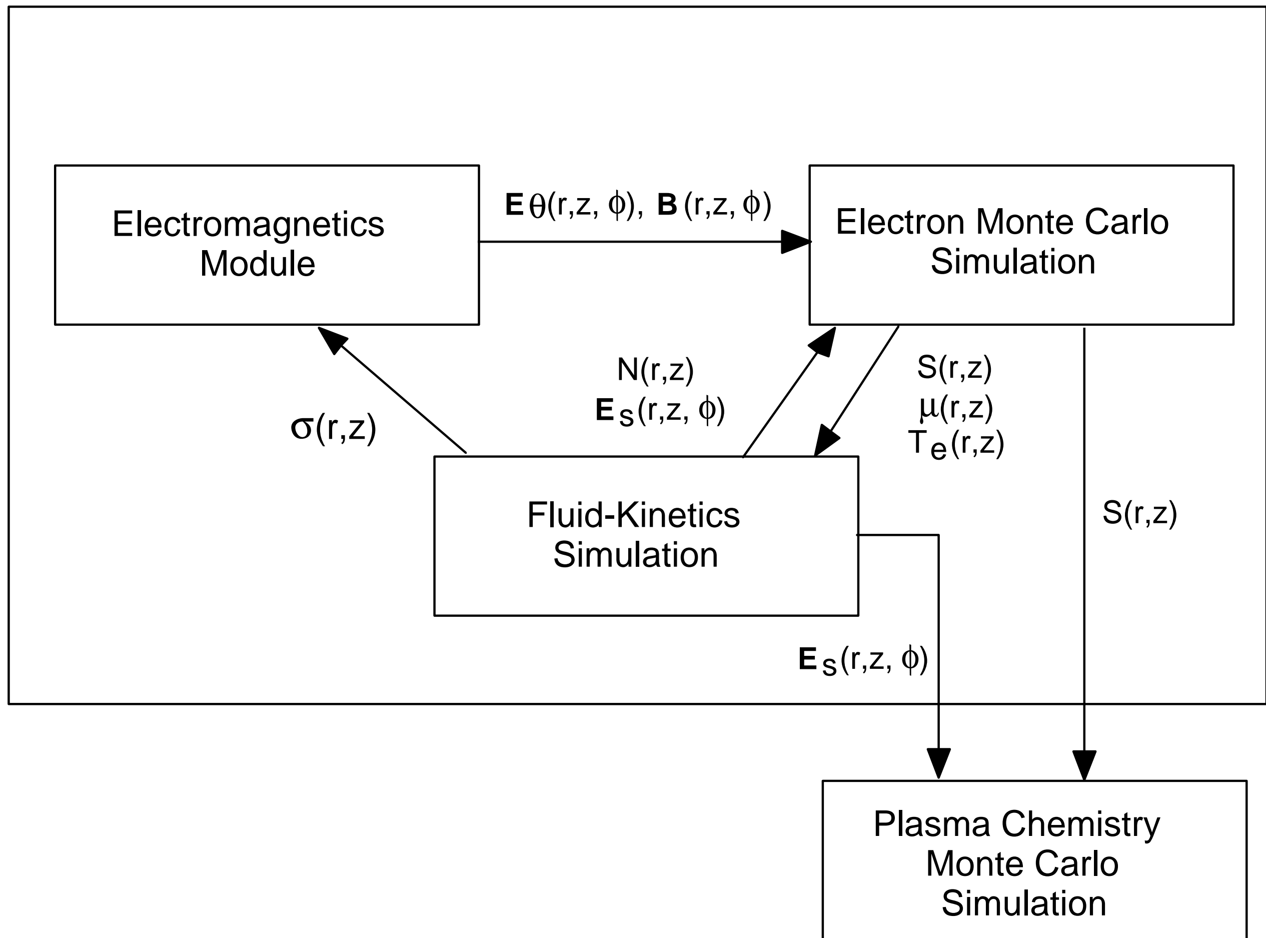

Figure 2.2. Schematic of the computational modules comprising the Hybrid Plasma Equipment Model (HPEM).

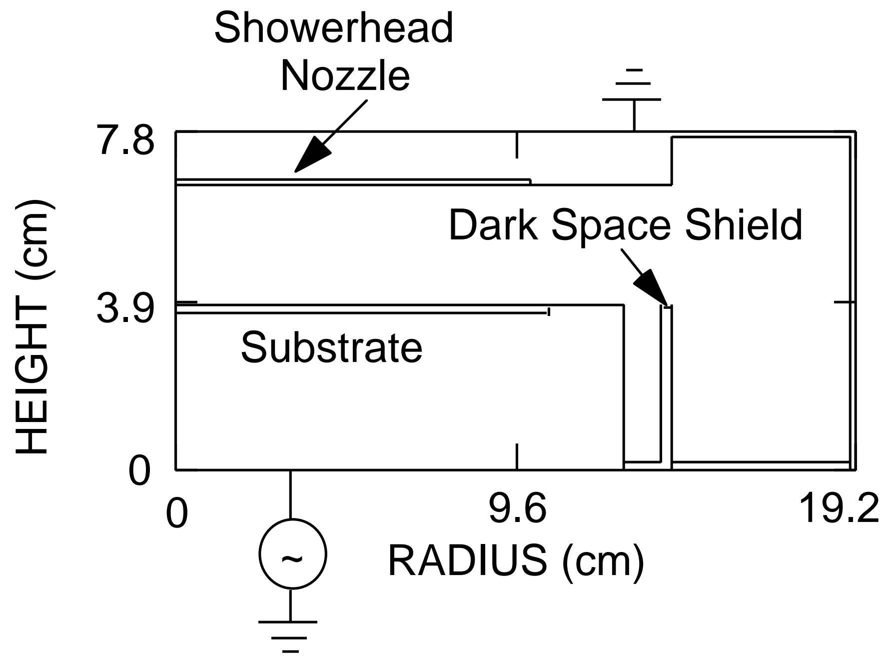
Showerhead
Nozzle
7.8
3.9
0
HEIGHT (cm)
Dark Space Shield
Substrate
0
9.6
19.2
RADIUS (cm)
~

Figure 2.3. Schematic diagram of reactor geometry used for results in Chapter 3, Section 3.1. The reactor includes a showerhead gas inlet in the grounded electrode, and various electrode geometries and features in the powered electrode.

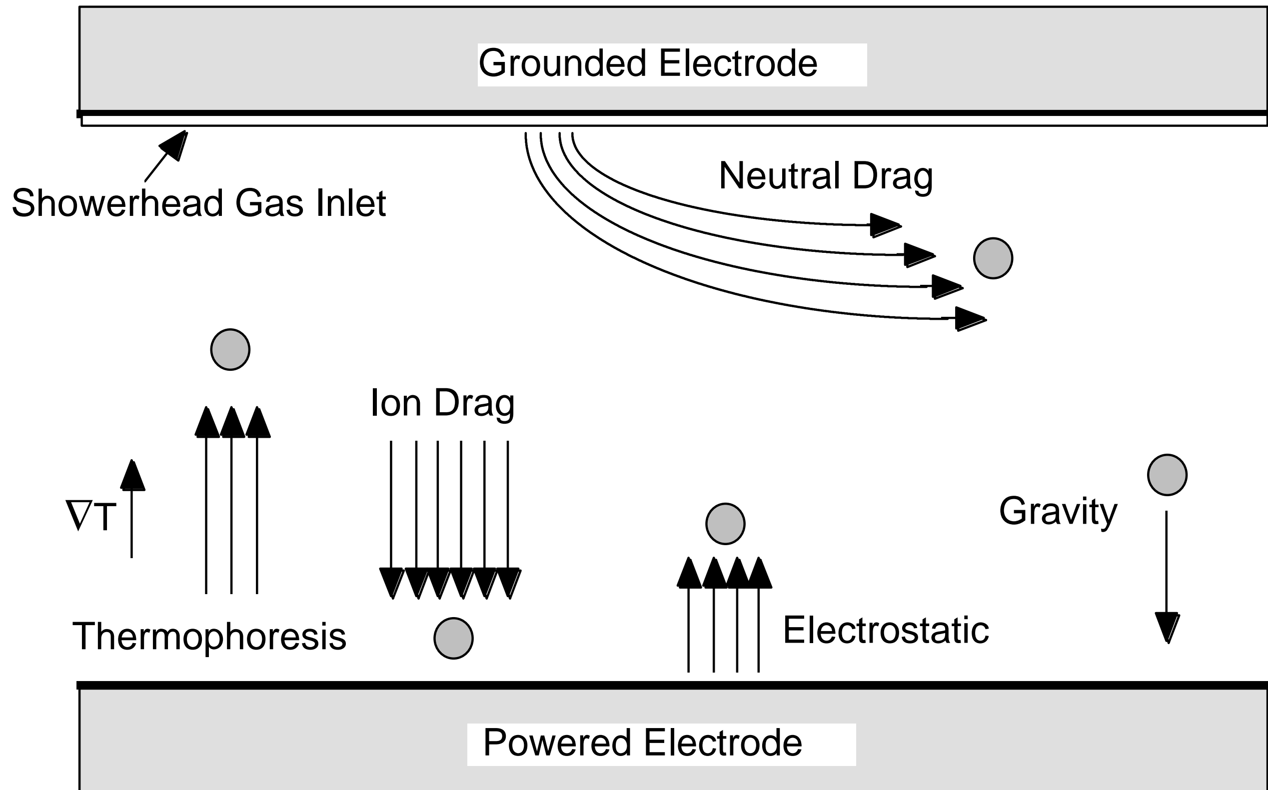

Figure 2.4. The primary forces in a typical low temperature low pressure plasma reactor. Electrostatic and ion-drag forces are the dominant forces under normal operating conditions.

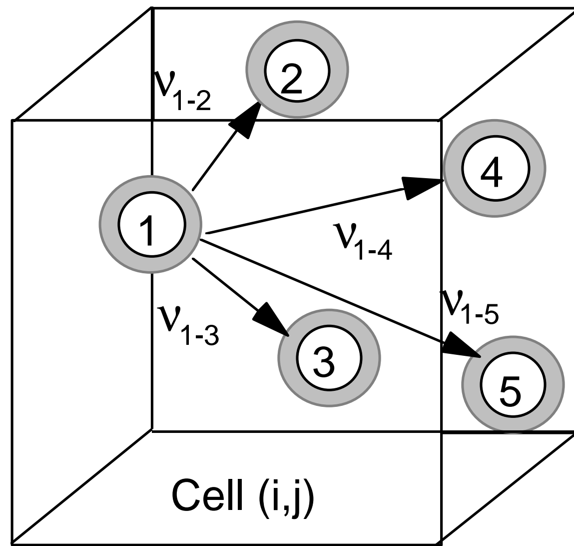

Figure 2.5 Pseudoparticles in a computation cell (i,j) are statistically collected during the simulation. Collision frequencies are computed between all pseudoparticles based on their Debye-Hückel shielding volumes. In this example, there are five pseudoparticles and four collision frequencies calculated for each pseudoparticle.

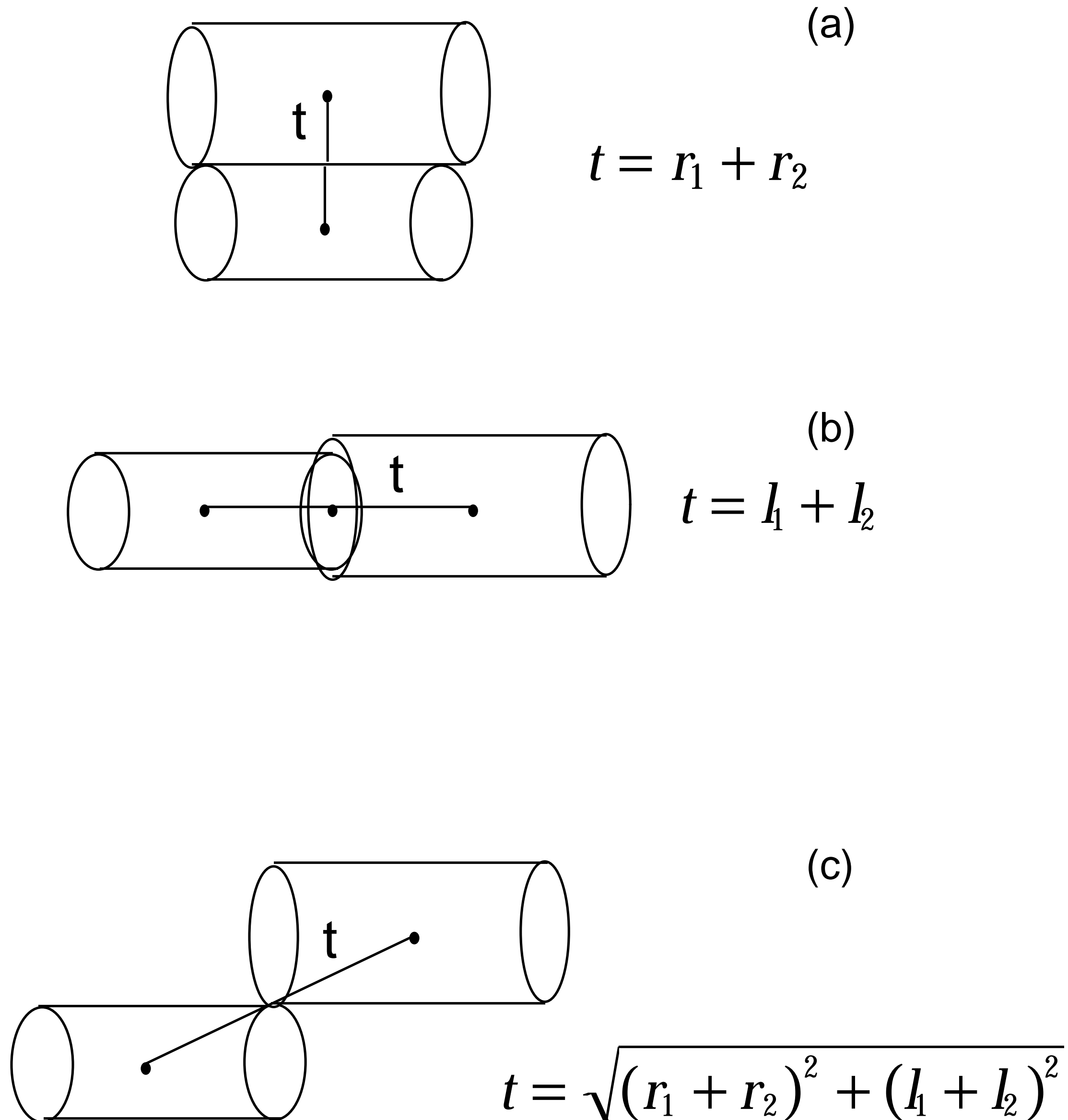

Figure 2.6. Calculation of impact parameter between cylindrically shaped pseudoparticles in the PAM simulation impinging: (a) "side to side" (b) "end to end" and (c) arbitrarily. The impact parameter is computed based on the length and radius of the two interacting cylinders.

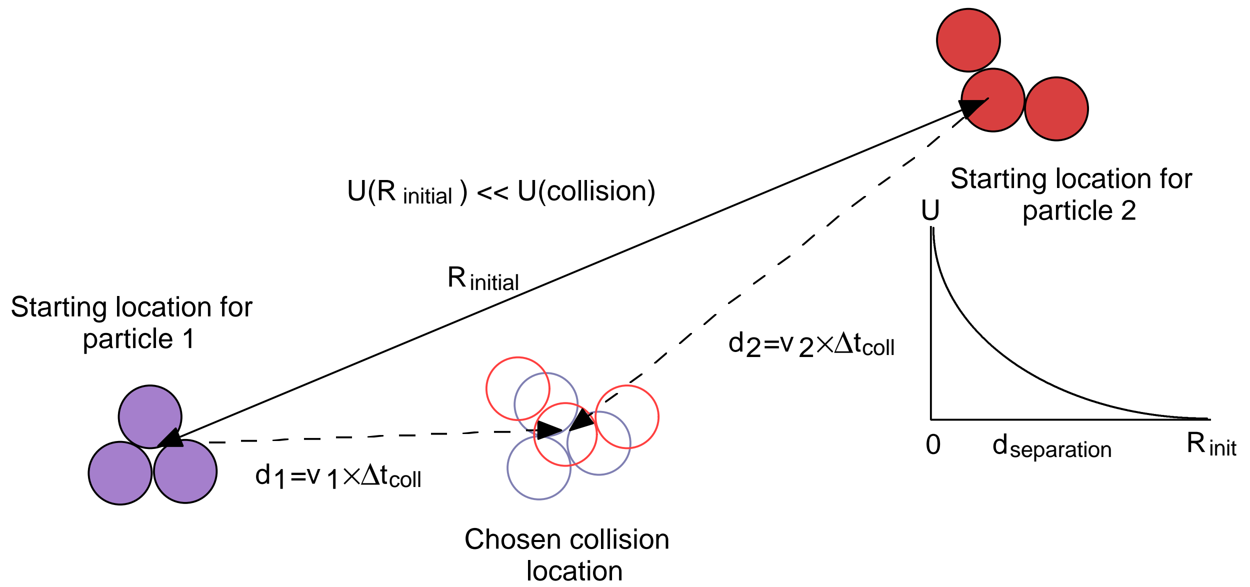

Figure 2.7. Calculation of the initial positions for two approaching particles/clusters in the MD-PAM simulation. Starting locations are chosen such that the initial potential energy is much less than the potential energy at contact.

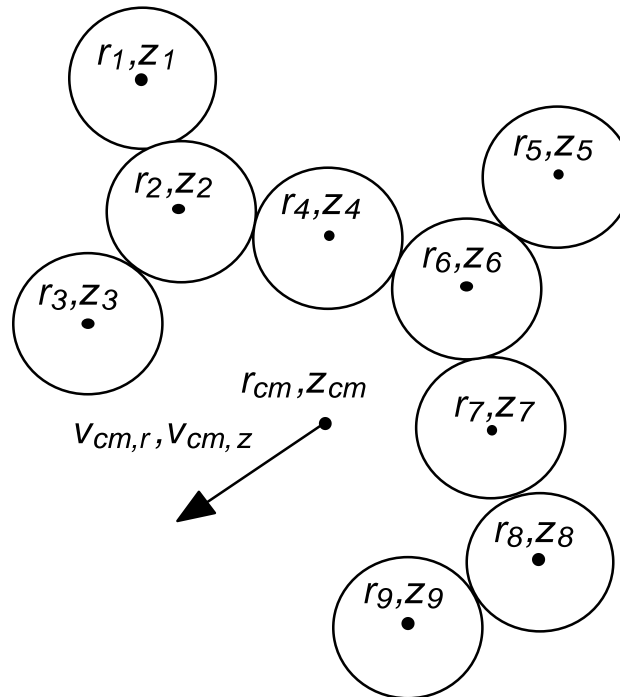

Figure 2.8. Spatial and velocity information retained for each agglomerate in the MD-PAM simulation. All spatial coordinates for each constituent "primary particle" in the cluster are tracked relative to the cluster's center of mass. The particle is assumed to be a rigid body.

2.7 References

[1]P. L. G. Ventzek, R. J. Hoekstra, and M. J. Kushner, J. Vac. Sci. Technol. B **12**, 461 (1994).

[2]S. J. Choi, and M. J. Kushner, IEEE Trans. Plasma Sci. **22**, 138 (1994).

[3]T. J. Sommerer and M. J. Kushner, J. Appl. Phys. **71**, 1654 (1992).

[4]Y. Weng and M. J. Kushner, Phys. Rev. A **42**, 6192 (1990).

[5]M. D. Kilgore, J. E. Daugherty, R. K. Porteous, and D. B. Graves, J. Appl. Phys. **73**, 7195 (1993).

[6]S. J. Choi, P. L. G. Ventzek, R. J. Hoekstra, and M. J. Kushner, Plasma Sources Sci. Technol. **3**, 418 (1994).

3. SIMULATION RESULTS AND ANALYSIS

3.1 Results for Dust Transport Simulation

I have used the Dust Transport Simulation to examine the effects of plasma power, neutral gas flow, and substrate topographical features on the movement and trapping of dust particulates. A schematic of the reactor chosen for these simulations is shown in Figure 3.1. This is a generic, reactive ion etch (RIE) plasma tool, very similar to the one shown in Figure 2.3. The reactor includes a showerhead gas inlet in the grounded electrode at the top of the reactor, while the powered electrode resides at the bottom of the reactor. The exit pump port is an annular region surrounding the bottom electrode. The feed gas for these simulations is Argon at 100 mTorr excited at an RF frequency of 13.56 MHz. The reactor typically operates with 5-120 W of RIE power. Under these operating conditions, the plasma density is on the order of 10^{10} cm^{-3}, with a time-averaged plasma potential of tens of volts. Feedstock gas flows for these simulations are from tens to a few hundred sccm. The reactor is has a 17.8-cm radius and is 5.0 cm in height.

Using this geometry, a series of simulations over a range of RIE power was performed using the DTS. The particular configuration for these cases includes a machined groove in the powered electrode, as well as a dark space shield surrounding the electrode. The time-integrated trajectories of 100 nm-radius dust particulates in the reactor are shown in Figure 3.2(a)-(c) for RIE power levels of 50 W, 200 W and 500 W, respectively. This "fluence contour" plot depicts the time-integrated density of dust particulates throughout the reactor. The brightly colored regions of these plots represent areas of high dust concentration and/or long dust residence times. Immediately we see the presence of dust trapping regions, especially in the low power case. As previously mentioned, these locations are where the electromechanical forces (electrostatic, ion-drag, fluid drag, thermophoretic, and graviational) balance. Significant trapping also occurs near the dark space shield and the machined groove in the substrate. As the RIE power increases to

200 W, particles are trapped in layers closer to the surfaces. Eventually, when the power reaches a sufficient level, the particles are driven through the sheath regions and to the surfaces of the reactor. This is due to the increase in the ion flux, which results in larger ion-drag forces on the particles. These ion-drag forces become the dominant force at higher powers, overcoming the electrostatic forces on the particles and pushing the particles through the sheath region. The electrostatic force, a result of the electric field acting upon the negatively charged dust particle, generally pushes particles away from the reactor surfaces. As these ion-drag forces increase at higher powers, however, the electrostatic fields can no longer keep the particle trapped. The residence time of the particles in the bulk plasma also decreases since the higher ion-drag forces impart more momentum to the particles, increasing their velocities.

Neutral gas flow has proved to be a potentially useful means of controlling contamination in the reactor. Results for three cases with gas flows ranging from 0 to 150 sccm are depicted in Figure 3.3. The plasma is a 100-mTorr Ar discharge operating at 50 W of RF power. Without gas flow, particles are trapped in layers near the reactor surface. With 150 sccm of gas flow, however, the particles are swept away to the outer regions of the reactor, towards the pump port. Trapping no longer occurs in the topographical features of the substrate.

The effects of topographical substrate features on particle transport and trapping are examined over a variety of geometries in Figure 3.4. Once again, a 100-mTorr Ar discharge, operating at 50 W RF power, is simulated. A general reactor, with no distinct substrate features, is shown in Figure 3.4(a). Dust particles are trapped in the conventional layers seen in previous figures. The reactor in Figure 3.4(b) includes an annular groove in the substrate, which creates isolated trapping sites in the dust population. Particles are frequently trapped in regions just above the substrate features. Finally, a silicon wafer is included in the reactor in Figure 3.4(c). This reactor also utilizes a subwafer electrostatic chuck made of dielectric material, but does not include the annular groove. We see that the dust particles are still trapped in layers, but with regions of high dust concentration above the chuck. Both the annular grooves and the subwafer dielectric chuck cause perturbations in the electrostatic fields in the reactor. These perturbations

direct the negatively charged particles towards these additional substrate features and result in a trapping region of higher dust concentrations. With the addition of neutral gas flow, these geometries can be used to prevent dust particles from reaching the surface of the wafer by suspending them above the wafer and entraining the particles into the gas flow to the exhaust port.

3.2 Results for the Particle Agglomeration Model

The Particle Agglomeration Model (PAM) was used to further investigate the agglomeration phenomenon. Using the reactor geometry shown in Figure 3.5(a), the particles were allowed to agglomerate during their transport. Time-fluence contours for primary particles (monomers), as well as agglomerates consisting of three primary particles, are shown in Figure 3.5(b) and (c), respectively. For these cases, the discharge used was a 100 mTorr Argon plasma at 12 W of RIE power. The primary particles used were 1.5 μm in radius, and the agglomerates were forced to be spherical. We see the familiar double trapping layer in the case of primary particles near the sheath edges of the two electrodes. The agglomerate particles are only generated in regions of high dust density, where collision frequencies between the primary particles are high enough to generate the larger clusters. These agglomerates represent only a small fraction (less than one percent) of the total dust particle population.

Fluence contours of the dust particle trajectories using the same discharge but at an RF power of 120 W are shown in Figure 3.6. for agglomerates up to sixth-order in size. As the RF power increases, agglomerates both grow to larger sizes (i.e., they contain more primary particles) and constitute a larger fraction of the total dust population. With increasing RF power, ion-drag forces increase dramatically, accelerating the particles to higher speeds. Second-order agglomerates are much more abundant and take on a spatial distribution similar to the primary particles' population. These agglomerates represent a substantially larger portion (several percent) of the dust particle inventory.

With the additional kinetic energy provided by the larger ion-drag forces, dust particles both collide more frequently and have more energy to overcome the repulsive potential barriers of

their collision partners and agglomerate. Agglomerating particles must have a large *relative* speed, and hence agglomeration typically occurs between fast monomers entering a trapping site and nearly stationary particles already residing in the trapping site. At moderate powers (tens of watts), large agglomerates are typically only found near true trapping sites, while at higher powers (greater than 100 W), large agglomerates can be generated in quasi-traps above the entire substrate surface.

The size of the primary dust particle plays an important role in particle trapping. Larger dust particles are typically trapped closer to surfaces in RIE reactors since they are more sensitive to ion-drag forces. There is a similar dependence for agglomeration. The maximum number of primary particles per agglomerate observed over a range of RF powers and monomer sizes is shown in Figure 3.7(a). For these cases, spherical primary particles were used in the simulation. In general, higher power and larger primary particle sizes produce higher degrees of agglomeration. This dependence on primary particle size results from the fact that repulsive forces scale as $Q^2/R \sim C^2/R \sim R$ in the case of spherical particles, whereas the kinetic energy of the particles scales as $MV^2 \sim R^3V^2$. With increasing particle radius, the kinetic energy of the particle grows more rapidly than the repulsive barrier between colliding particles. The increased sensitivity to ion-drag of larger particles compensates for their lower rates of acceleration due to their larger mass. The end result is agglomeration which favors larger primary particles and higher RF powers, provided that the power is not so large that ion-drag forces push small agglomerates through the sheaths. The fraction of the total particle population that agglomerates represent is shown in Figure 3.7(b). In addition to growing larger at higher powers and primary particle sizes, the relative amount of agglomeration increases as well.

Agglomeration results from particle-particle interactions, and therefore the rates of agglomeration are sensitive to the total monomer particle density. The relative densities of agglomerates are shown in Figure 3.8 as a function of average primary particle density for an RF power of 48 W. Both the number of agglomerates formed and the extent of agglomeration increase with increasing primary particle density. Clearly, for a given power deposition and

reactor geometry, which determine the location of particle trapping sites, there is a density threshold below which no agglomeration occurs.

As mentioned in Chapter 3, Section 3.1, large gas flows from a showerhead or laterally across the wafer in an RIE reactor can be useful in controlling contamination of the substrate. Gas flows of hundreds of sccm can sweep dust particles away from the substrate and electrodes. The effect of gas flow was investigated using the PAM model and similar results for agglomeration were found. For example, fluence contours are shown in Figure 3.9 for 1μm primary particles and fifth-order agglomerates at an RF power of 72 W without gas flow (Figure 3.9(a)) and with 225 sccm of gas (Figure 3.9(b)). Without gas flow, primary particles trap and agglomerates form over the substrate and electrode surfaces. With gas flow, primary particles are swept to the outer regions of the reactor as expected, and agglomerates dominantly form outside the interelectrode gap. The additional kinetic energy imparted to the particles by fluid drag may also contribute to additional agglomeration.

To further investigate the utility of neutral gas flow for controlling contamination, a statistical count was made of particles collected on the surfaces in the reactor, and this distribution is plotted in Figure 3.10. The case shown is for a 72-W, 100-mTorr Argon plasma with no neutral gas flow and 1000-nm-radius primary particles which agglomerate spherically. The brighter portions of the plot represent a larger population of collected particulates. We see that the monomers are driven to the entire surface of both electrodes, in amounts proportional to their concentration just above these surfaces. This implies that the monomers are pushed through the sheaths in trajectories normal to the surface. This is consistent with our contention that they are forced through the sheaths by the positive ion flux, which is normal to the electrodes. The larger agglomerates, shown in Figures 3.10(b) and (c), are also driven to the surface at points very near their generation and/or trapping locations.

Collected agglomerate particles for the same discharge, but with 225 sccm of gas flow, are shown in Figure 3.11. With the additional fluid motion, agglomerates are swept to the outer regions of the reactor as in Figure 3.9, and the surfaces stay contaminant-free.

The shapes of the agglomerates in part define their rates of agglomeration for at least two reasons. First, the capacitance (and hence charge) of the agglomerate depends on the shape of the particle. Second, the orientation (and distance of closest approach) of colliding particles also depends on their respective shapes. Both of these dependencies can be be illustrated by the agglomeration of a spherical primary particle with a long string of already-agglomerated spherical primary particles. For a sufficiently long string (length > λ_D), the approaching primary particle electrostatically "sees" only the charge on one end of the string, thereby reducing the repulsive forces. An illustration of this is given in Figure 3.12. The charge on the long string is also remote from the approaching particle. This effect is much less severe for spherical agglomerates. To illustrate this scaling, the PAM was parameterized for otherwise identical conditions while specifying that the particles be only spherical or allowing them to take on cylindrical shapes. The resulting particle counts are shown in Figure 3.13 for a power deposition of 120 W and primary particles 0.2 μm in radius. Cylindrical particles agglomerate to a greater degree for at least two reasons. First, the cylindrical particles, on average, have a larger distance of separation between the charge centers. Secondly, the cylindrical particles have a smaller capacitance and thus a lower amount of charge on them. The combination of these two effects creates a lower average electrostatic potential to overcome between the colliding particles, and results in a significantly higher degree of agglomeration for the cylindrical particles. Agglomerates in excess of fifteen primary particles are generated.

The aspect ratio of the cylindrical particles may perhaps provide some insight to the agglomeration phenomenon. The aspect ratio is defined as $\Gamma=(R/L)$, where R is the particle's radius and L is the length of the cylinder. Therefore, Γ ranges from zero to infinity, the former representing an infinitely long, thin rod shape while the later represents an infinitely large, flat disk. The threshold value of $\Gamma=1$, where the radius and length are equal, corresponds roughly to a spherically shaped particle.

The aspect ratio of the particles generated in the PAM simulation for the case of Figure 3.13 is plotted in Figure 3.14 for agglomerates of sizes three through fifteen. We see that all

species grow somewhat preferentially into the longer cylindrical shapes, especially the larger (N>8) structures. This implies that under these discharge conditions, the primary particles attain relative velocities which are sufficient for growing agglomerates with lower fractal dimensions only. The average speeds of the primary particles are not large enough to produce agglomerates with higher aspect ratios. For 200-nm radius primary particles, with a linearized Debye length of approximately 18 μm in the discharge used for the results of Figure 3.14, the capacitance of a spherically shaped primary particle is 2.25×10^{-17} F. This value is computed using Equation 2.22. For a cylindrically shaped particle consisting of three primary particles chained together, the capacitance from Equation (2.23) is approximately 1.49×10^{-17} F. In a region where the electron temperature is constant, the charge on the spherical primary particle would be approximately 50% higher than that of a third-order cylindrical agglomerate. From this simple comparison, we see that the electrostatic potential barrier between two particles is highly dependent on the particle shapes, and that smaller aspect ratios produce conditions more favorable to agglomeration. The results of this are clearly seen in Figure 3.14, where the majority of the agglomerates have aspect ratios of less than 1.

3.3 Results for the Molecular Dynamics PAM Model

Using the MD-PAM model, the morphology of particles under various operating conditions was further investigated. In Figure 3.15(a), an SEM micrograph of a dust particle collected in a 200 mTorr, SF_6 RIE discharge is pictured. The primary particles in this cluster are approximately 40 nm in diameter. In Figure 3.15(b), a typical agglomerate generated by the MD-PAM model under similar conditions, using the same size primary particles made of silicon, is presented. Both the experimental and simulated particles exhibit a low fractal dimension, filamentary shape.

As previously mentioned, dust particulates require a sufficient velocity to overcome the electrostatic potential barrier between them and agglomerate. This potential barrier is highly dependent on the morphology of the particles, since the morphology determines the distance of closest approach between charge centers for two colliding particles. Long, filamentary clusters, on

average, present a lower repulsive charge to an incoming particle if it is more than a linearized Debye length in dimension. Tightly packed clusters, such as the “cauliflower shaped” particles observed by Garscadden et al.,[1] present a higher effective charge for the same number of constituent primary particles, since more of the primary particles, on average, are in a linearized Debye length of an approaching particle. Thus, the required relative velocity to produce agglomeration will, on average, be smaller for the first collision pair.

To determine the effects of approach velocity on morphology, the MD-PAM was run using a range of specified, constant particle velocities. The simulations were each begun with two 1-μm-radius silicon primary particles colliding at the specified approach velocity. If they agglomerated, another single primary particle was introduced to the system, again at the specified velocity. This process was repeated until the agglomerate cluster reached a specified size or the simulation reached a specified number of trials. The electric charge residing on each of the primary particles was calculated to be -2277 q. The particles generated by approach velocities ranging from 50 cm/s to 300 cm/s are depicted in Figure 3.16(a)-(d). At the lower velocities, the clusters formed are long and filamentary, similar to the particle shown in Figure 3.15. As the approach velocity increases to 100 cm/s or higher, the particles have sufficient kinetic energy to form higher fractal, cauliflower-like shapes.

The primary particle size is expected to once again have a large effect on the amount and extent of agglomeration, due to the increased kinetic energy at larger primary particle radii. The MD-PAM simulation was executed under a parameter space of approach speeds ranging from 10 to 1000 cm/s, and for primary particles ranging from 100 to 1000 nm in radius. The maximum number of allowed primary particles per agglomerate was set at 150, after which the simulation was ended. Our experience is that agglomerates reaching this size will continue to grow. The maximum agglomerate size attained is plotted in Figure 3.17 for these cases. We see that as the primary particle size increases, the amount of agglomeration at a given velocity increases. The increased mass of the larger particles gives them more kinetic energy and overcompensates for their increased surface charge, allowing for growth to larger sizes. Also, for each primary particle

size, there is a cutoff velocity below which no agglomeration occurs. For particles 100 nm in radius, the minimum required approach speed is approximately 200 cm/s, while for particles 1000 nm in radius, the required speed is only 40 cm/s.

The morphology depends directly upon the ratio of the kinetic energy of the particles to the potential energy of the collision pair. The kinetic of a particle is given simply by

$$KE = \tfrac{1}{2} m v^2 \propto R^3 v^2 \tag{3.1}$$

Here, m is the mass of the particle, R is the particle radius, and v is the particle's translational velocity. The repulsive potential energy between the two particles is given by

$$U = \frac{Q_1 Q_2}{4\boldsymbol{pe}\left(R_1 + R_2\right)} \propto \frac{R_1 R_2 T_e^2}{R_1 + R_2} \tag{3.2}$$

where Q_1 and Q_2 represent the total surface charge on the particles, and T_e is the electron temperature in the surrounding plasma.

The parameter ***b*** is defined as

$$\boldsymbol{b} = \frac{KE}{U} \propto \frac{R^2 v^2}{T_e^2} \tag{3.3}$$

which has the units of $cm^4/eV^2\text{-}s^2$, upon which the morphology is dependent. A higher approach velocity increases the value of ***b***, and so a high ***b*** value is expected to produce compact, high fractal dimension agglomerates. To test the validity of ***b*** as a scaling parameter, agglomerates were generated using different sized primary particles and approach velocities that resulted in the same value of ***b***. The results of the simulations are pictured in Figure 3.18. All three agglomerates have low fractal dimensions and are similarly shaped.

A series of simulations using the MD-PAM was then performed with plasma parameters and velocity distributions taken from a generic RIE reactor. A schematic of this reactor is shown in Figure 3.19. This reactor is similar to the reactor used in Chapter 3, Section 3.1, but includes a

larger interelectrode gap. Once again, a metal dark space shield surrounding the powered electrode is included, and a showerhead gas inlet nozzle is built into the grounded electrode at the top of the reactor. The HPEM simulation was first used to calculate plasma parameters for this reactor, and susbsequently ran the DTS simulation to model the dust transport and trapping. Velocity distributions were then generated in the DTS throughout the entire reactor.

The plasma potential, electron density, and electron temperature are shown in Figure 3.20(a)-(c) for a 100-mTorr Ar discharge operating at 21 W of RF power. The powered electrode was driven with an RF amplitude voltage of 60V. An operating power of roughly 20 W was chosen because commercial etching processes are often performed at powers of tens of watts. The value of 21 W was the power deposition converged upon by the HPEM model at the specified bias voltage. The time-averaged plasma potential ranges from -26.5 V on the powered electrode to 21.8 V in the bulk plasma. The electron and ion densities are on the order of 10^8-10^9 cm^{-3}, while the electron temperature ranges from roughly 1.5 eV in the sheath regions to 4 eV in the bulk plasma.

Time-fluence contours for silicon primary particles 200 nm in radius are plotted in Figure 3.21. The particles were initially released uniformly in the region between the two electrodes. Notice that particles are suspended in two distinct layers originating near the center of the inter-electrode gap. Particles travel along these layers, towards the center of the discharge at $r=0$, where they are trapped near the sheath regions. The particles move towards the center of the discharge as a result of electrostatic forces; the negatively charged particles are attracted to the plasma potential peak. The contaminants are forced to the sheath regions by the ion-drag forces, which increase near the surfaces of the electrodes.

The same reactor and primary particles were used in a series of cases varied over deposition power. The time fluence contours for the primary particles are once again plotted in Figure 3.22(a)-(e). These discharges were simulated at 2 W, 11 W, 21 W, 53 W and 106 W of RF power, respectively. We see that at low powers, particles are trapped near the center of the discharge where the electrostatic forces dominate. As the power increases to 21 W in Figure

3.22(c), the dust particulates are driven towards the electrode surfaces in two distinct layers. As the power increases further to 53 and 106 W in Figure 3.22(d) and (e), respectively, these trapping layers become more pronounced and begin to extend toward the outer regions of the chamber. At higher power levels, the ion-drag forces in the reactor begin to dominate, pushing the particles toward the reactor surfaces. The isolated trapping sites in the fluence layers in Figure 3.22 (d) and (e) are most likely statistical artifacts. The electric fields and ion fluxes do not vary greatly over these regions; using more pseudoparticles in the simulation would produce more evenly distributed density plots. To optimize execution time of the code, an upper limit of 30,000 pseudoparticles was set for the cases presented.

Results from the PAM simulation indicate that dust particles agglomerate either in or en route to the trapping site. A typical plot of these results is shown in Figure 3.23 for a 100-mTorr Ar discharge at 21 W of power, using primary particles 1000 nm in radius which agglomerate cylindrically. The dust populations for primary particles, second-order agglomerates, and third-order agglomerates are illustrated in Figure 3.23(a)-(c) respectively. We see the familiar trapping layers for primary particles in Figure 3.23(a). The second-order agglomerates in Figure 3.23(b) are grown in the trapping layers in regions of high dust concentration. This is true of the third-order agglomerates as well, although in a more isolated region. This implies that the majority of agglomerates are formed one primary particle at a time, and usually between a slow moving large particle residing in a trap, and a faster approaching primary particle.

Velocity distributions of primary particles were then taken throughout the reactor. In particular, the velocity distributions of dust particles in and near the trapping layer near the top electrode were generated for the cases in Figure 3.22(a)-(e). These velocities were then used in the MD-PAM simulation to determine the extent of agglomerate formation and their resulting morphology. Three typical velocity distributions are plotted in Figure 3.24(a) for the 21.17-W, 53-W and 106-W cases. We see that the maximum speed attained by particles in this region of the reactor is approximately 1000 cm/s at the lower powers, and nearly 1200 cm/s at the higher powers. The majority of the population, however, reside in the very low (0-100 cm/s) speed

ranges. This portion of the distribution represents the particles that have either slowed down or virtually stopped in the trapping site. An expanded plot of the low-velocity (0-100 cm/s) portion of the distributions appears in Figure 3.24(b). We see that the lower powers have a relatively larger population at these low velocities. The high velocity tail of the distribution represents particles that are being driven into the trap from the adjacent spatial cells. Agglomeration occurs mainly between representative particles from both ends of the velocity distribution.

The agglomerates formed using the MD-PAM simulation and the speed distributions generated by the DTS are depicted in Figure 3.25. Once again, the cases range in RIE power from 2 W to 106 W. We see that at low powers, the agglomerates formed are long, dendritic structures, as expected. With the lower average speeds at the low powers, the primary particles require a large amount of charge shielding from each other in order to overcome the repulsive potential barrier. As the RF power increases, the higher attained velocities allow the agglomeration to be more ballistic in nature, and we see that the agglomerate begins to take on a more compact shape. The agglomerates grown at higher powers also have a greater number of consituent primary particles. With a higher average energy, more primary particles on average are able to overcome the electrostatic potential and deposit themselves on the agglomerate. Note that the center portion of the agglomerate in Figure 3.25(c) is “cauliflower-like” while the ends are more filamentary. This implies that the primary particles deposited ballistically on the structure at first, until the collective surface charge reached some threshold. At this point, particles were no longer able to overcome the electrostatic barrier of the agglomerate, and the dominant growth mechanism changed to diffusive growth, forming the longer, chain-like structures on the two ends of the agglomerate.

To examine the statistical nature of these agglomerate morphologies, a large sample of relatively small agglomerates was generated using the discharge conditions of Figure 3.20. The velocity distribution used to grow these agglomerates is the same as that used in Figure 3.25(a). Once again, 200-nm-radius primary particles were used. A collection of agglomerates ranging from three to ten primary particles in size was produced, with forty particles grown for each size.

Some typical morphologies for fourth-order and tenth-order agglomerates are shown in Figures 3.26 and 3.27, respectively. We see in Figure 3.26 that fourth-order agglomerates can be formed in either colinear structures or compact clusters using this velocity distribution. At this relatively small size, the average β values of the primary particles is high enough to generate both morphologies. In general, the compact structure is found to be more common with this velocity distribution. Only a few particles in the entire sample size were colinearly shaped. These compact structures cannot be sustained as the particles grow larger, however. As the size of the particle grows to tenth order in Figure 3.27, we see that the low fractal dimension morphology becomes the dominant shape in the particle inventory. The average β value for these particles, using this velocity distribution, is not high enough to generate compact clusters as the electrostatic charge barrier increases with higher-order agglomerates.

As previously mentioned, the size of the primary particle used in the MD-PAM simulation has a dramatic effect on the amount of agglomeration. The mass, and hence the kinetic energy, of a primary particle is proportional to the cube of the primary particle's radius. Thus, using larger primary particles, it is easier to overcome the potential barriers between them. The surface charge on each primary particle, calculated using the algorithm described in Chapter 2, is plotted for primary particles ranging from 50 nm to 1000 nm in radius in Figure 3.28. We see that the surface charge does indeed scale very nearly linearly with particle radius under these plasma conditions. Thus, the potential barrier between two unshielded primary particles of the same size scales with $Q^2 \sim R^2$. The kinetic energy of the system, however, increases with R^3, and so agglomerate growth is expected to become more ballistic at the larger particle radii since the ***b*** value increases.

A series of DTS simulations were performed using primary particles ranging from 50 nm in radius to 1000 nm in radius. The time-fluence contours for these spherical primary particles is pictured in Figure 3.29. The radii for the plots in Figure 3.29(a)-(e) are 50 nm, 200 nm, 500 nm, 750 nm, and 1000 nm, respectively. We see that with smaller primary particles, electrostatic forces dominate and the particles are suspended in the center of the discharge. As the primary particle size increases, however, the ion forces increase proportionally, forcing the particles

towards the electrode surfaces in two distinct layers. This effect continues to grow as the particles reach the micron range. Finally, with 1000-nm-radius particles, the ion flux begins to drive some of the particles outward in the reactor.

The particle velocity distributions in the trapping regions of the reactor for the cases of Figure 3.28 are plotted in Figure 3.30. These normalized distributions were taken in the spatial region immediately surrounding the trapping layers shown in Figure 3.29(a)-(e). For the cases where there are two trapping layers, the region near the grounded (top) electrode was selected for these purposes. As the particle size increases, the maximum velocity attained decreases, as expected. The larger, heavier primary particles simply cannot accelerate as quickly, and do not reach very high speeds. We see that the smaller particles, those 50 nm and 100 nm in radius, can reach very high speeds.

The maximum velocity attained for each size primary particle is depicted in Figure 3.31. The 50-nm and 100-nm primary particles each reach the maximum allowed velocity of 1500 cm/s. For particles larger than 100 nm in radius, the maximum velocity roughly follows an inverse square dependency on the particle radius. The energy of a particle moving at this velocity, however, also depends on the mass of the particle, which is proportional to R^3. This would imply that for two different sized particles, each moving at its maximum velocity, the larger particle would still have a higher level of kinetic energy.

To examine this more closely, the kinetic energy distribution, defined in Equation (3.1), is plotted Figure 3.32 for primary particles 200 nm, 300 nm, and 1000 nm in radius. These kinetic energies were recorded directly from the DTS simulation; they are not calculated based on the velocity distributions in Figure 3.30. We see that although the average velocity of the larger particles is lower, their average kinetic energy is still much higher than that of smaller particles. The maximum energy bin for these distributions was set at 1×10^{-7} ergs. While the energy distributions for 200-nm and 300-nm radius particles cuts off at 4.25×10^{-8} and 6.25×10^{-8} ergs respectively, the cutoff energy for particles 1000 nm in radius is much higher. All three distributions exhibit a large population of primary particles near zero energy. Once again, these

particles represent the particles that are nearly motionless as they are suspended in the trapping site.

The energy distributions for 300-nm particles, taken from the trapping site and over the entire reactor mesh, are depicted in Figure 3.33. We see that the primary particles are able to attain much higher kinetic energies in other regions of the reactor. The cutoff energy in the reactor distribution is much higher than in the trapping location. The particles in the reactor distribution's high energy tail are probably those that are accelerated through the sheath region to the reactor surfaces. Since the positive ions reach their highest velocities (and thus energies) in the sheaths, this region is where dust particles are likely to be accelerated to their highest velocities as well.

The agglomerates generated by the MD-PAM using primary particles 100 nm to 1000 nm in radius are pictured in Figure 3.34 (a)-(e), respectively. These particles were constructed using the velocity distributions of Figure 3.30, generated by the DTS. The 100-mTorr, 21-W discharge was used for these simulations. At 100 nm, very few primary particles were able to agglomerate, and only a small chain was formed. Contrarily, by using 200-nm particles that are eight times as heavy in Figure 3.34(b), a large, filamentary agglomerate could be formed in the allotted number of trials (30,000). At the larger radii of 500 nm, 750 nm and 1000 nm, only large, compact agglomerates are formed. In the intermediate primary particle sizes of 300 nm and 400 nm in Figure 3.34 (c) and (d), the growth pattern seems to be a combination of diffusive and ballistic mechanisms. Similar to the results in Figure 3.25(c), we see agglomerates that have a closely packed center region, with a few scattered filamentary chains extending from it. This is more pronounced at 300 nm than at 400 nm. Once again, this suggests that the particles have enough mass that there is sufficient kinetic energy to grow ballistically for a while, until the concentrated charge center proves to be too large of an electrostatic barrier. After this point, the agglomerate grows diffusively.

Finally, the effect of neutral gas flow on the transport and velocity of the particles in the reactor was further investigated. Time-fluence contours for a 100-mTorr, 21-W Ar discharge using 200-nm-radius particles at gas flows ranging from 10 to 500 sccm are plotted in Figure 3.35.

The gas flows for Figure 3.35(a)-(e) are 10 sccm, 50 sccm, 100 sccm, 250 sccm, and 500 sccm, respectively. Comparing the plots of 3.35(a)-(b) with the same case with no gas flow in Figure 3.21, we see that low flow rates of 10-50 sccm have little effect on dust transport. As the gas flow increases to 100 sccm, however, we see that a significant portion of the dust population is pushed outward in the reactor, forming a single trapping location outside the interelectrode gap. As the gas flow further increases to hundreds of sccm, the particles are pushed outward even further, to the point where they are suspended in layers above the surfaces of the outer regions of the reactor.

The normalized total reactor velocity distributions for the cases in Figure 3.35 (a)-(d) are plotted in Figure 3.36. Flow rates of less than 100 sccm produce no significant changes to the velocity distribution. At 250 sccm, however, there is a noticeable increase in the average velocity of the particles, particularly at velocities below 1000 cm/s. One would expect that the amount of agglomeration would increase as well with the increased velocity, but this would likely occur away from the wafer region of the reactor.

The time fluence contours for three cases–all implementing 250 sccm of gas flow but with primary particle radii of 50 nm, 200 nm, and 500 nm–are shown in Figure 3.37(a)-(c), respectively. The RF power in these simulations was held at 21 W. With the smaller particles of Figure 3.37(a), the flow rate is sufficient to drive the particles outward in the reactor, while the electrostatic forces prevent them from reaching the surface of the electrodes. Note that the particles now reside in two distinct layers, whereas they were in a single layer without the gas flow in Figure 3.29(a). Apparently, the addition of the gas flow exerts some additional force upon the particles which is sufficient to drive them away from the center of the discharge. At 200 nm, the particles are heavy enough that they are not driven as far outward in the reactor as 50-nm particles. Interestingly, at even larger radii in Figure 3.37(c), the primary particles are once again forced outwards. This is perhaps due to the fact that the ion-drag forces are much higher at these larger radii, and so it may be the positive ion flux in the reactor which pushes the particles toward the outer walls. Also in this case, there is a much larger dust population near the bottom of the reactor than at the top. This perhaps implies that at the larger radii, gravitational forces come into play and can overwhelm the

smaller electrostatic forces in this region of the discharge, allowing the particles to "fall" toward the bottom of the reactor.

Finally, the reactor velocity distributions for the three cases of Figure 3.37 are plotted in Figure 3.38. When comparing the maximum velocities of these distributions with the values using no gas flow in Figure 3.31, we see that the addition of neutral gas flow does not cause a significant increase. However, the flow rate is able to cause a large perturbation in the spatial distribution of the particles. This is probably due to the fact that the neutral gas flows in a direction that is often perpendicular to the electrostatic and ion-drag force vectors, especially near the electrodes. As the particles become trapped in layers, then, a small "nudge" by the neutral gas in a direction normal to these vectors is enough to drive the particles toward the outer regions of the reactor. It is possible, then, to sweep contaminants away from the wafers with moderate amounts of gas flow.

3.4 Figures

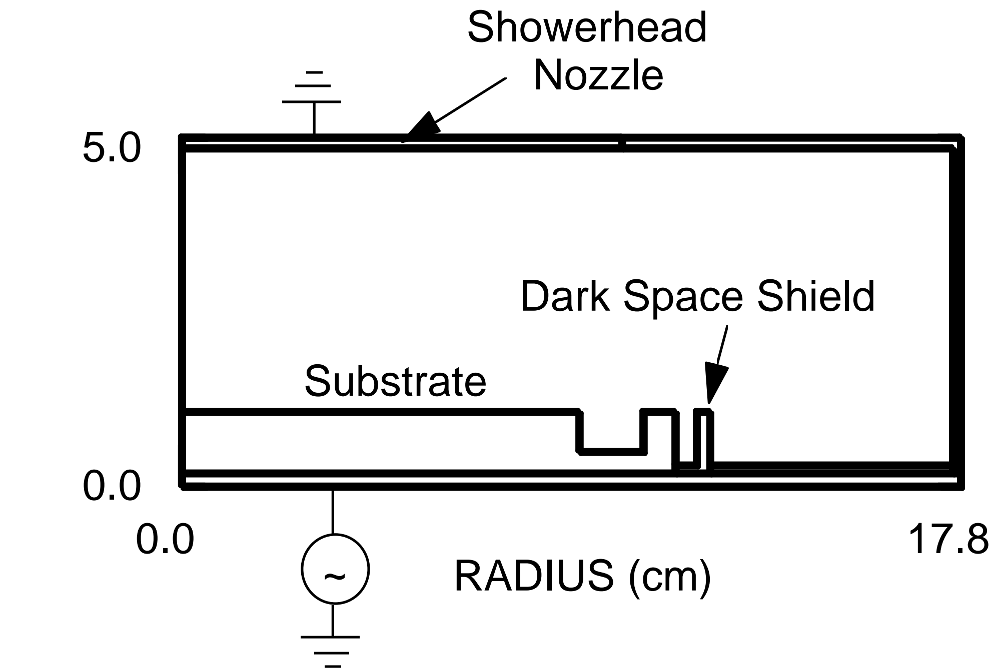

Figure 3.1. Schematic of the reactor used for the results of Chapter 3, Section 3.1. The reactor includes a showerhead gas inlet at the top of the chamber, and a dark space shield surrounding the powered electrode at the bottom of the chamber.

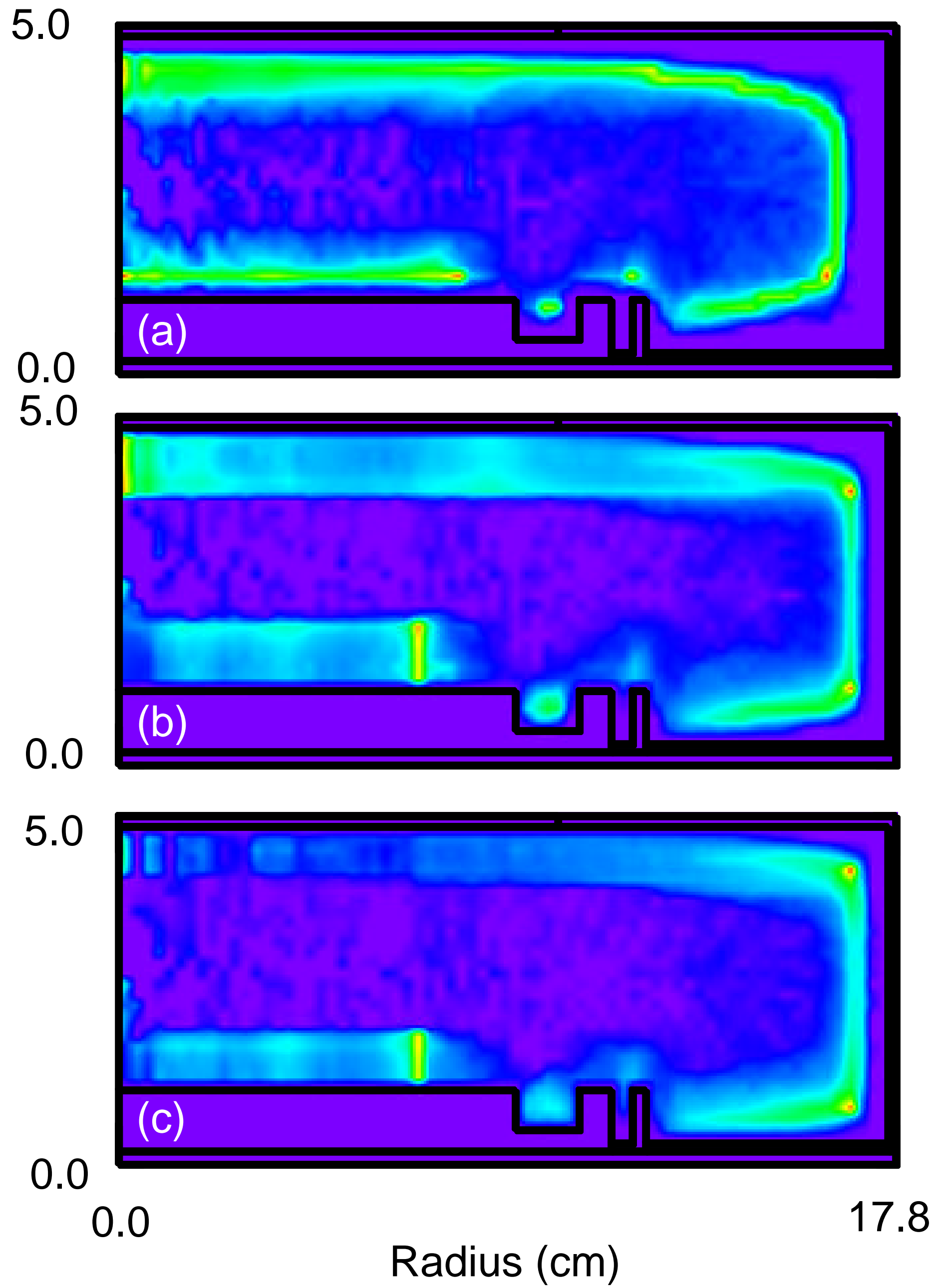

Figure 3.2. Time fluence contours for primary particles 100 nm in radius in the RIE reactor of Figure 3.1. The discharge is a 100 mTorr Argon plasma operating at (a) 50 W, (b) 200 W, and (c) 500 W of RF power.

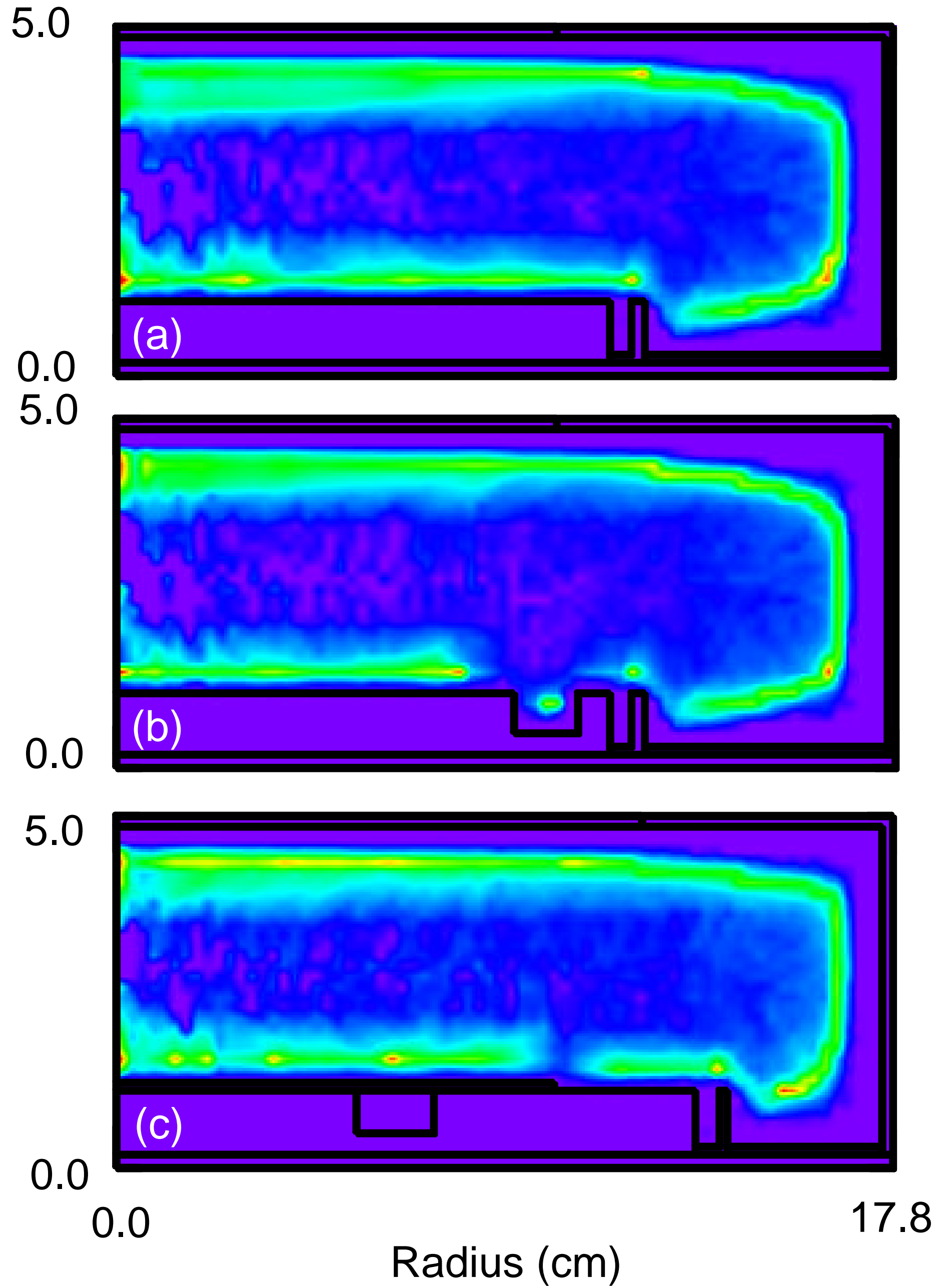

Figure 3.3 Time fluence contours for 100 nm primary particles in a 100 mTorr Ar discharge operating at 50 W of power in a reactor having (a) no substrate features, (b) having a machined groove in the powered electrode, and (c) having a subwafer dielectric ring. The groove and dielectric ring in (b) and (c) alter the electric fields, leading to small potential wells over these features which trap particles.

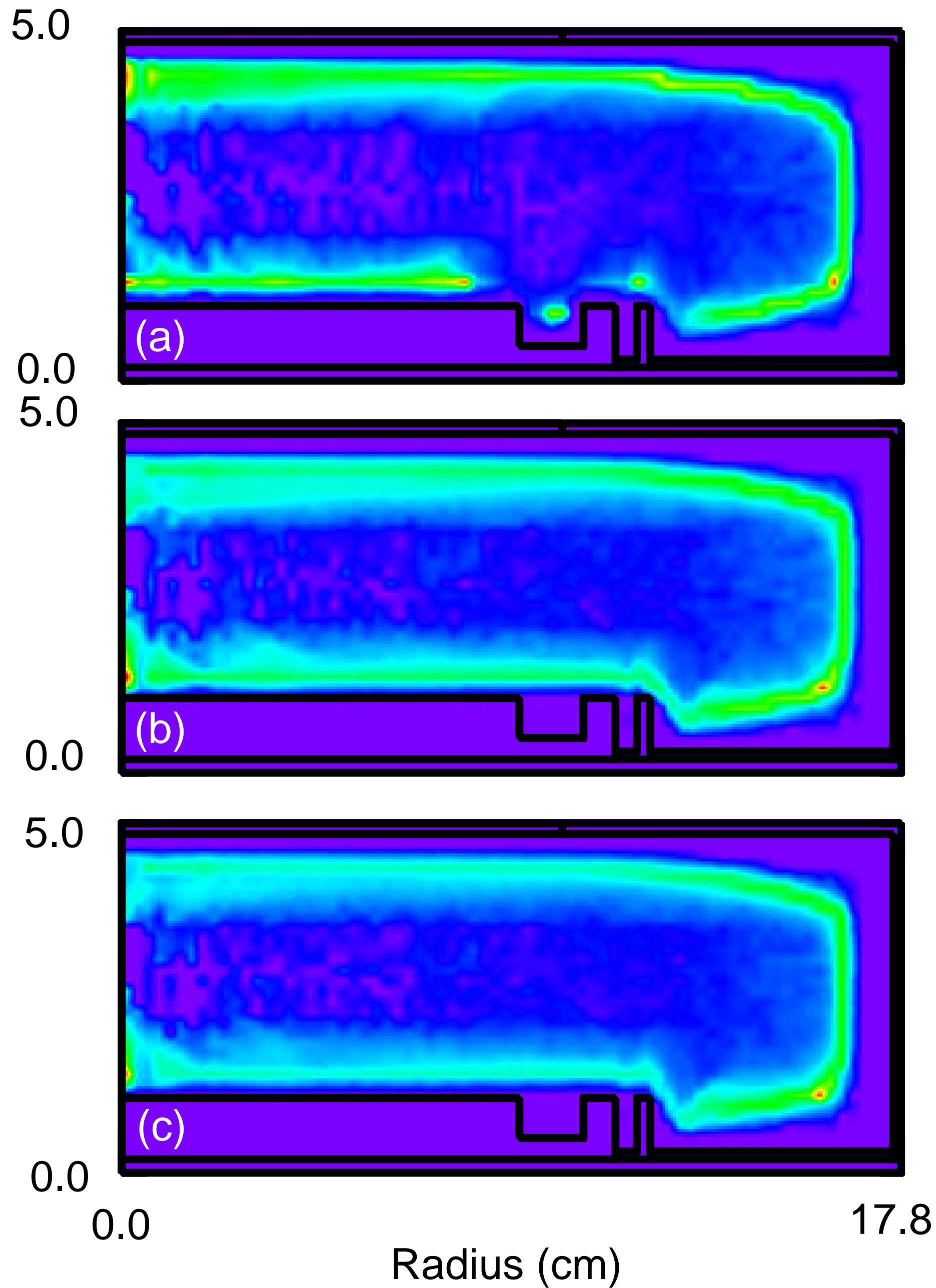

Figure 3.4. Time fluence contours for 100 nm radius primary particles in a 100 mTorr Ar discharge operating at 50 W of power and having feedstock gas flow rates of (a) 0 sccm, (b) 75 sccm, and (c) 150 sccm. Particles residing in the powered substrate groove at 0 sccm are no longer trapped there at 75 and 150 sccm.

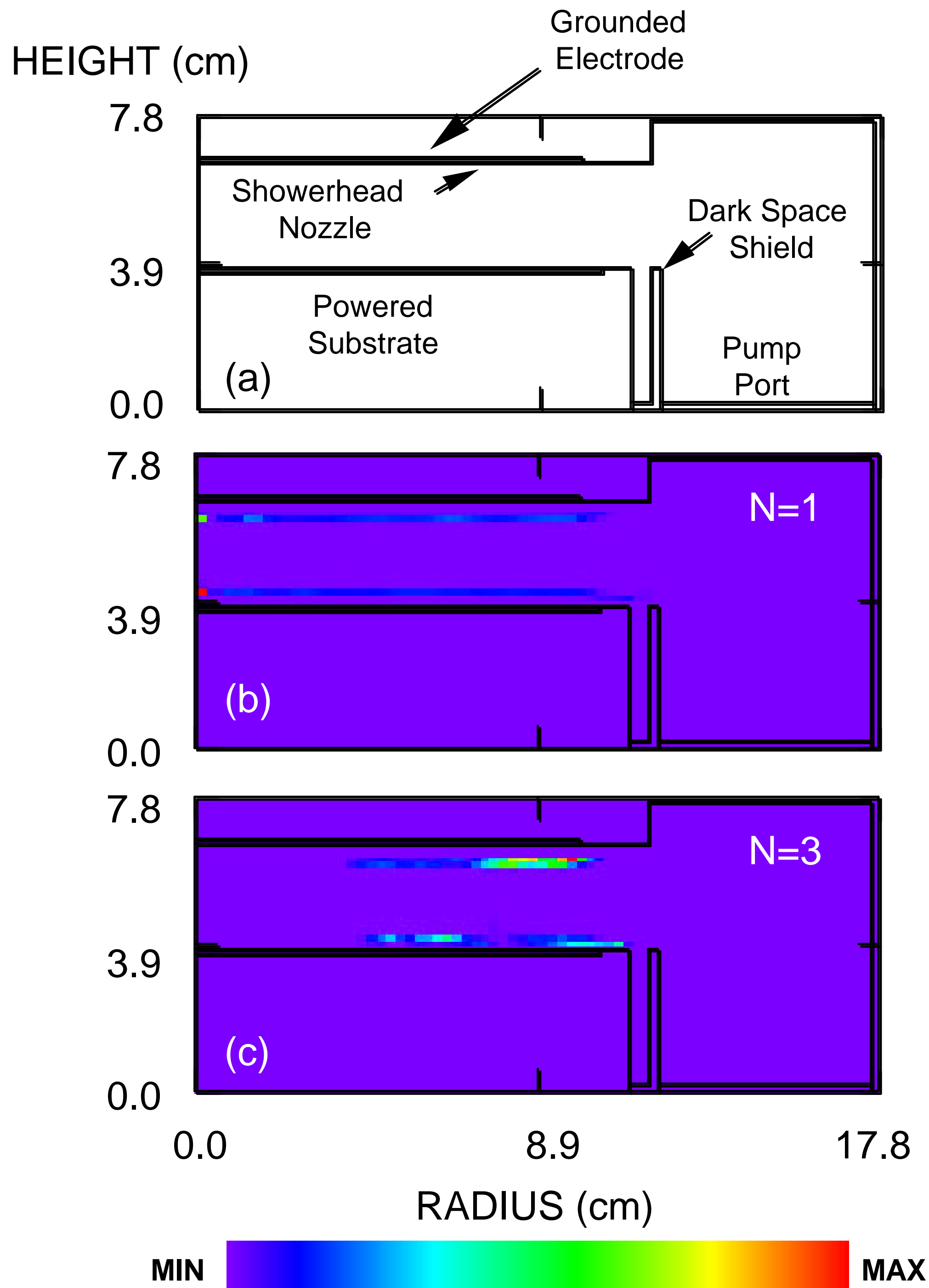

Figure 3.5. Schematic diagram (a) of the RIE reactor geometry modeled in Section III.B, and time fluence contours for (b) primary particles and (c) third-order agglomerates in a 100 mTorr, 12 W Ar discharge. Primary particles were spherically shaped, and 200 nm in radius.

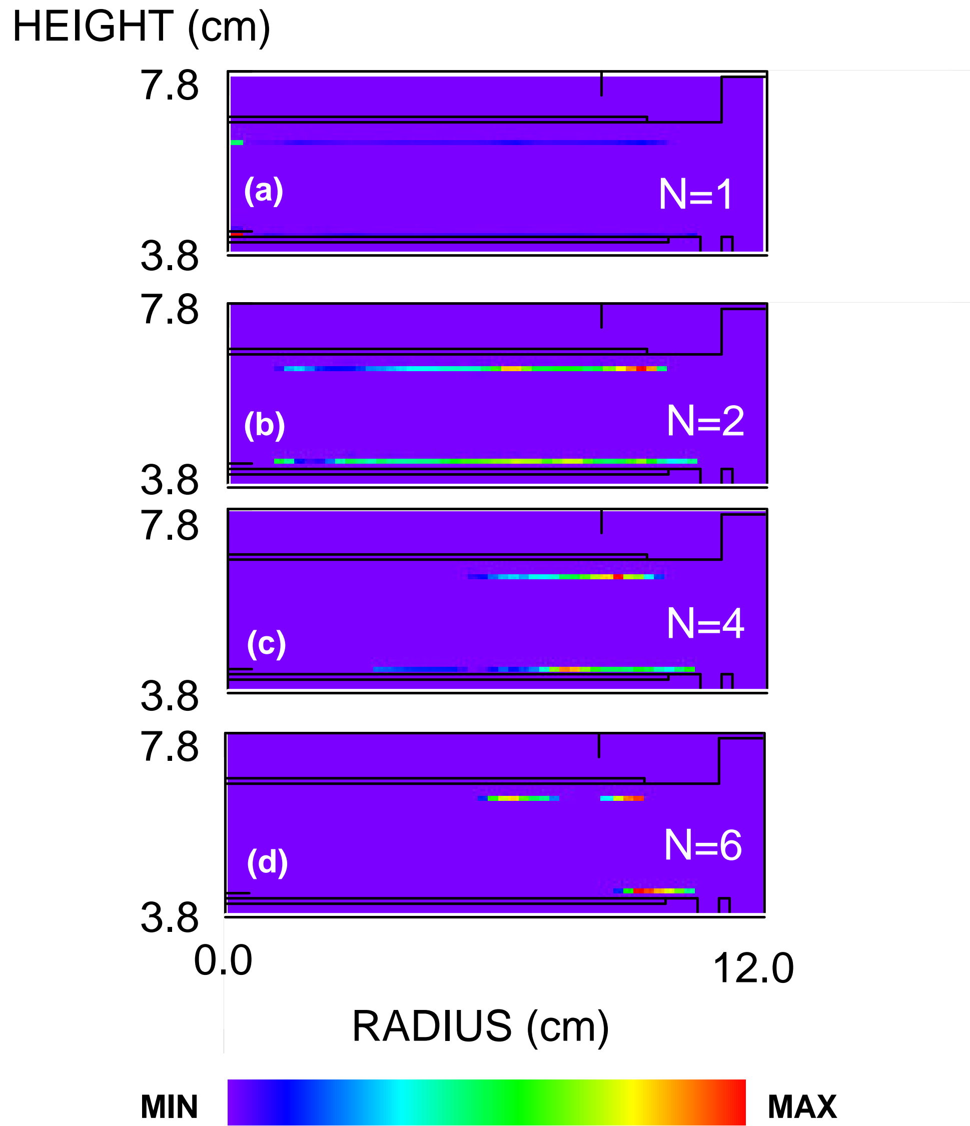

Figure 3.6. Time fluence contours for (a) primary particles, (b) second-order, (c) fourth-order, and (d) sixth-order agglomerates generated in a 100 mTorr 120 W Argon discharge. The primary particles reside in well spread, uniform layers, while the larger agglomerates form in more isolated regions in the trapping layers.

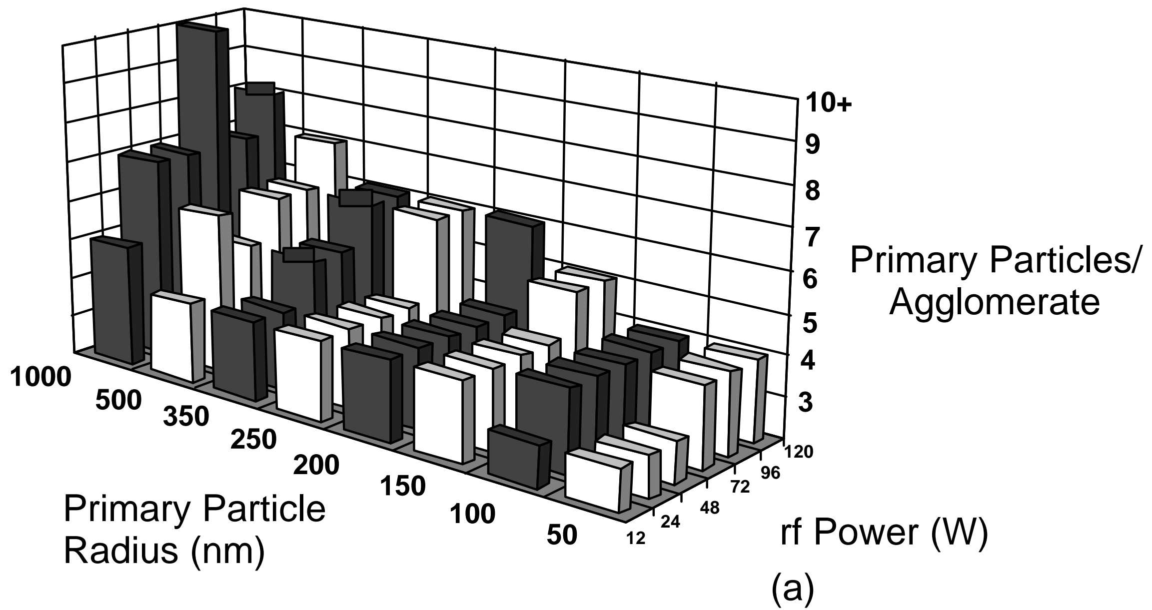

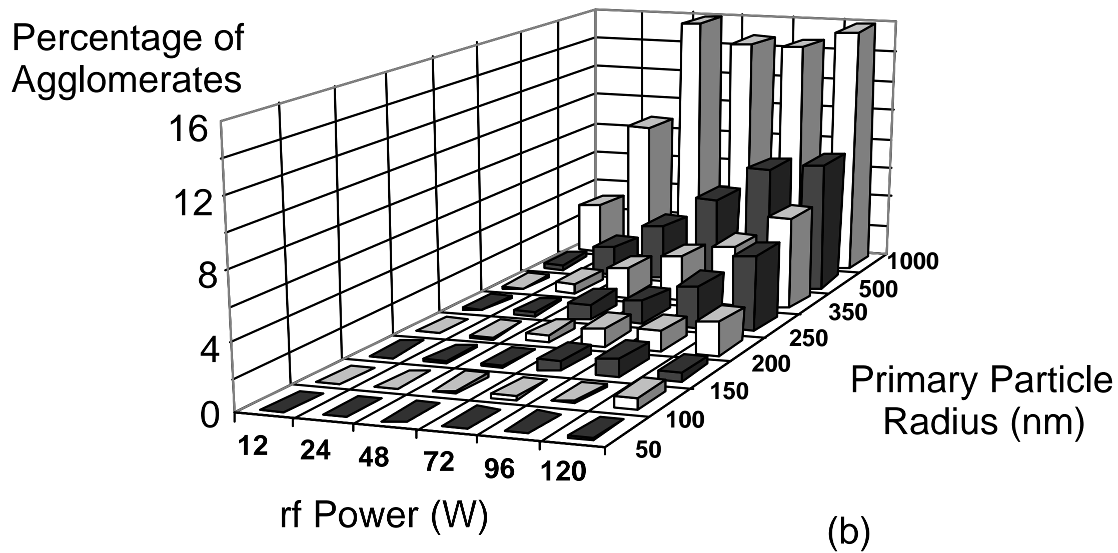

Figure 3.7. (a) Maximum size attained by agglomerates (in primary particles/agglomerate) and (b) fraction of the total dust population which are agglomerates for powers ranging from 12 to 120 W,

and primary particle radii from 50 to 1000 nm. As the primary particle and RF power increase, the amount and extent of agglomeration both increase as well.

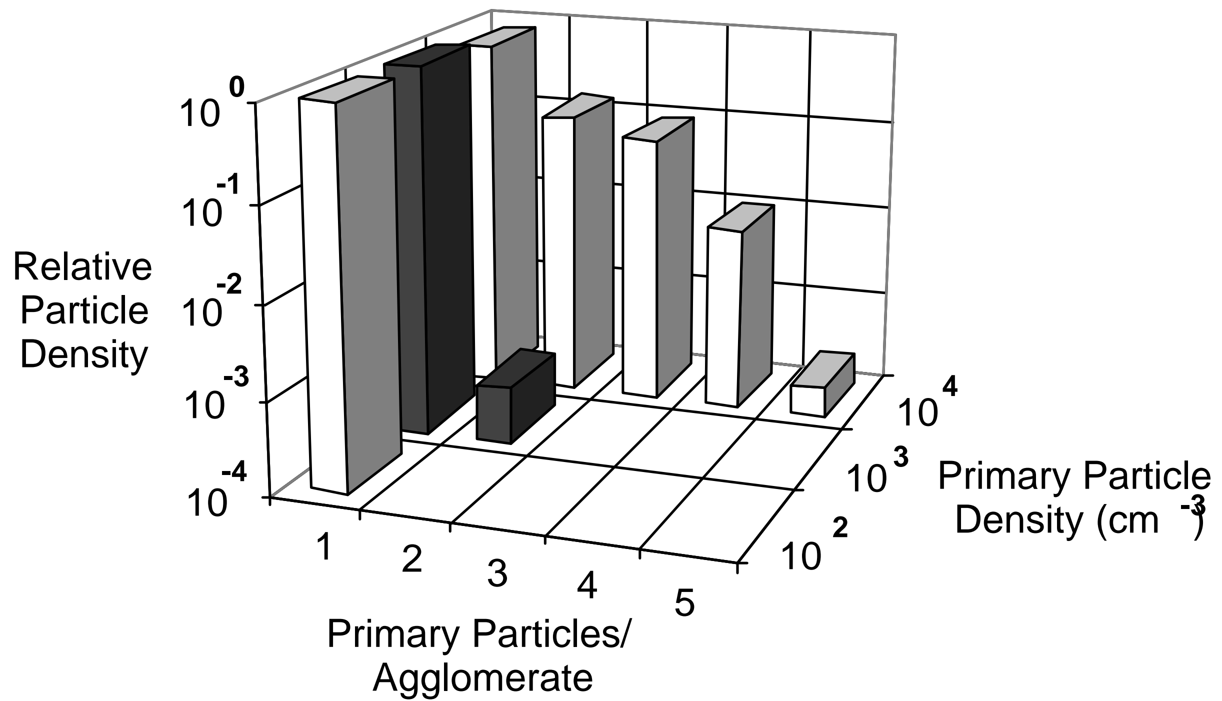

Figure 3.8. Relative particle population for primary particles and agglomerates vs. primary particle density. Below a density of 10^4 cm^{-3}, no agglomeration occurs.

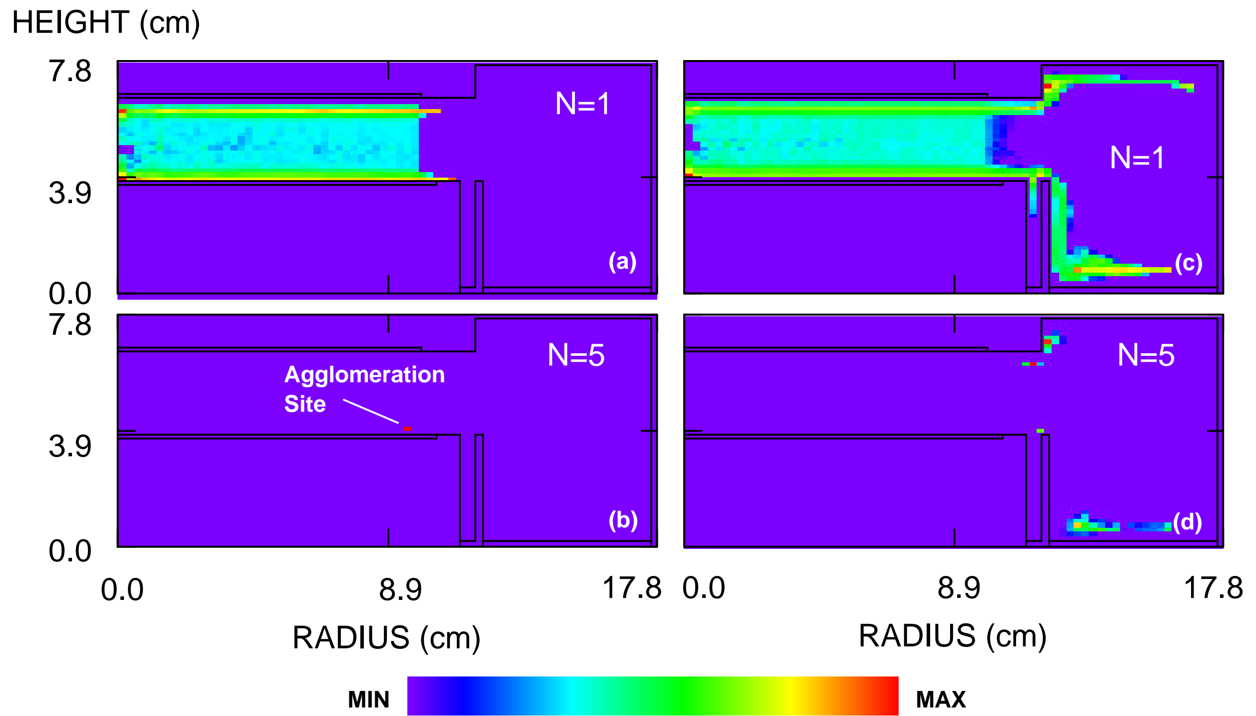

Figure 3.9. Time fluence contours for (a) primary particles and (b) fifth-order agglomerates for a discharge with no neutral gas flow, and (c)-(d) with 225 sccm of gas flow. With the gas flow, primary particles and agglomerates alike are swept out to the outer portions of the reactor, away from the substrate surfaces.

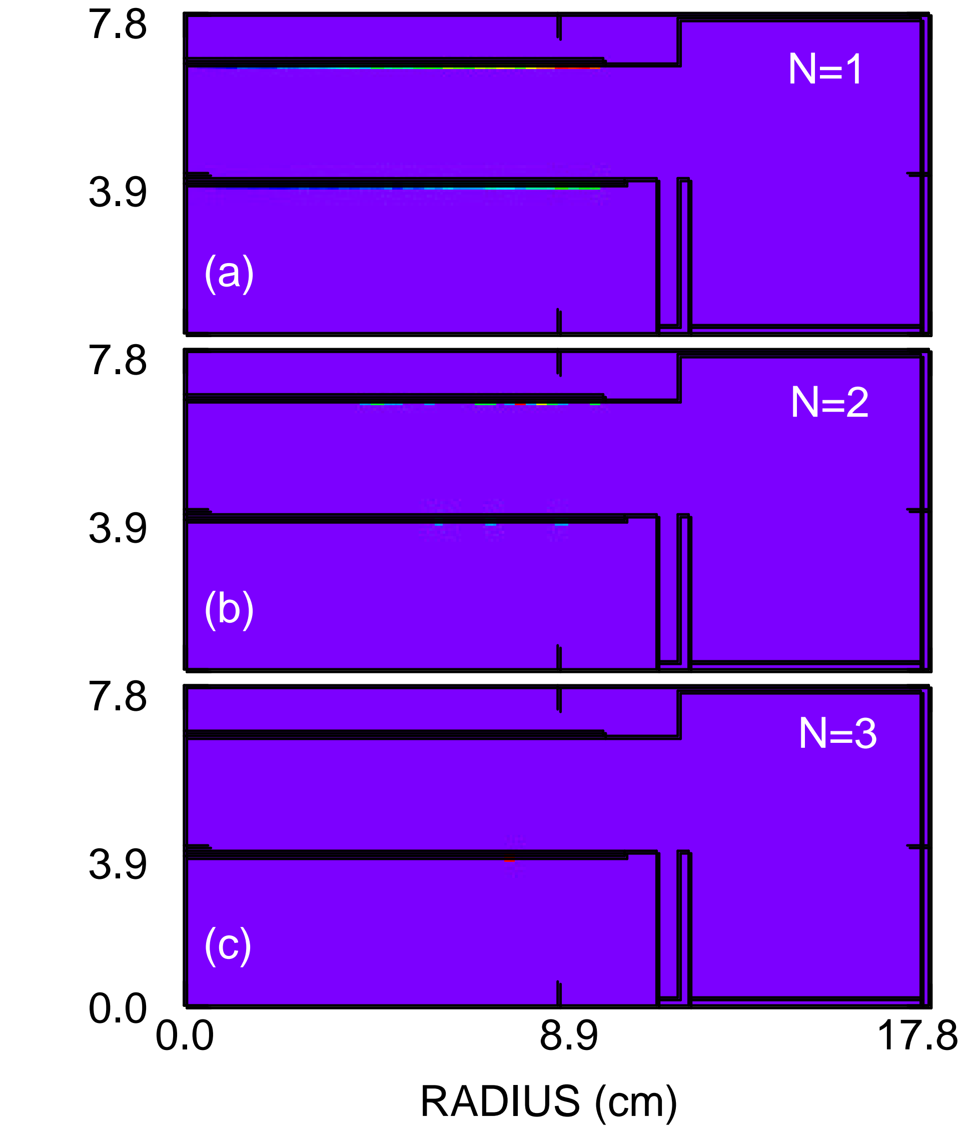

Figure 3.10. Surface contamination levels of (a) primary particles, (b) second-order agglomerates, and (c) third-order agglomerates in a 100 mTorr Ar discharge with 72 W of power. The primary particles are 1000 nm in radius, and no gas flow is used for this case.

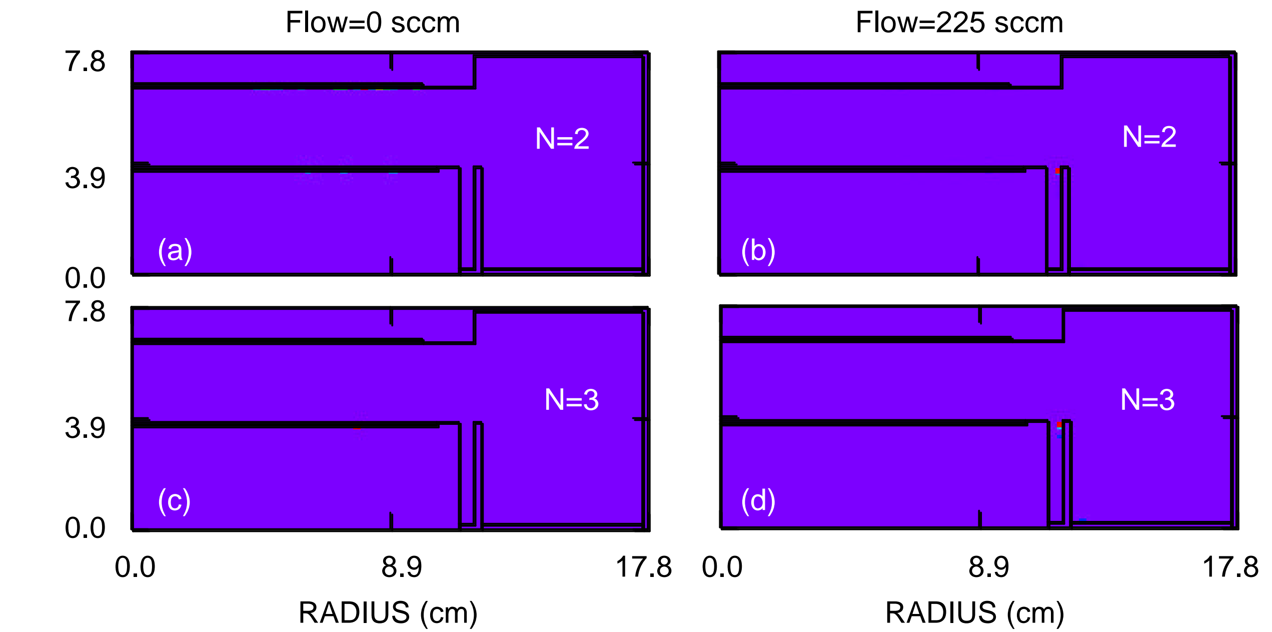

Figure 3.11. Surface contamination levels for the (a)-(b) second-order and (c)-(d) third-order agglomerates using 0 and 225 sccm of gas flow, respectively. Without gas flow, particles are readily driven to the electrode surfaces. With gas flow, however, particles are swept outwards and do not contaminate the electrodes or substrates.

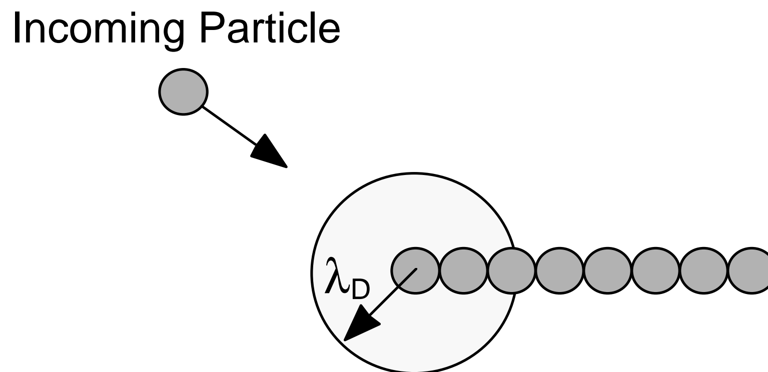

Figure 3.12. An illustration of the charge shielding effect. For a sufficiently long string of particles, an approaching particle only "sees" a fraction of the total surface charge residing on the string.

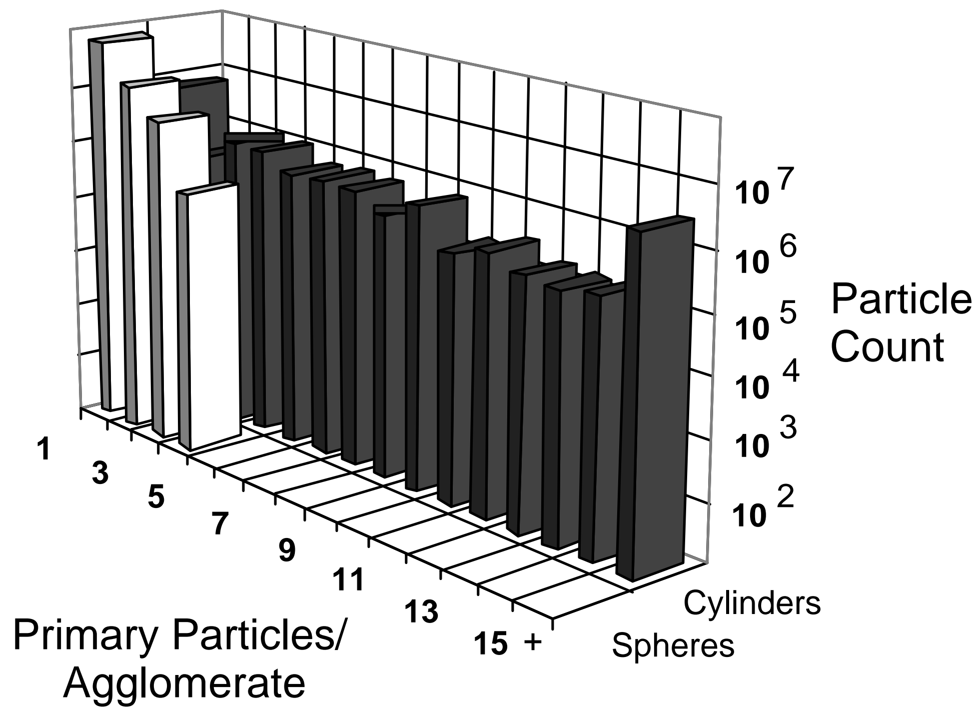

Figure 3.13. Relative populations of agglomerates formed using spherical and cylindrical agglomerates. The primary particles were 200 nm in radius and the power deposition for the discharge was 120 W.

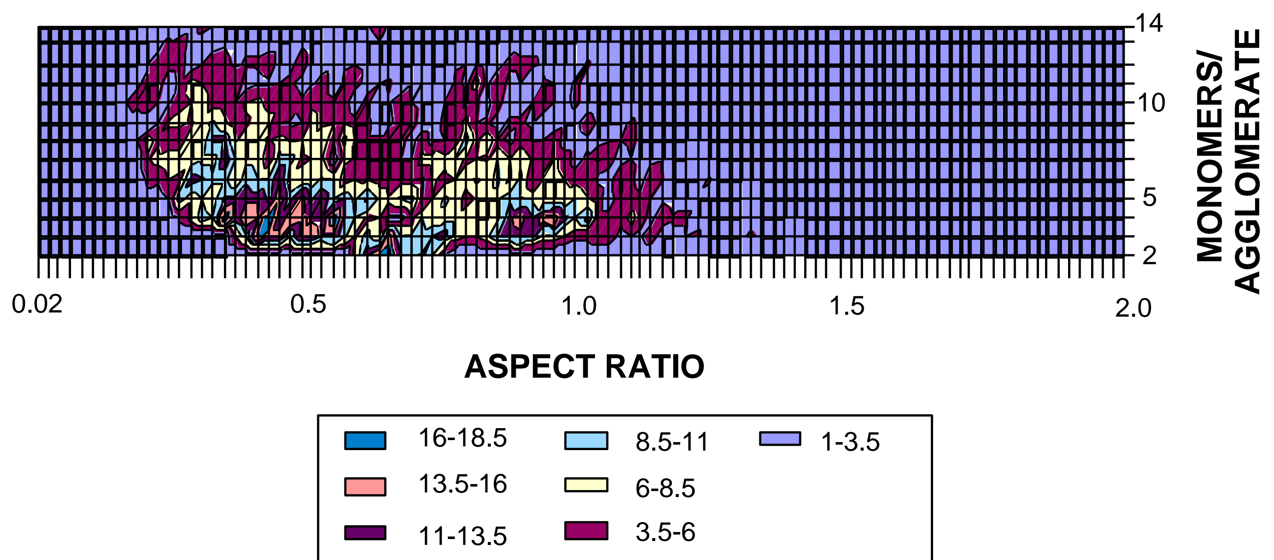

Figure 3.14. Aspect ratio, defined as *R/L* for cylindrical agglomerates, for a population of particles generated in the conditions of Figure 3.13. Agglomerates of all sizes grow somewhat preferentially into long thin rods, with low aspect ratios below 1.

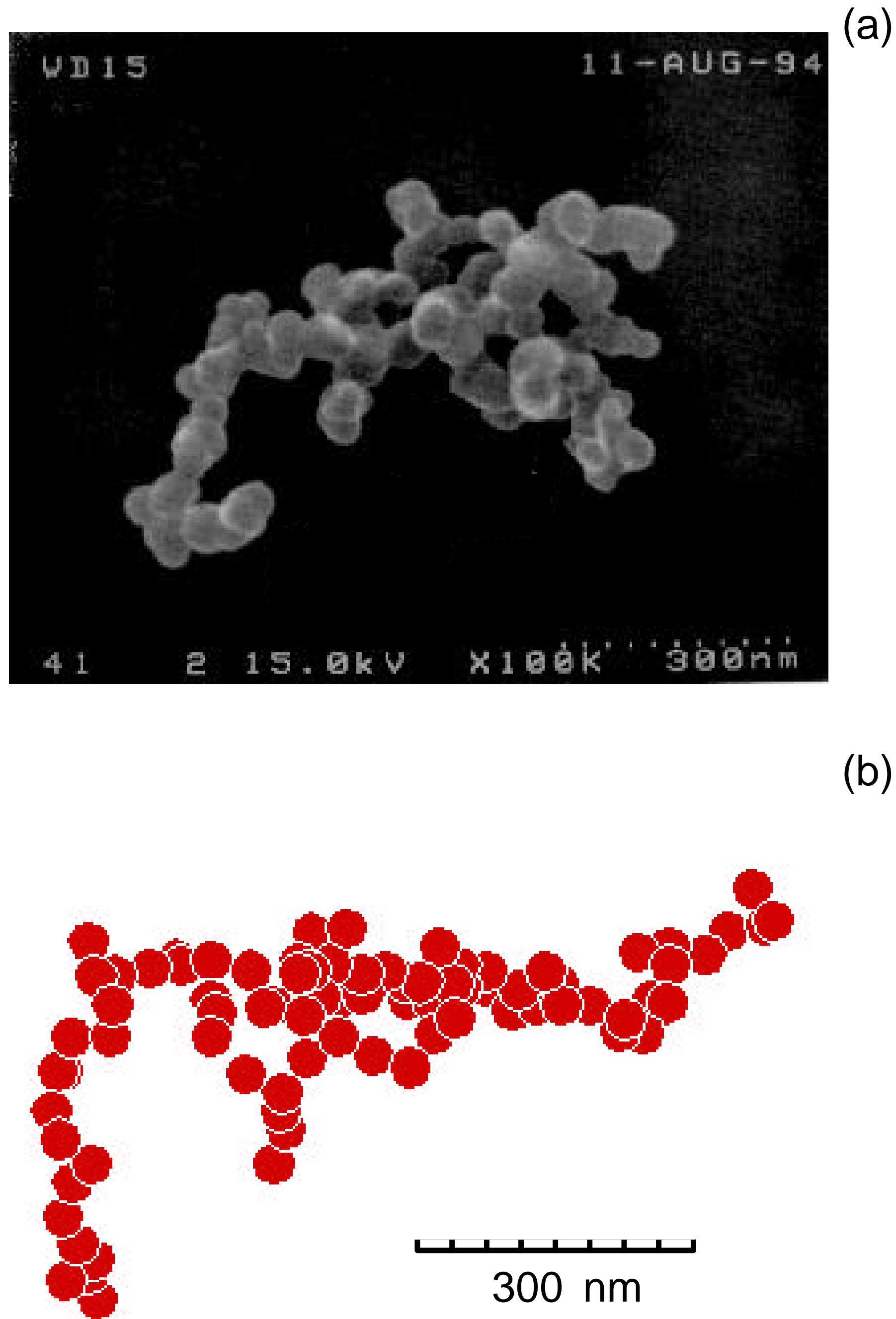

Figure 3.15. Comparison of (a) an experimentally collected particle and (b) particle generated by the MD-PAM simulation. The discharge in (a) is a 40 mTorr, SF_6 plasma. The primary particles in both (a) and (b) are approximately 40 nm in radius.

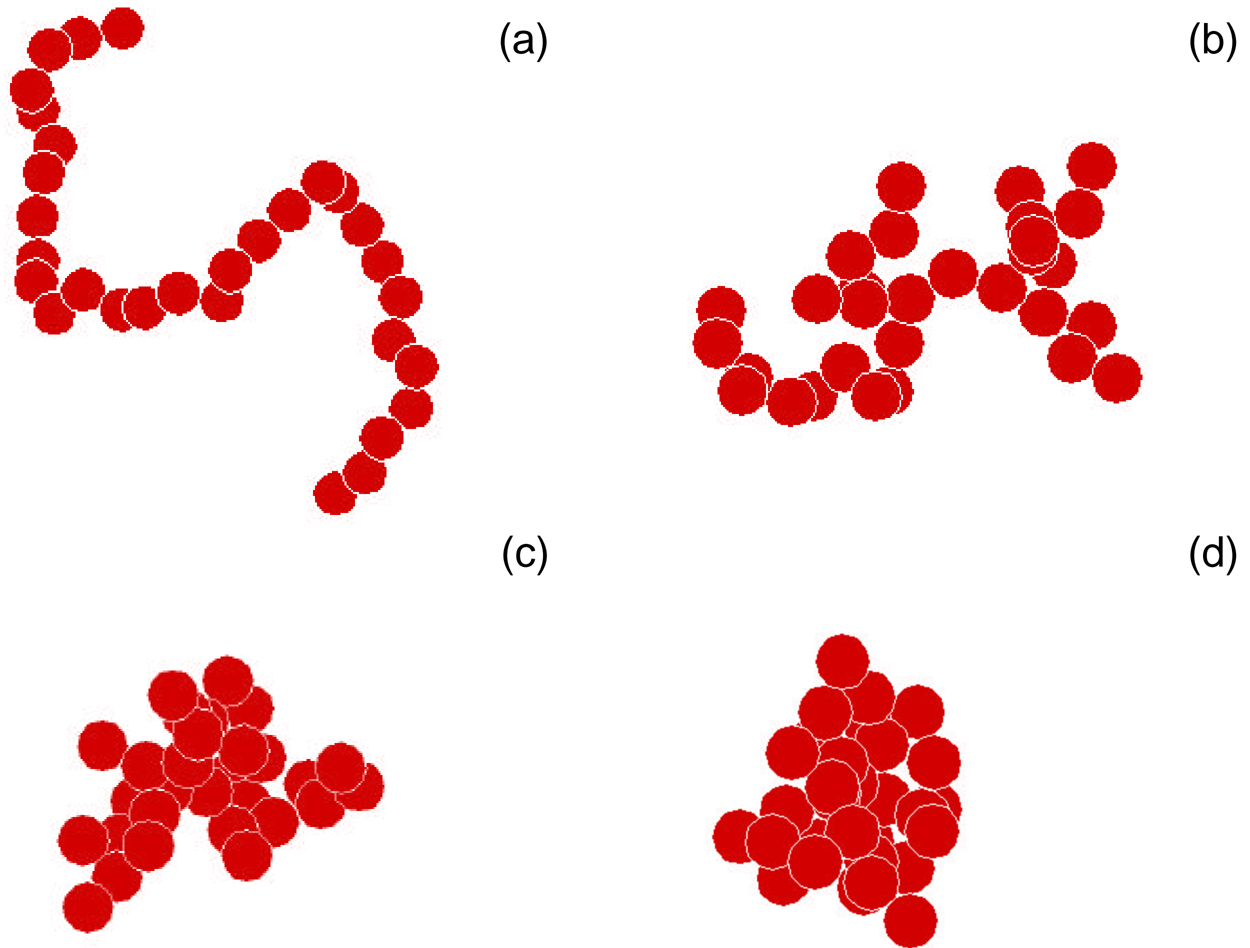

Figure 3.16. Agglomerates generated by the MD-PAM simulation using 1000 nm-radius primary particles, and with approach velocities of (a) 50 cm/s, (b) 75 cm/s, (c) 100 cm/s, and (d) 300 cm/s. As the velocity increases, the agglomerate growth becomes more ballistic.

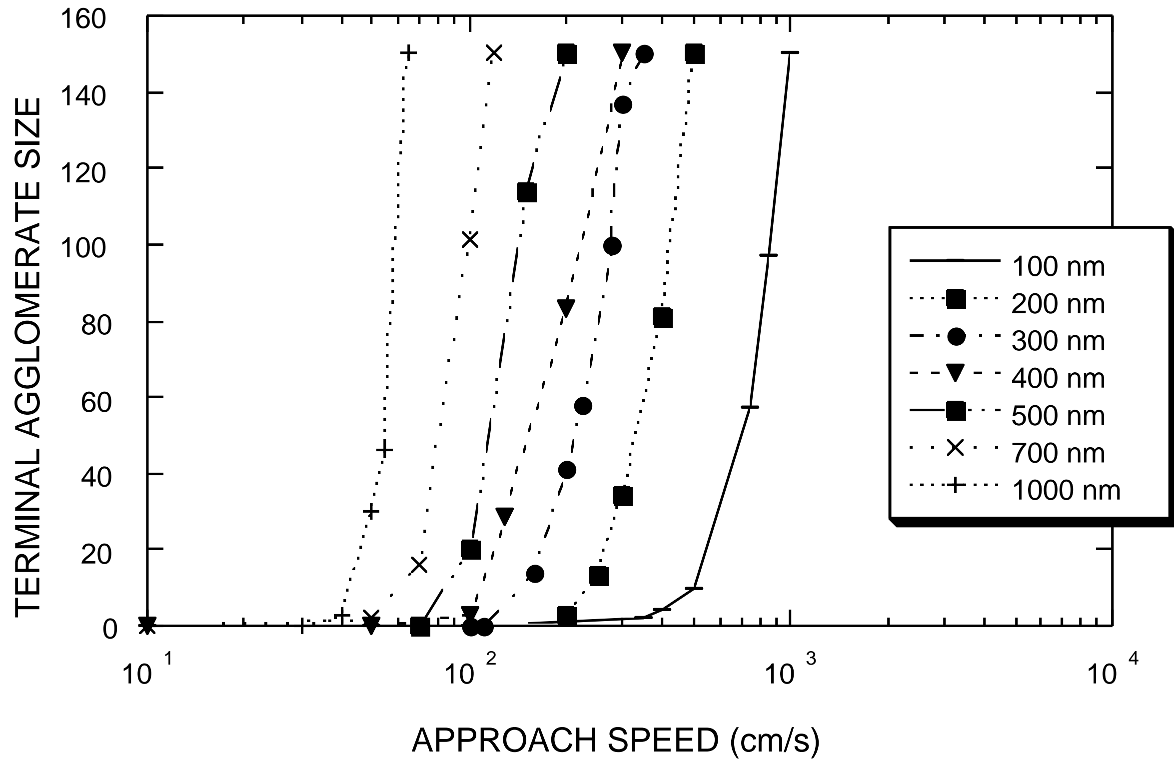

Figure 3.17. Maximum agglomerate size attained (limit 150) for various approach velocities. Larger primary particles require less speed to agglomerate.

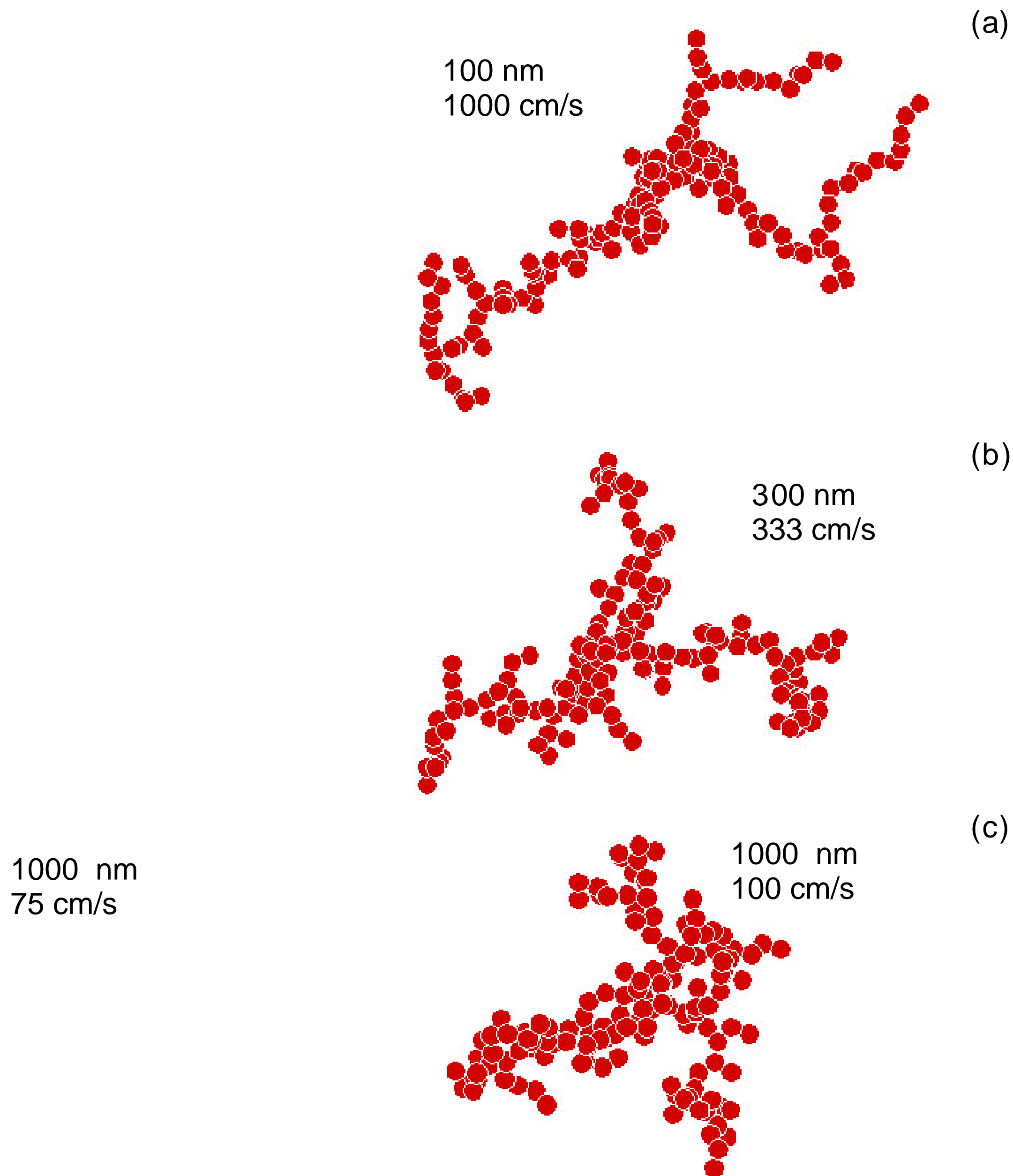

Figure 3.18. Morphology of agglomerates generated using a constant ***b*** value, with radii and approach speeds of (a) 100 nm and 1000 cm/s, (b) 300 nm and 300 cm/s, and (c) 1000 nm and 100 m/s. The same ***b*** value produces agglomerates similar in shape to each other.

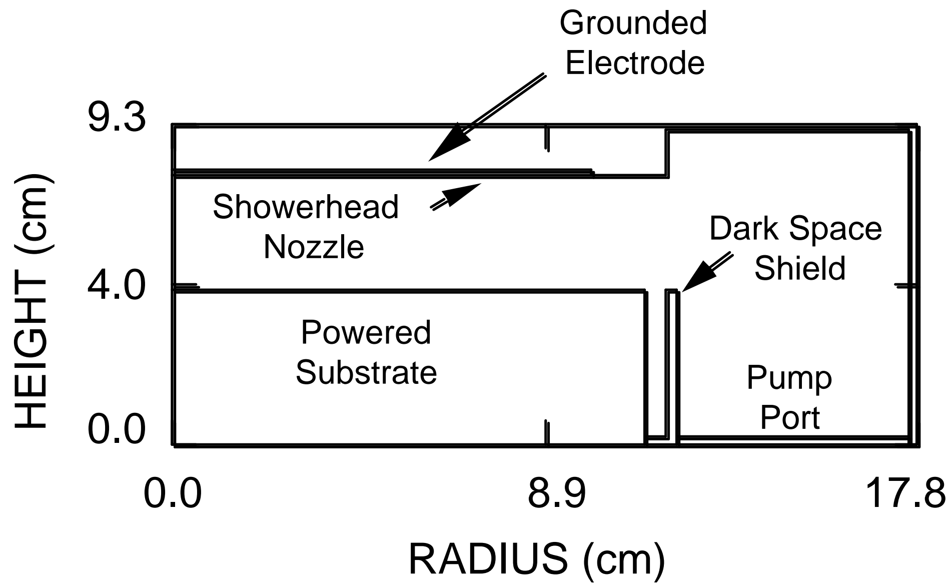

Figure 3.19. Schematic of the RIE reactor used for the simulation results of Section III. C. The interelectrode gap is larger than the reactor shown in Figure 3.1, and there is no wafer embedded in the powered electrode.

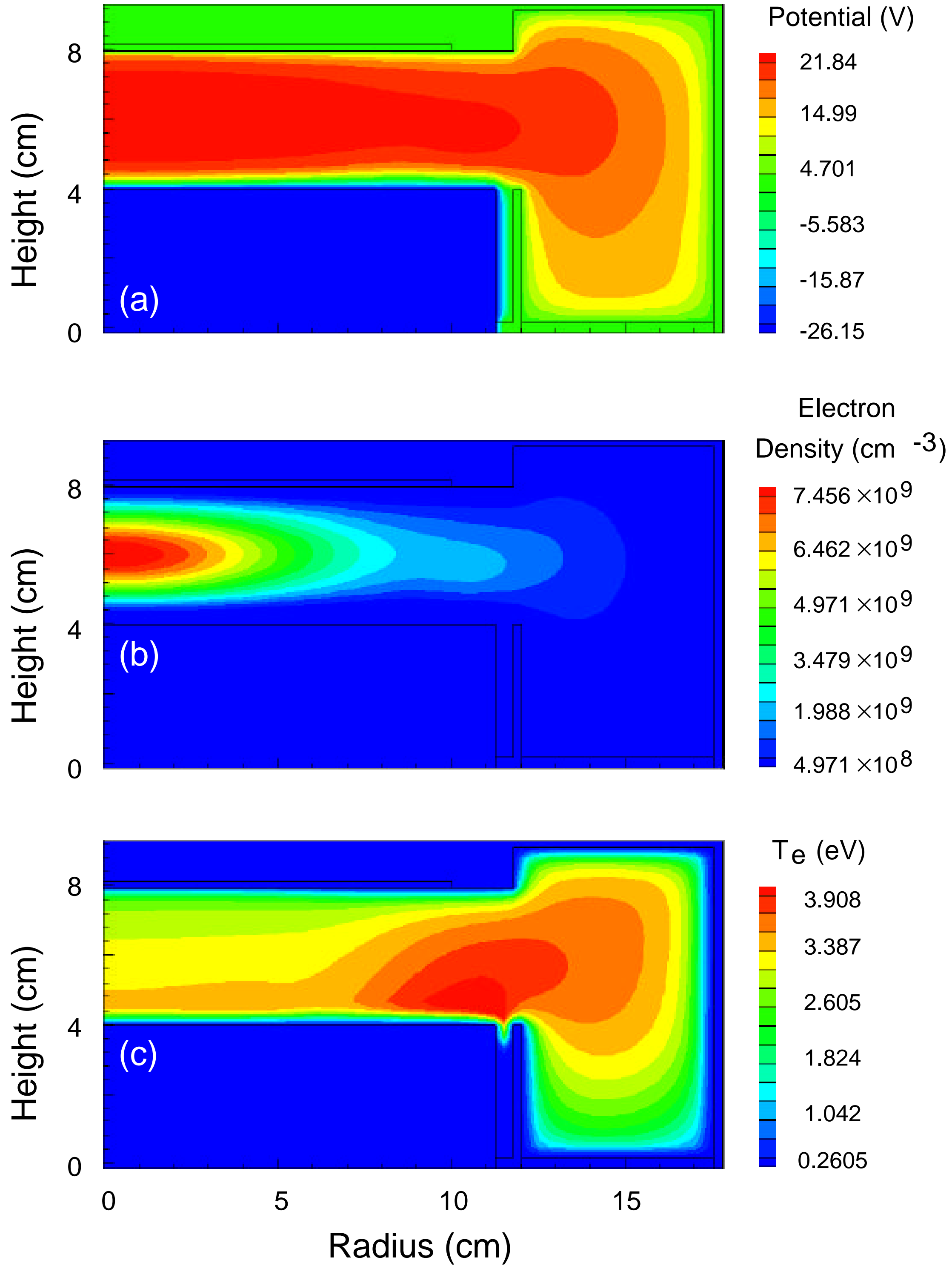

Figure 3.20. (a) Electric potential, (b) electron density, and (c) electron temperature for the reactor of Figure 3.19 driving a 100 mTorr Ar discharge. The power deposition is 21.17 W.

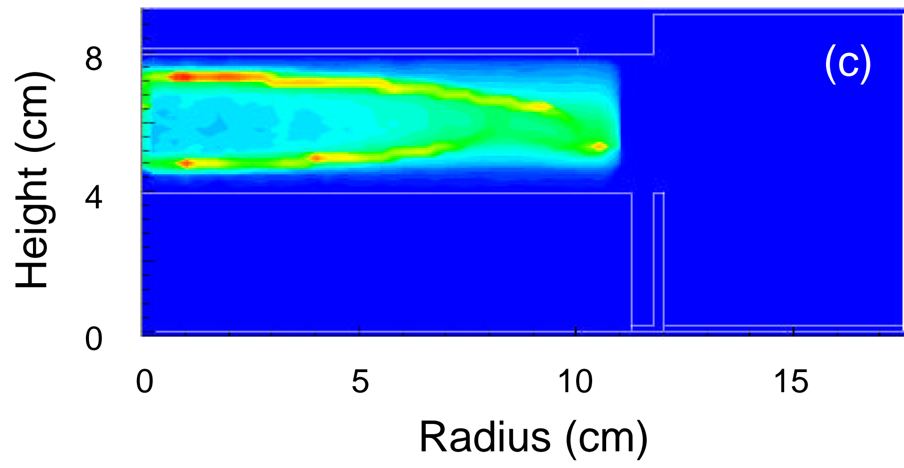
Height (cm)
Radius (cm)
(c)
0
4
8
0
5
10
15

Figure 3.21. Time fluence contours for 200 nm radius primary particles in a 100 mTorr, 21.17 W Ar discharge. Particles are trapped in two distince layers near the electrodes.

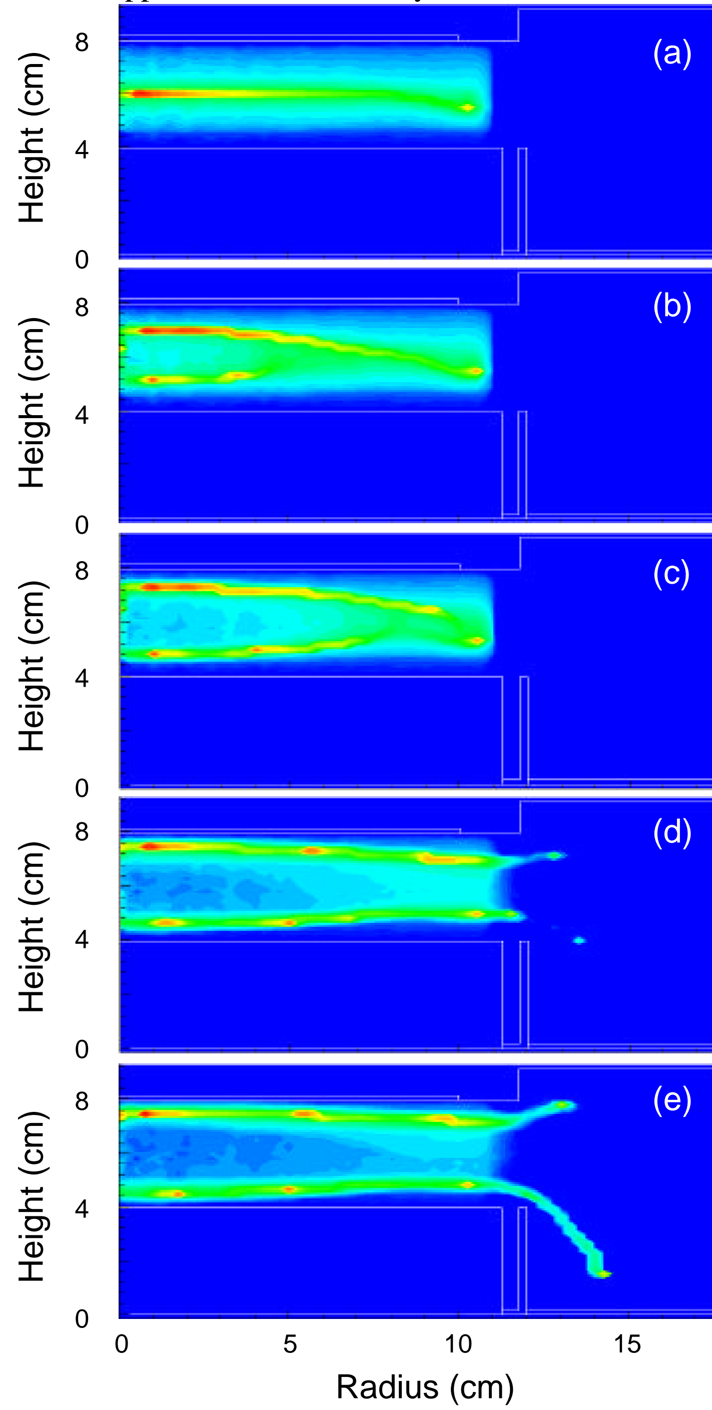

Figure 3.22. Time fluence contours for the primary particles in Figure 3.21. using (a) 2 W, (b) 11 W, (c) 21 W, (d) 53 W, and (e) 106 W of RF power. At the higher powers, particles are driven towards the surfaces of the reactor by the higher ion-drag forces.

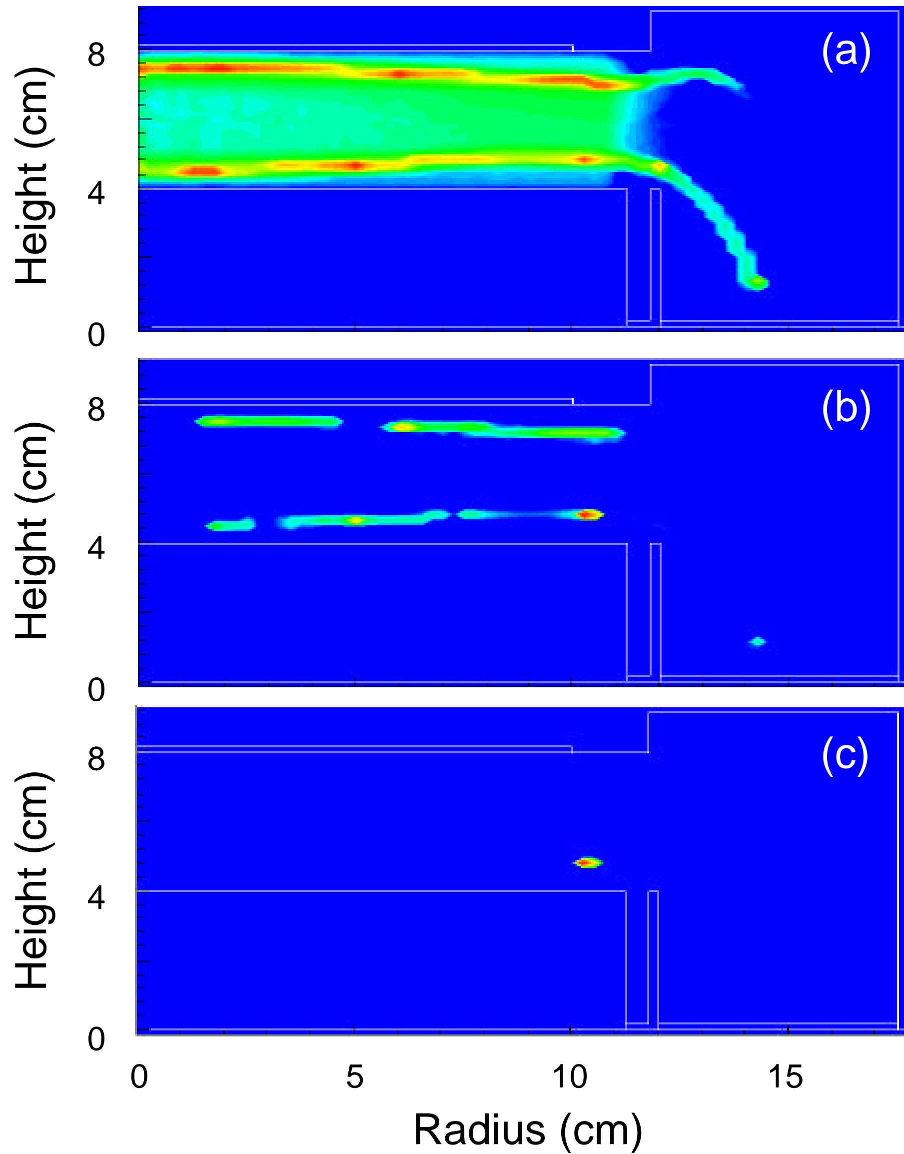

Figure 3.23. Time fluence contours for (a) primary particles, (b) second-order, and (c) third-order agglomerates in a 100 mTorr, 21 W Argon discharge. Primary particles are 1000 nm in radius, and use cylindrically shaped agglomerates. Agglomerates are formed by primary particles en route or residing in trapping layers and sites.

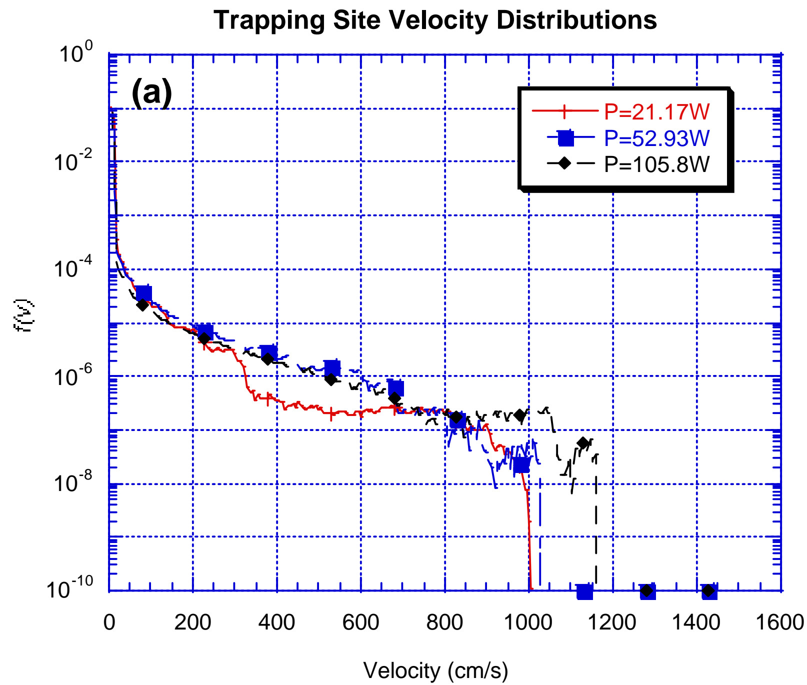

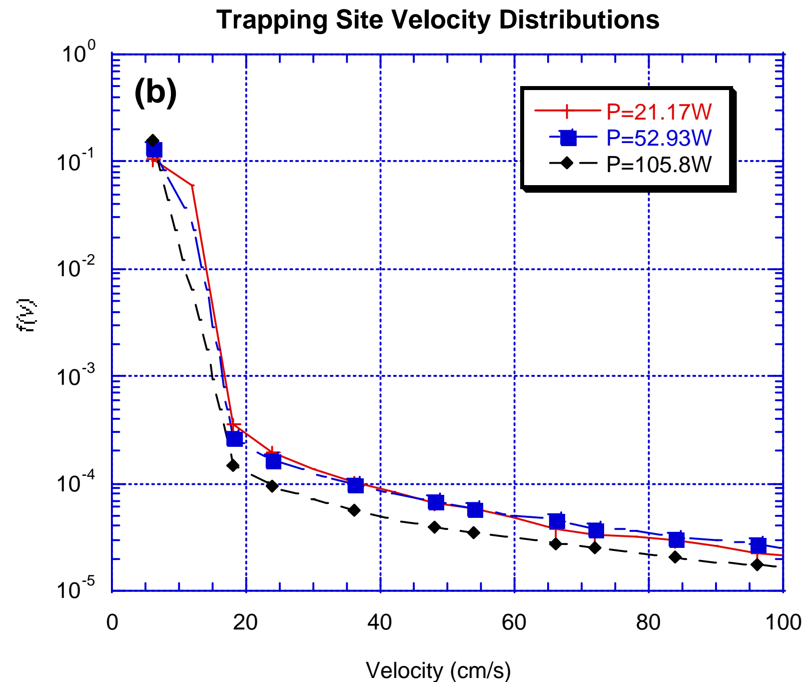

Figure 3.24. Trapping site velocity distributions for 200 nm primary particles in 21.17, 52.93, and 106-W Ar discharges. (a) Full distribution, and (b) an expanded view of the low velocity portion of the distribution. Higher powers result in higher average velocities and higher maximum velocities. Lower powers have a more heavily populated distribution at low velocities.

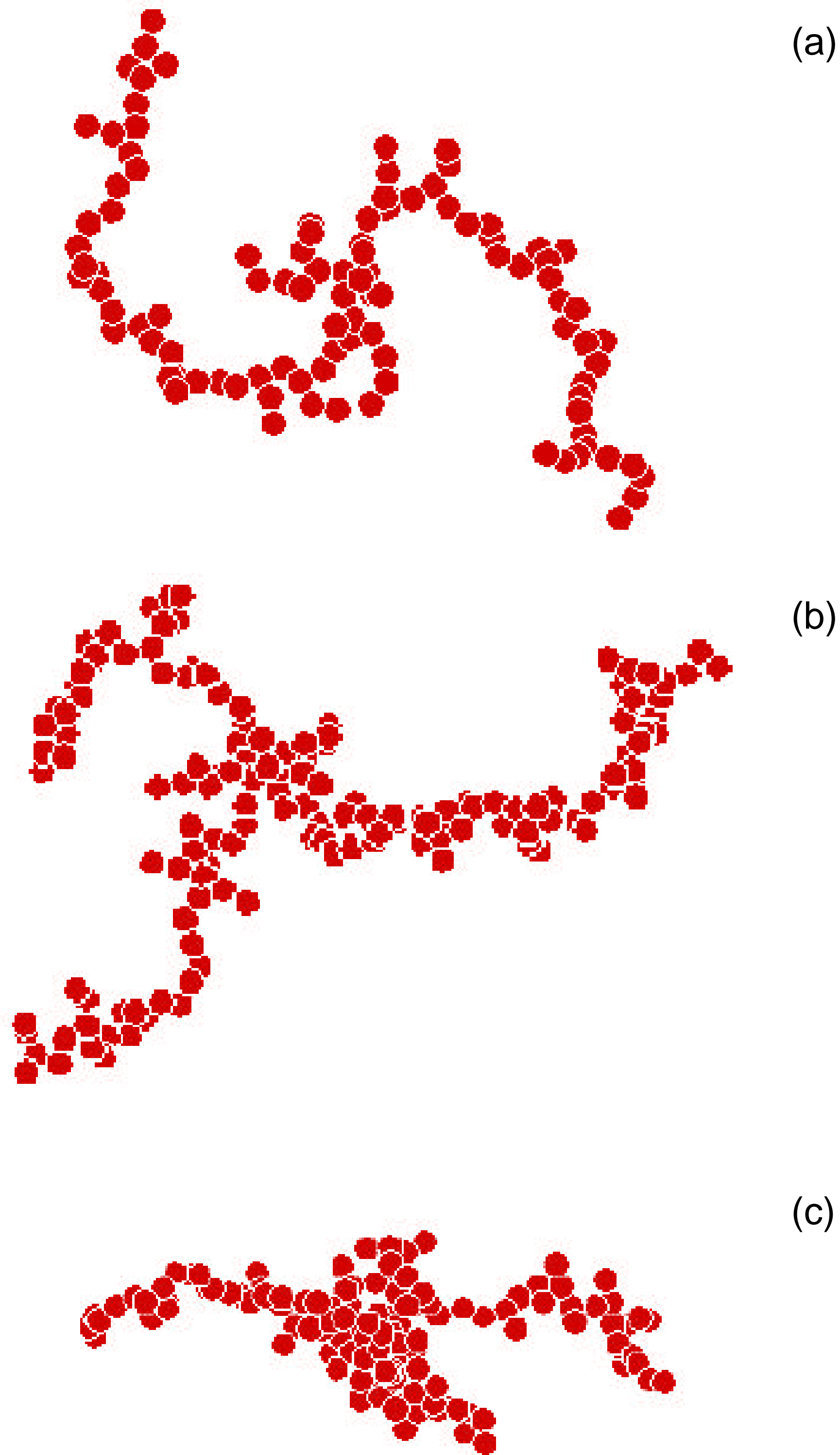

Figure 3.25. Morphology of particles generated by the discharges of Figure 3.22. (a) 21.17 W, (b) 53 W, and (c) 106 W. As the power increases, the growth mechanism shifts from diffusive to ballistic mechanisms.

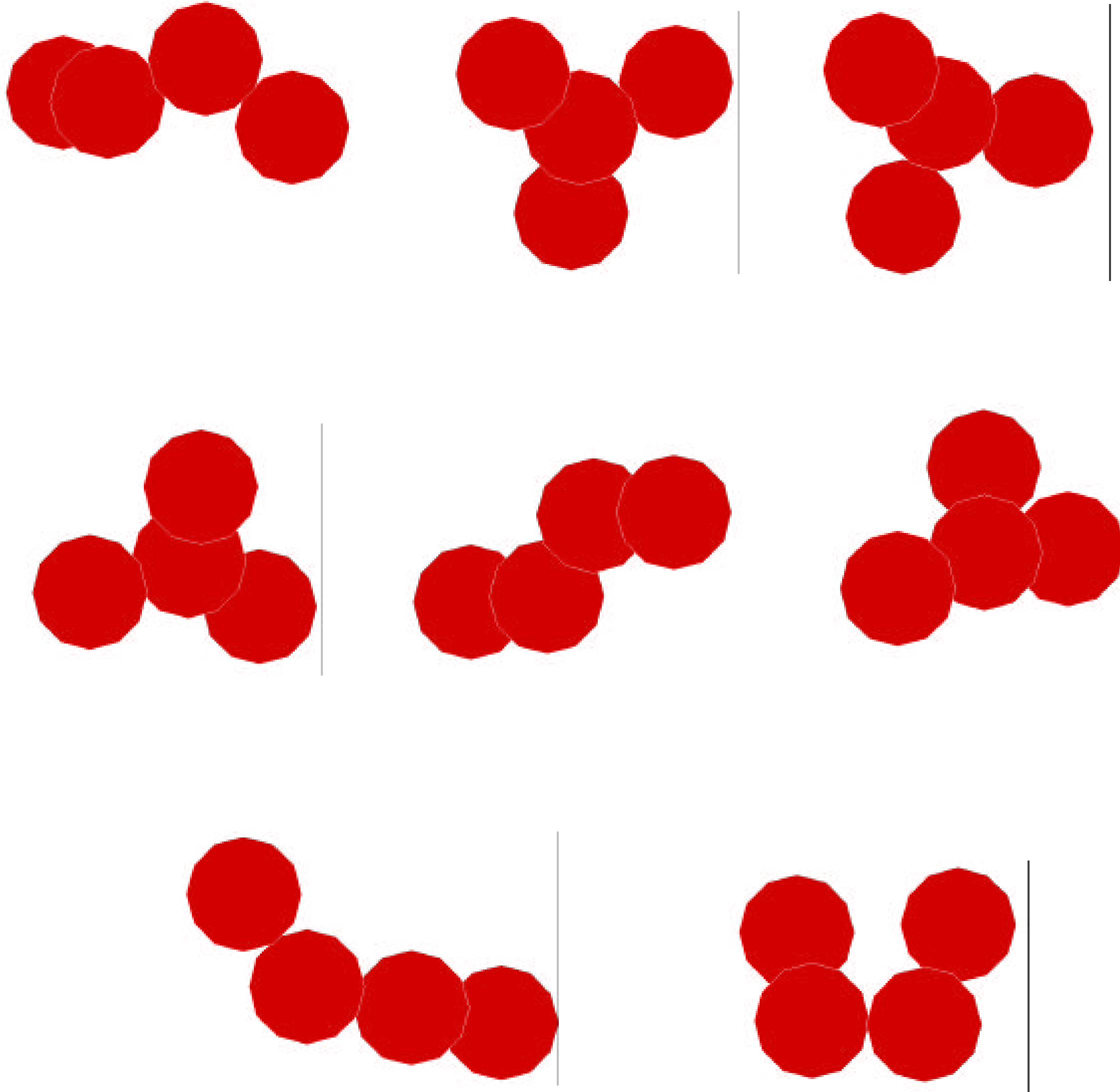

Figure 3.26. Samples of fourth-order agglomerates grown in a 100 mTorr Argon discharge with an RF power of 21 W using 200 nm radius primary particles. Using this velocity distribution, primary particles have a high enough average velocity to generate compact clusters as well as colinear chains.

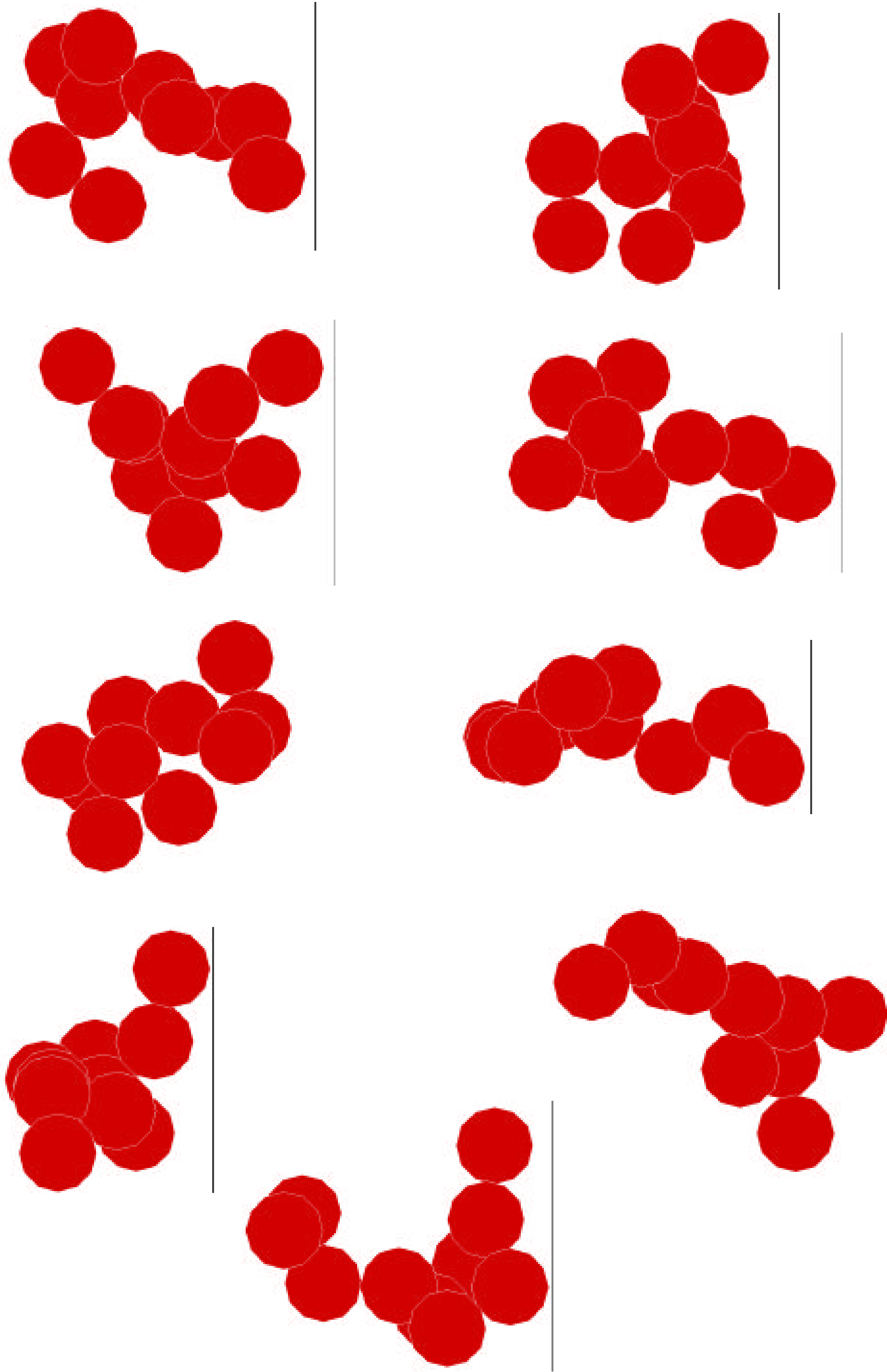

Figure 3.27. Tenth order agglomerates grown in the discharge of Figure 3.26. Agglomerates of this size grow preferentially into low fractal dimension shapes since the velocity distribution does not result in high enough β values to produce compact morphologies.

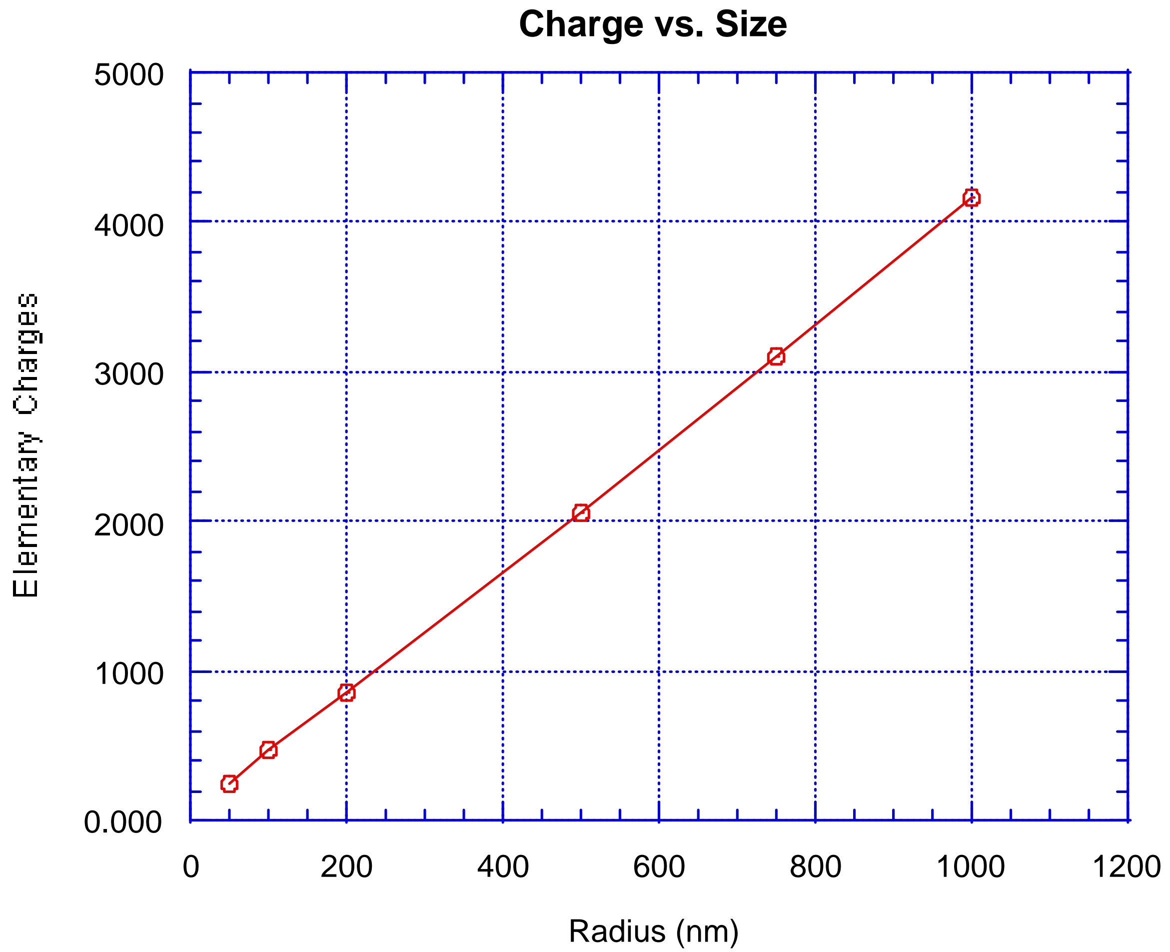

Figure 3.28. Computed surface charge on dust particulates as a function of their radius. As the particle increases in size, the surface charge increases very nearly linearly.

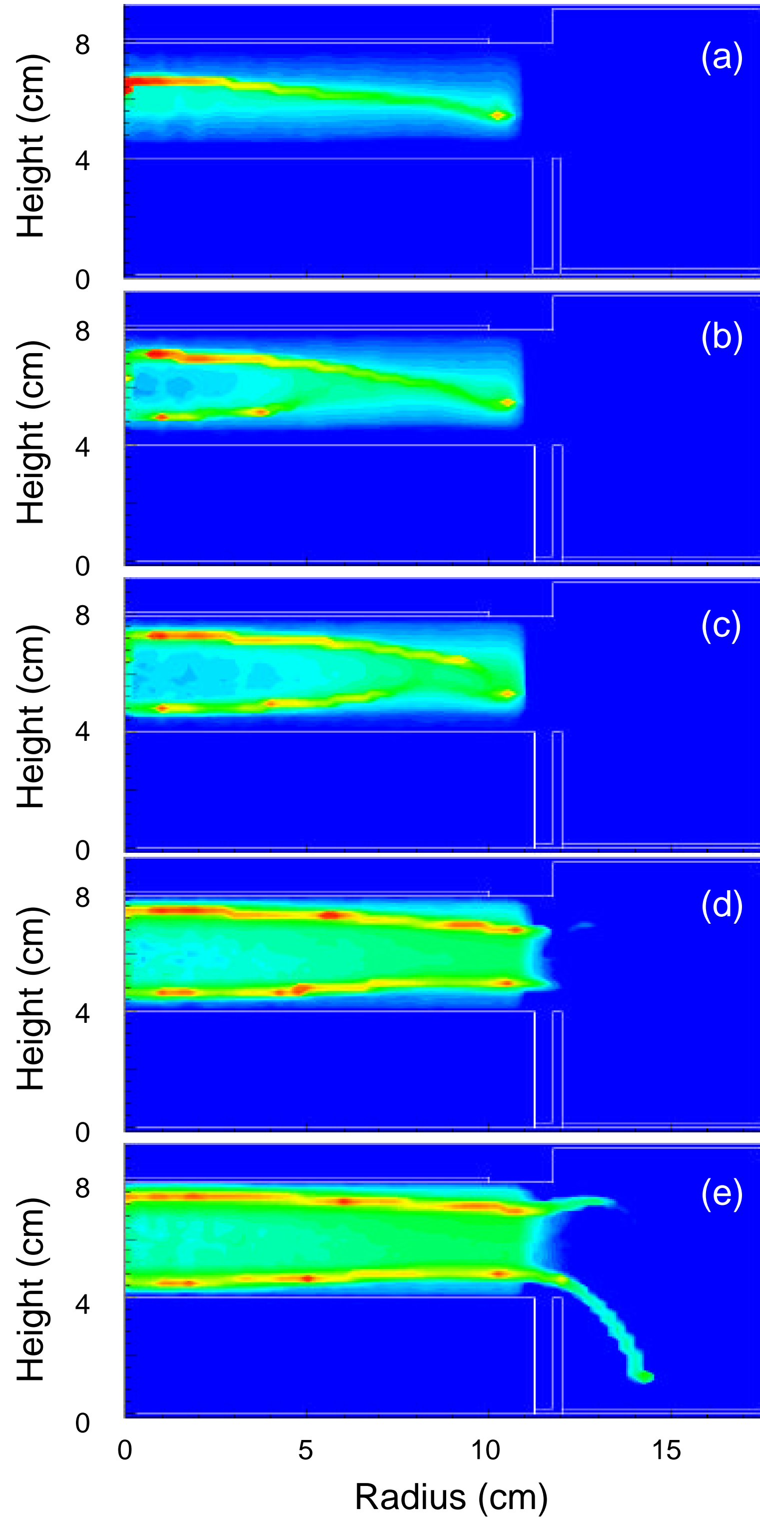

Figure 3.29. Time fluence contours for primary particles in a 21.17 W 100 mTorr Argon discharge, having radii of (a) 50 nm, (b) 200 nm, (c) 500 nm, (d) 750 nm, and (e) 1000 nm. There is no neutral gas flow. The larger particles are driven closer to the surfaces by the increasing ion-drag forces, while electrostatic forces dominate at smaller particle sizes.

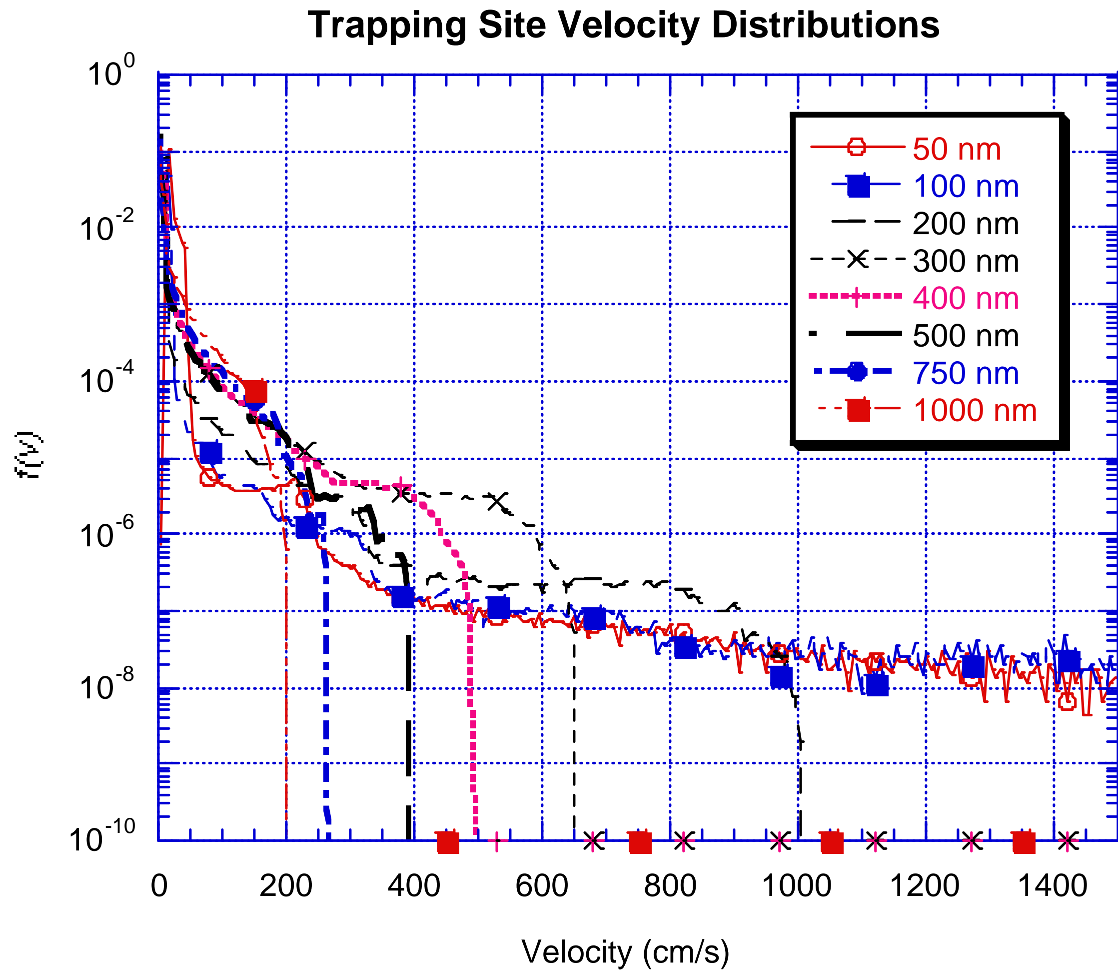

Figure 3.30. Trapping site velocity distributions for primary particles 50 nm to 1000 nm in radius. The smaller particles are accelerated to higher average and maximum velocities. Maximum velocities decrease dramatically with increasing radius.

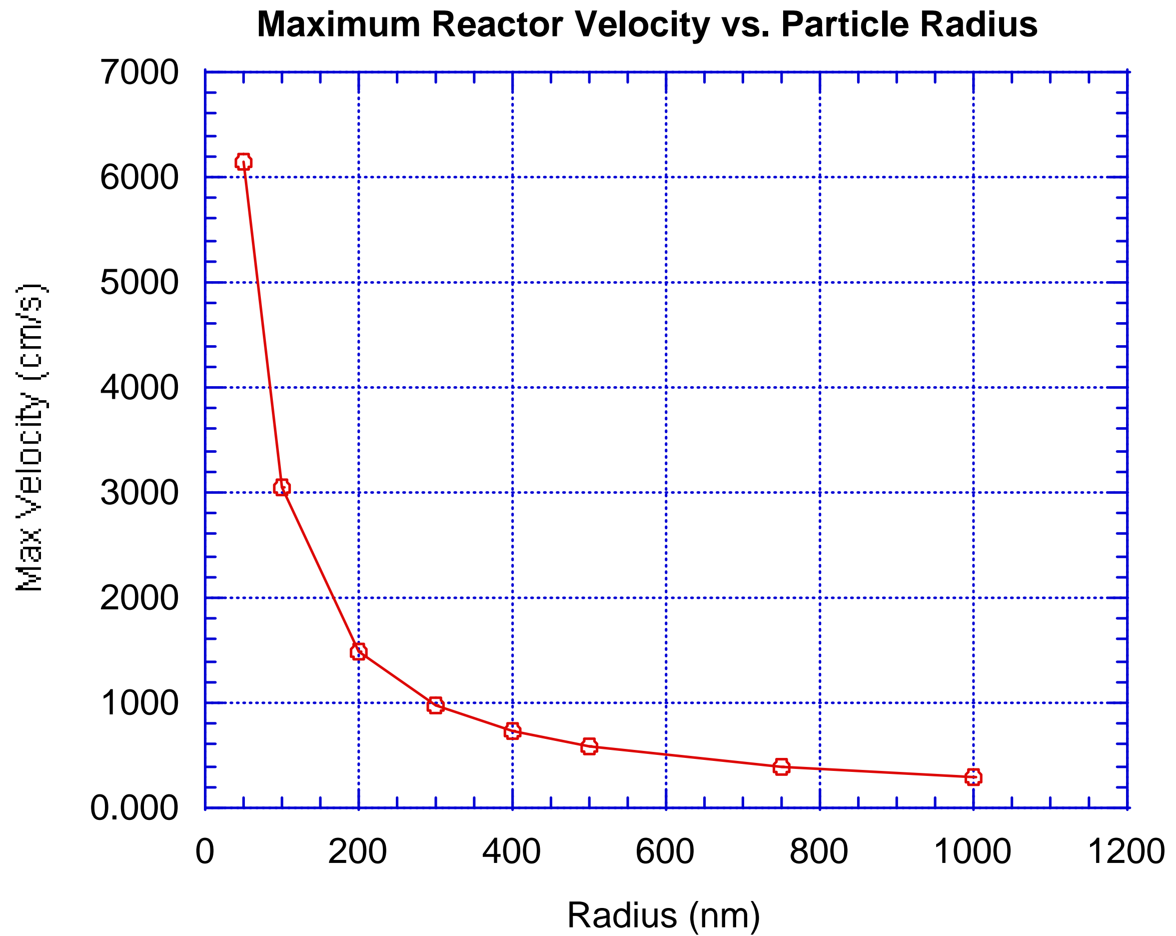

Figure 3.31. Maximum primary particle velocity as a function of particle radius. The maximum attained velocity scales roughly as $1/R^2$.

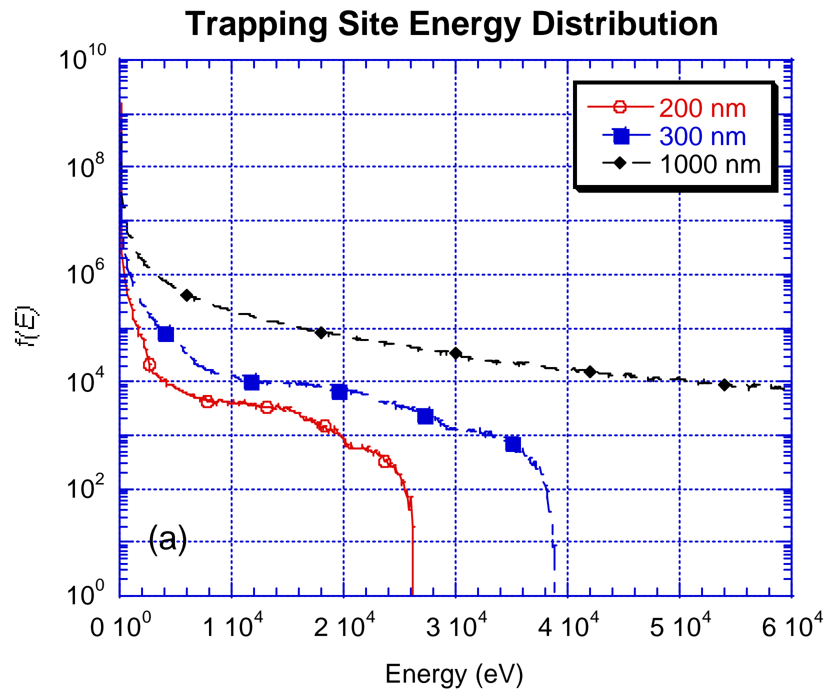

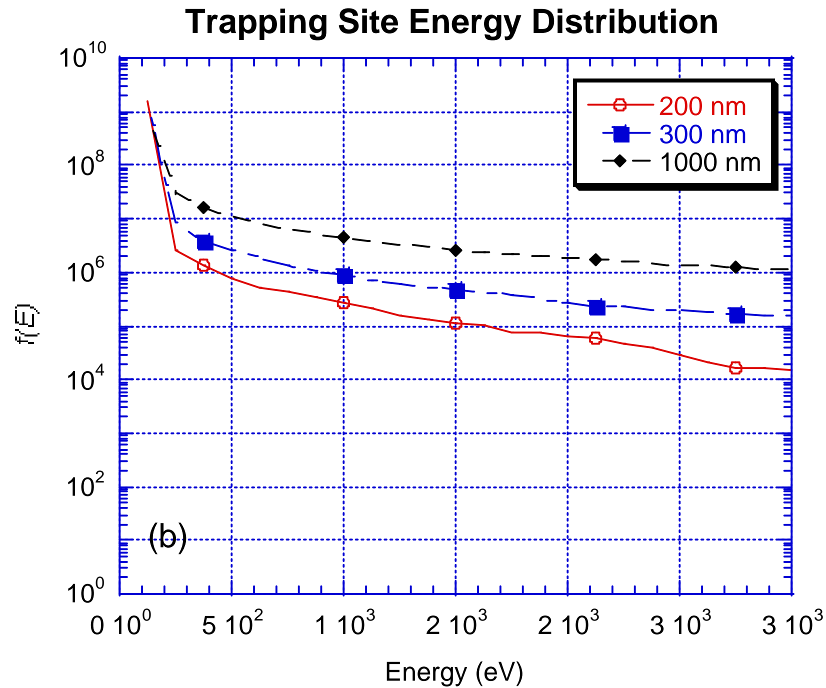

Figure 3.32. Kinetic energy distributions for 200 nm, 300 nm, and 1000 nm radius particles in a 21.17 W 100 mTorr Argon discharge. (a) Complete distribution, and (b) an expanded view of the low energy range. Although much slower on average, the larger particles still carry on average a higher kinetic energy, making them more favorable for agglomeration.

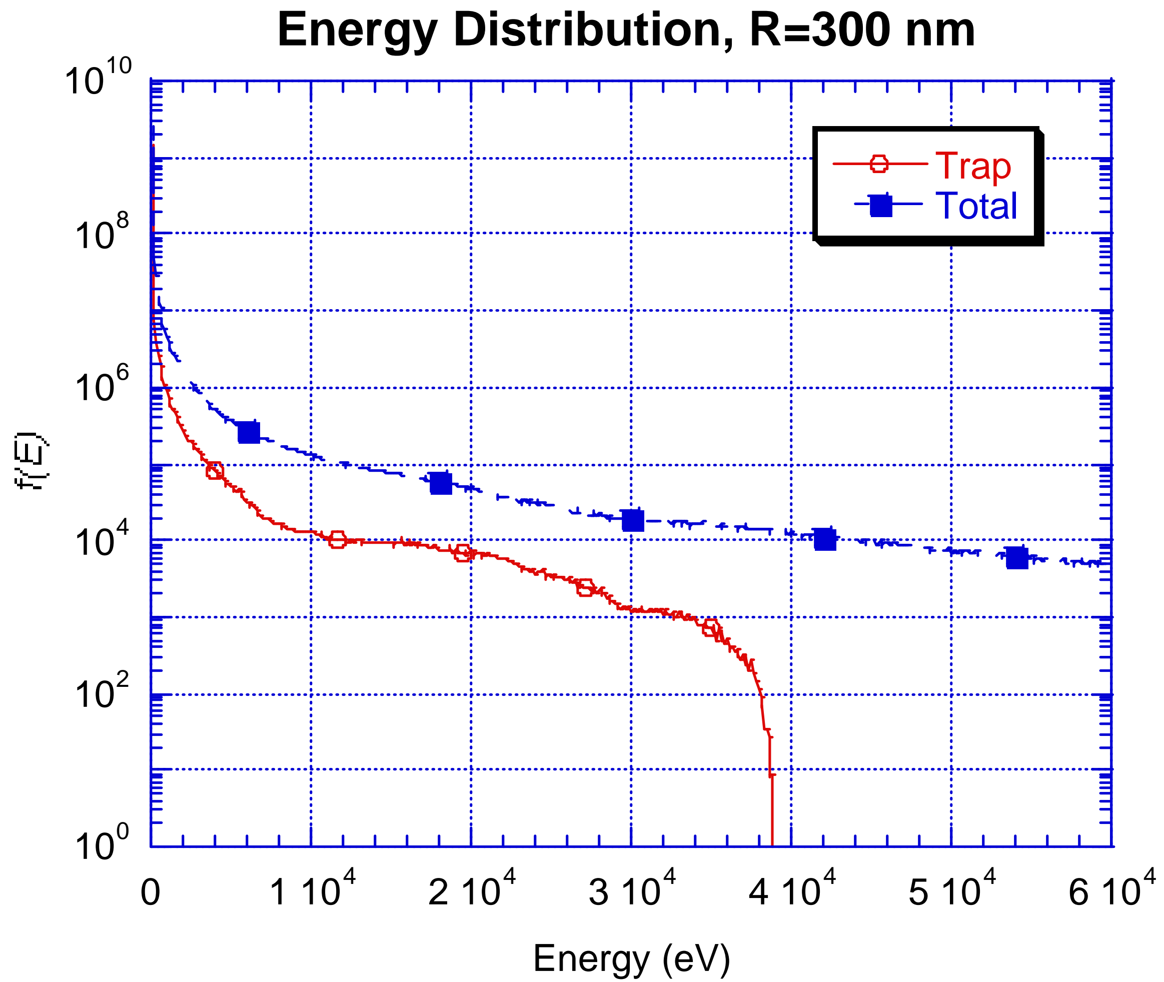

Figure 3.33. Trapping site and total reactor kinetic energy distributions for 300 nm primary particles. Particles can attain much higher velocities outside the trapping regions.

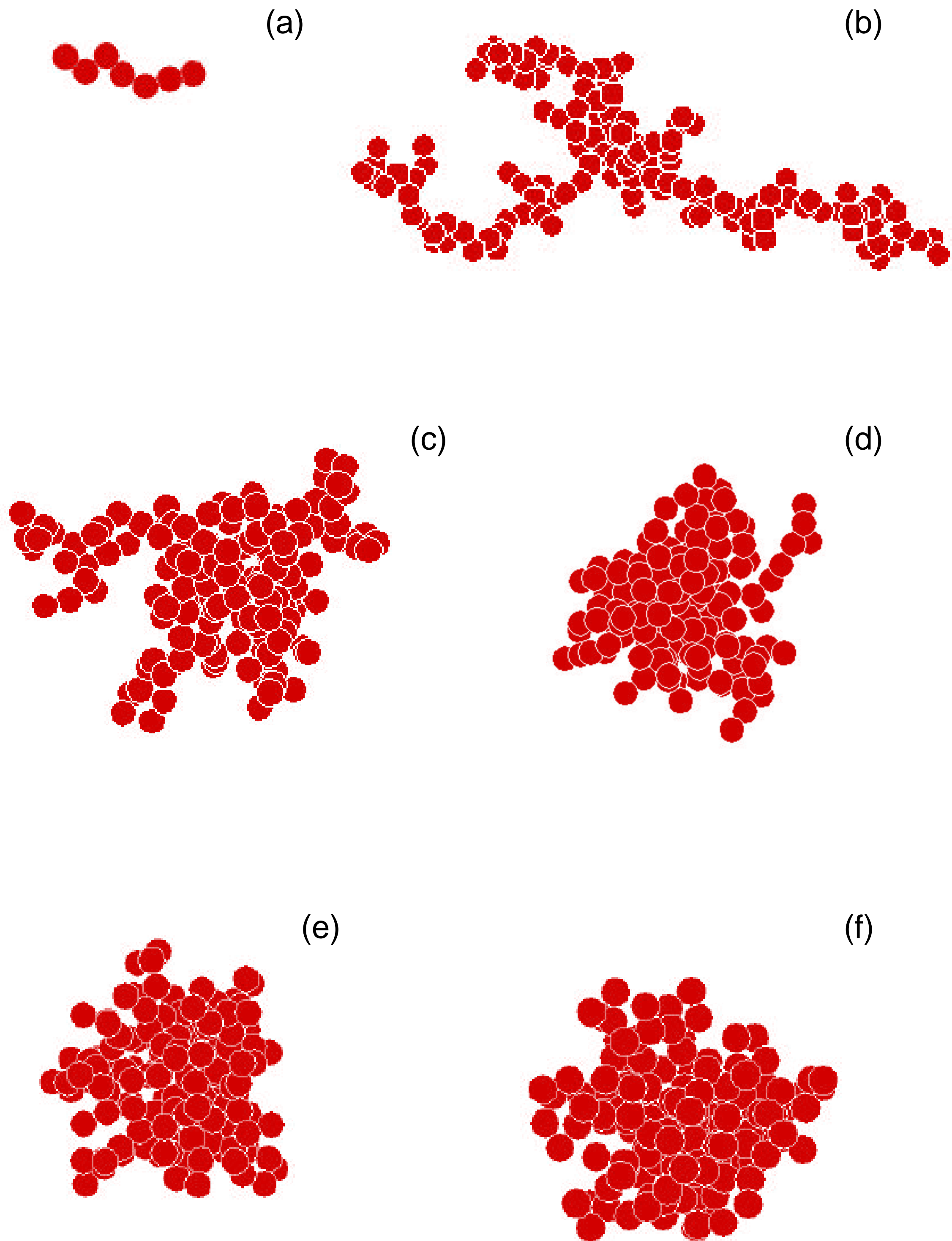

Figure 3.34. Agglomerates generated in a 21.17 W Ar discharge using (a) 100 nm, (b) 200 nm, (c) 300 nm, (d) 400 nm, (e) 500 nm, and (f) 1000 nm radius primary particles. At approximately 300 nm, the growth mechanism shifts from diffusive growth to ballistic, creating compact agglomerate structures.

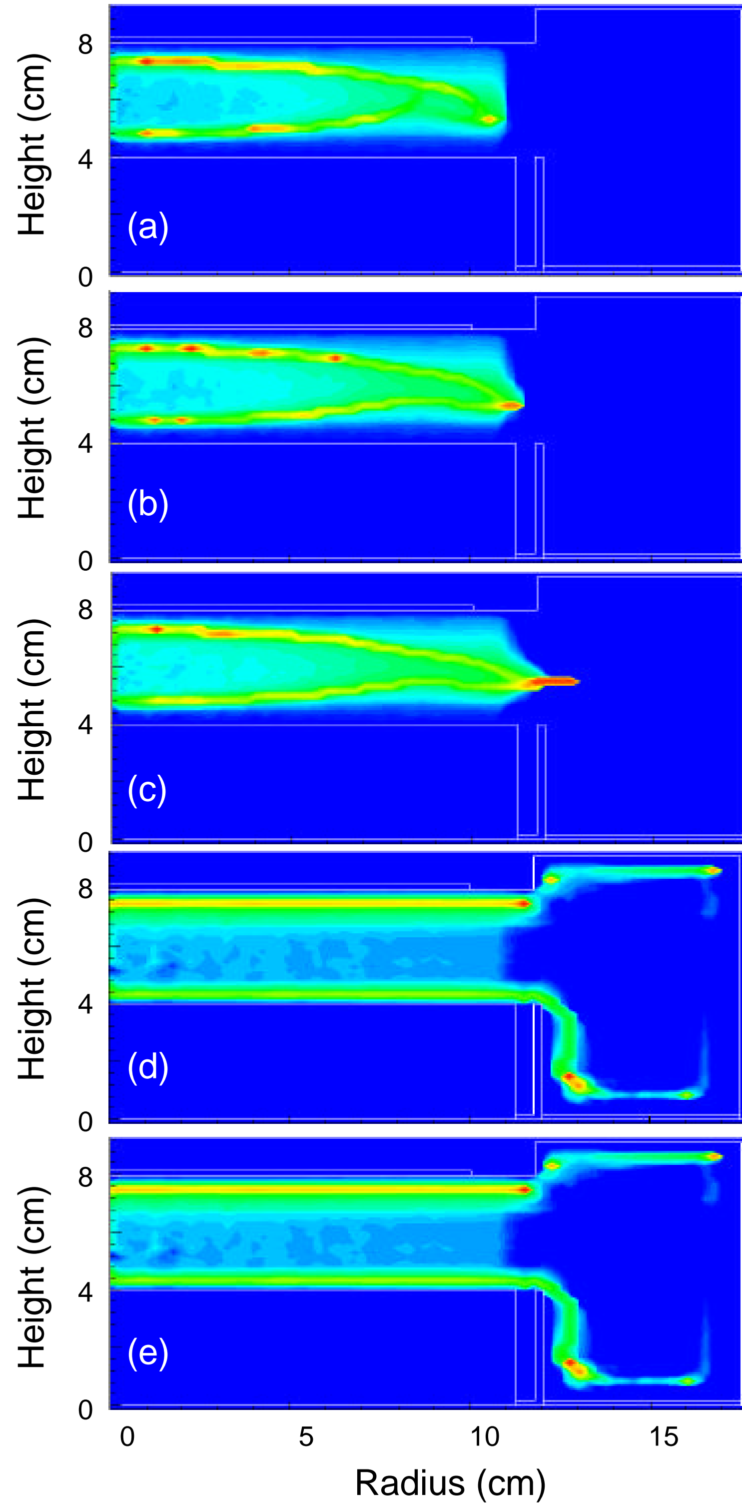
Height (cm)
8
4
0
(a)
(b)
(c)
(d)
(e)
0
5
10
15
Radius (cm)

Figure 3.35. Time fluence contours for 200 nm primary particles in a 21.17 W discharge having (a) 10 sccm, (b) 50 sccm), (c) 100 sccm, (d) 250 sccm, and (e) 500 sccm of neutral gas flow. Above 100 sccm, there is sufficient gas flow to push the particle to the outer regions of the reactor.

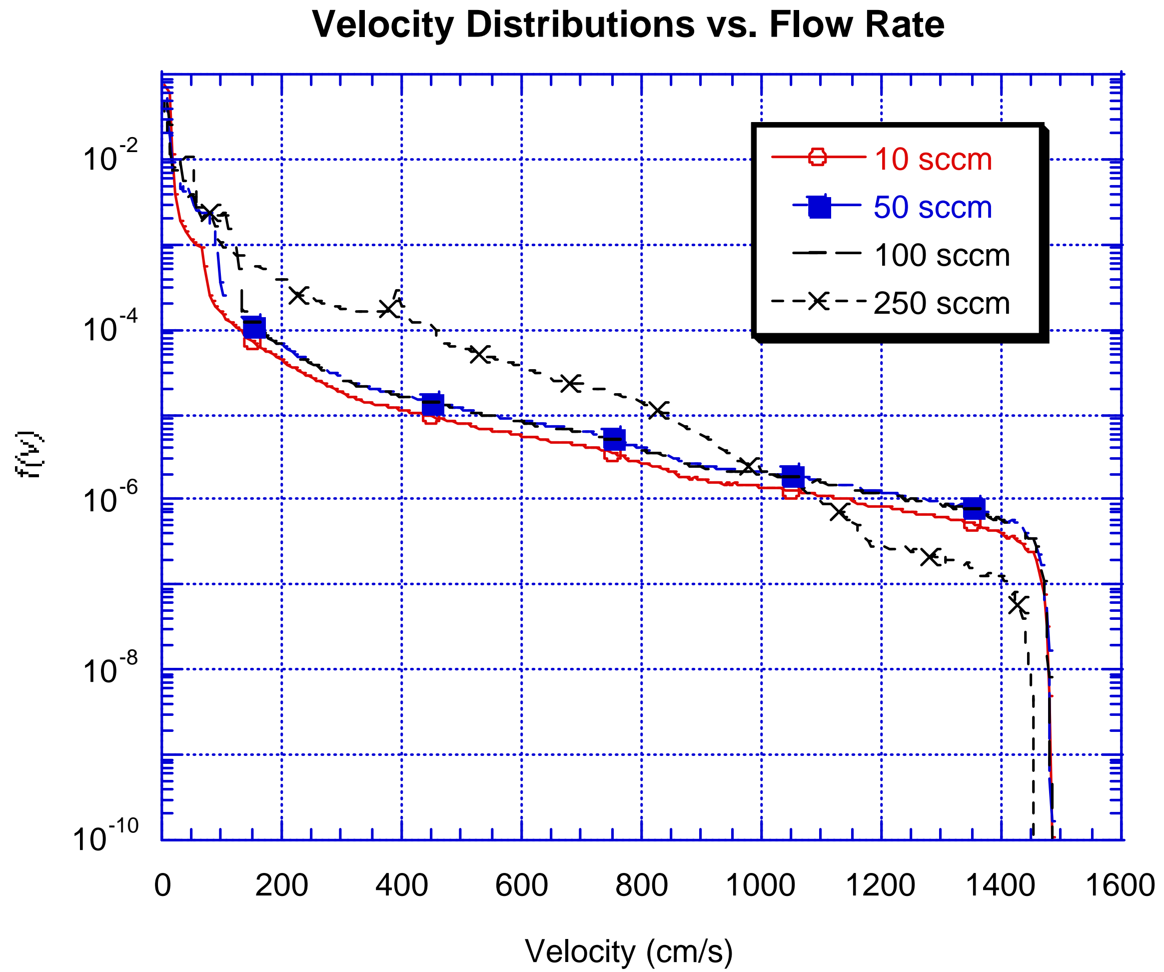

Figure 3.36. Total velocity distributions for the primary particles of Figure 3.33 (a)-(d). With 250 sccm of gas flow, the velocity distribution is significantly shifted. On average, particles have a higher velocity with increasing gas flows.

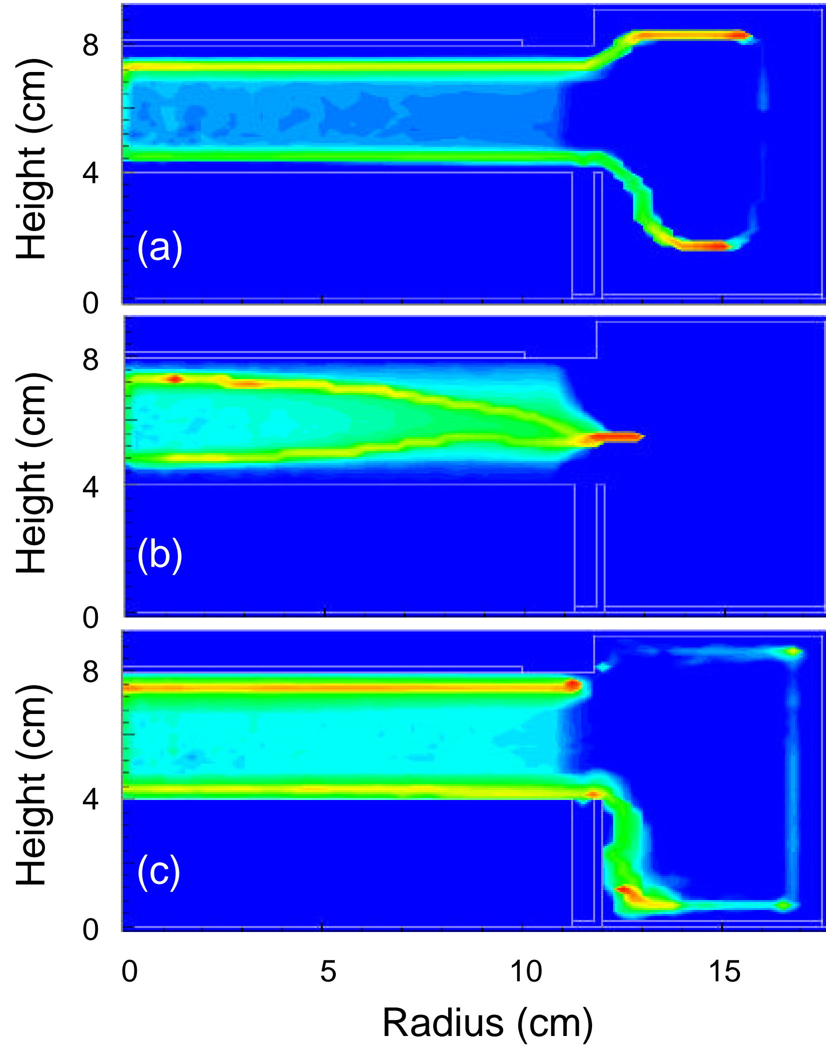

Figure 3.37. Time fluence contours for primary particles (a) 50 nm, (b) 200 nm, and (c) 500 nm in radius in a 21.17 W discharge having 250 sccm of gas flow. The smaller particles are light enough to be entrained by the gas flow, while the 500 nm particles are driven outwards by both ion-drag and gravitational forces. The 200 nm particles are not affected as much.

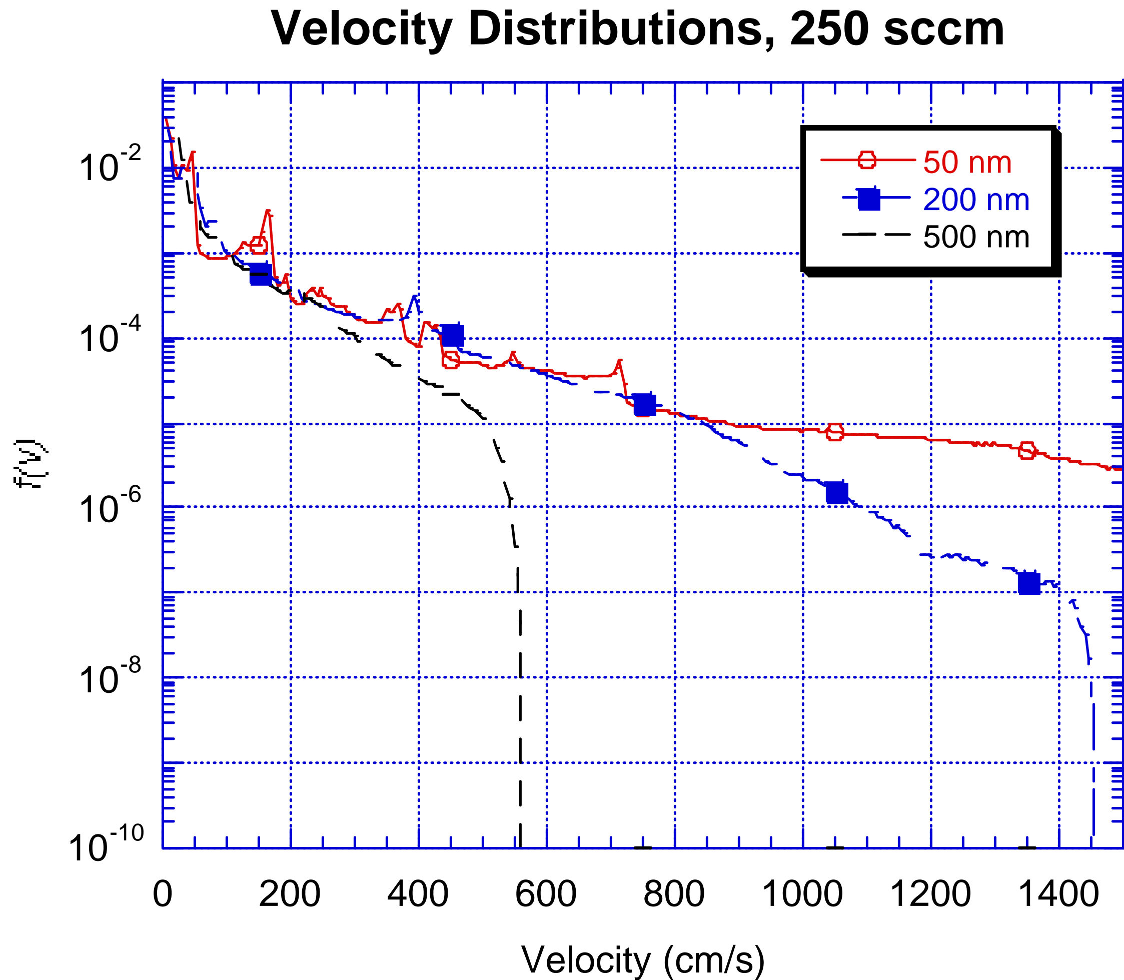

Figure 3.38. Total reactor velocity distributions for primary particles 50 nm to 500 nm in radius in a 21.17 W Ar discharge having 250 sccm of gas flow. The smaller, lighter particles accelerate to much higher average velocities, although the maximum velocities are relatively unchanged from their values without gas flow.

3.5 References

[1]A. Garscadden, B. N. Ganguly, P. D. Haaland, and J. Williams, Plasma Sources Sci. Technol. **3**, 239 (1994).

4. CONCLUSIONS

A series of numerical simulations has been developed to investigate the phenomenon of dust particle contamination in reactive ion etch reactors. Dust contamination is a vital concern to the microelectronics industry, and poses a growing problem as minimum feature sizes continue to decrease. A Dust Transport Simulation (DTS) has been devised to simulate the transport of these dust particulates in the reactor chamber. Forces in the reactor exerted upon contaminants, including electrostatic, ion-drag, neutral fluid drag, thermophoretic, and gravitational forces, determine the trajectories traversed by the dust particles. In addition, self-diffusion due to pressure gradients in the particle distribution are considered.

Using the DTS, dust transport was found to be a function of reactor geometry and operating conditions. The two dominant forces under typical RIE operating conditions are the electrostatic and ion-drag forces. Electrostatic forces push particles toward the center of the discharge, while ion-drag drives them to the surfaces. In general, higher operating powers and larger particle sizes result in higher amounts of surface contamination. This is the regime where ion-drag forces begin to dominate, overwhelming the electrostatic forces and forcing the particles to the electrodes and wafer. To minimize contamination, lower operating powers are preferable. In order to optimize a commercial etching process, manufacturers should operate at the lowest power possible while maintaining acceptable etch rates.

Neutral gas flow was also found to be a potentially useful means of controlling contamination in the reactor. At sufficiently high flow rates, particles can become entrained in the feedstock gas flow as it moves from the gas inlets to the exhaust port. By doing so, particles can be swept away from the wafer region, hopefully before they contaminate it, and moved to less sensitive areas of the reactor.

A second computational tool, the particle agglomeration model (PAM), has been developed to study the agglomeration phenomenon. The criteria that must be met by two particles in order for them to agglomerate is based on energy considerations; the kinetic energy of the agglomeration pair must exceed the potential energy barrier which exists between them due to

their repulsive electric charge. A particle's kinetic energy is classically dependent on its mass (and thus the cube of its radius for spherically shaped particles) and square of its velocity. The PAM model compares these two energies for approaching particulates using a particle charge calculated using plasma conditions and velocities attained by the particles. Once again, higher RF powers and larger particle sizes proved to be detrimental operating conditions. The combination of larger mass and higher particle speeds due to greater ion-drag forces resulted in a much higher level of particle agglomeration. Ultimately, these larger structures are more difficult to repel from the wafer because of their large size; ion-drag forces can more easily force these particles to the surfaces in the reactor. Not only did the number of agglomerates increase under these conditions, but a larger fraction of the total dust population increased as well.

The Particle Agglomeration model showed that higher gas flow rates were still able to push large agglomerates away from the critical regions of the reactor. Although fluid flow can actually contribute to the agglomeration phenomenon through higher particle velocities, this agglomeration occurs in "safer" areas in the chamber, further out near the pump port.

Finally, a third module, the Molecular Dynamics extension (MD-PAM), was developed to more closely study the morphology of agglomerate particles. Currently used as a standalone model, with inputs taken from the Hybrid Plasma Equipment Model and the DTS, the MD-PAM simulates the motion of primary particles as they approach each other in the discharge. This is currently a particle-particle simulation which approximates the charge-shielding effect on each particle for the given plasma conditions. Two types of agglomerate growth were discovered: diffusive growth, which produces filamentary particles with low fractal dimension and ballistic growth, which produces tightly compacted, high fractal dimension clusters. Diffusive growth is favored by smaller primary particle sizes and/or lower approach velocities. Higher velocities and larger primary particles typically lead to ballistically grown agglomerates. A parameter $\boldsymbol{b}$ has been defined, which is the ratio of kinetic energy to potential energy for an agglomeration pair. This parameter, which is proportional to the square product of the primary particle radius and velocity for a given discharge, determines what type of agglomerate will be formed. Relatively low values

of ***b*** result in filamentary shapes, while high values of ***b*** produce compactly packed structures. Because higher operating powers and larger sizes increase the value of ***b***, these conditions favor the ballistically grown agglomerates. Generally, this operating regime also results in larger (i.e., more primary particles per agglomerate) particulates being formed.

Controlling contamination defects in vacuum processing equipment while maintaining the quality and throughput of the process recipe is a difficult task for IC manufacturers. Understanding the phenomena surrounding generation and growth of dust particles is the first step toward eliminating them. As the semiconductor industry continues its progress to the 0.25-μm feature size and beyond, dust contamination will continue to be an ever-growing problem. The industry will have to find more effective means of either preventing dust growth or removing dust from the reactor entirely.

VITA

Fred Huang was born in New York City in 1970. He received his B.S. and M.S. degrees in Electrical and Computer Engineering from the University of Illinois at Urbana-Champaign in May 1991 and October 1994, respectively. Under the direction of Professor Mark J. Kushner, he has conducted research in dc and RF electrical discharges. His work on an equivalent species representation modelling technique of dc positive columns and dust contamination transport and agglomeration in plasma etching reactors has resulted in three reviewed papers and eleven conference presentations. He is a Semiconductor Research Corporation Graduate Fellow, and a member of the Tau Beta Pi Engineering Honor Society.